POLITECNICO DI TORINO
THE UNIVERSITY OF TOKYO

Department of Mechanical and Aerospace Engineering
Master of Science in Aerospace and Astronautical Engineering

Master's Degree Thesis

Thermo-elastic analysis on a macroscale model of a triangular sub-array with dielectric patches

Supervisors
Prof. Alfonso PAGANI
Prof. Ryo HIGUCHI
Prof. Erasmo CARRERA
Dr. Rebecca MASIA

Candidate
Irene IZZO

Academic Year 2025/2026

Alla mia fortuna più grande,
i miei genitori Annarita e Giuseppe.

Alle mie stelle splendenti,
Vanessa e Pelè.

Ai cuori impavidi e gentili.

Thermo-elastic analysis on a macroscale model of a triangular sub-array with dielectric patches

Irene Izzo

Abstract

The new frontiers of space research increasingly require the adoption of extremely lightweight and ultra-thin structures, often characterized by anisotropic materials and capable of operating efficiently in the harsh space environment. Among these, large deployable space structures represent a key technological solution for space observation and telecommunications, as they allow the realization of highly efficient and extended apertures while complying with strict mass and stowage constraints. Due to their slenderness and large dimensions, such structures are typically subjected to complex thermo-mechanical loading conditions, including severe thermal gradients, which may induce deformations and consequently affect their functional performance. In this context, the present study aims to provide an effective and reliable modeling strategy for the analysis of highly extended and structurally complex systems with particular emphasis on the macroscale structural response. The proposed approach is based on the use of high-order theories within the framework of the Carrera Unified Formulation (CUF), which enables accurate modeling of anisotropic and slender structures with enhanced computational efficiency. The methodology is assessed through the macroscale decoupled thermo-elastic analysis of a representative triangular sub-array with dielectric patches, considered as a benchmark problem. Numerical results are validated through comparison with simulations performed using the commercial finite element software ABAQUS/-CAE, confirming the reliability and suitability of the proposed macroscopic model for multiscale analysis and design of large deployable space structures.

Table of Contents

1 Introduction **1**

1.1 Scope and Objectives 1

1.2 GEO environment 2

1.3 Structural typologies in Large-Scale Space systems 4

  1.3.1 Plate structures 4

  1.3.2 Modular truss structure 5

  1.3.3 Tesion-Dominated cable network structures 6

  1.3.4 Pure membrane structures in tension 8

  1.3.5 Tether-based structural systems 9

  1.3.6 Shell and spherical membrane structures 10

  1.3.7 Actively Deformable Structures 11

  1.3.8 Multi-body flexible structures 11

2 Multiscale Analysis **12**

2.1 Multiscale analysis procedure with CUF 13

2.2 Introduction to micromechanics 14

  2.2.1 Variational asymptotic method for the thermo-elastic unit cell 16

  2.2.2 Refined beam models for thermo-elastic RUC problem . 18

  2.2.3 Unified high-order finite beam elements 20

3 Theoretical Framework for plate macroscale models **25**

3.1 3D elasticity problem 25

  3.1.1 Equilibrium equation 25

  3.1.2 Boundary conditions 26

  3.1.3 Geometrical relations 26

  3.1.4 Hooke's law 27

3.2 Classical Theories 29

  3.2.1 Kirchhoff-Love plate theory 31

  3.2.2 Reissner-Mindlin plate theory 33

3.3 High Order Theories (HOT) 35

4 Carrera Unified Formulation 36
4.1 Introduction to CUF for 2D models 36
4.2 Finite Element Formulation and Fundamental Nuclei 37
4.3 Layer Wise (LW) and Equivalent Single Layer (ESL) models . . 42
4.3.1 Taylor Expansion (TE) 42
4.3.2 Lagrange Expansion (LE) 42

5 Thermo-elastic problem 44
5.1 Fundamentals of thermoelasticity 44
5.1.1 Stress tensor, Displacement and Strain tensor 44
5.1.2 Conservative laws 45
5.1.3 Hamilton's principle and the Principle of Virtual Displacements 47
5.1.3.1 PVD-based formulation for partially coupled thermoelastic analysis 48
5.1.3.2 PVD-based formulation for coupled thermoelastic analysis 48
5.2 Thermoelastic analysis and Unified Formulation 49
5.2.1 Compact formulation of governing and constitutive equations 49
5.2.2 Decoupled approach 51
5.2.3 Coupled approach 52

6 Sub-array preliminary models and thermo-elastic analysis results 55
6.1 Triangular sub-array with four ultra-thin layers 56
6.1.1 Problem set-up and model description 56
6.1.2 Convergence Analysis results 58
6.1.3 Macroscopic thermo-elastic deformation 63
6.2 Triangular sub-array with two ultra-thin layers with two in-plane geometries 66
6.2.1 Problem set-up and model description 67
6.2.2 Convergence Analysis results 68
6.2.3 Macroscopic thermo-elastic deformation 69
6.3 Triangular sub-array with four ultra-thin layers with three in-plane geometries 73
6.3.1 Problem set-up and models description 73
6.3.2 Macroscopic thermo-elastic deformation 74
6.4 Development of the final model without microstrips lines 78
6.4.1 ABAQUS Shell Model 79
6.4.2 CUF model 80

6.4.3 Macroscopic thermo-elastic deformation 80
6.4.4 Through-the-thickness stress distributions 86

7 Macroscale sub-array model **100**
7.1 Development of the final model 101
7.1.1 Abaqus 3D shell model 101
7.1.2 CUF model 103
7.2 Thermo-elastic analysis results 103
7.2.1 Macroscopic thermo-elastic deformation 104
7.2.2 Through-the-thickness stress distributions 111

8 Conclusions **123**
8.1 Future works 124

A Through-the-thickness stress distributions for Patch 2 of the preliminary triangular sub-array model without microstrip lines **125**

B Through-the-thickness stress distributions for Patch 2 of final triangular sub-array model **131**

Bibliography **136**

List of Figures

1.1 Geosynchronous Earth Orbit and Geostationary Earth Orbit . 3
1.2 GPR stellite under investigation 4
1.3 MR-SSPS 5
1.4 Supporting Truss 5
1.5 Astro MEsh 7
1.6 Astro MEsh 8
1.7 IKAROS solar sail 9
1.8 Artist conception of theter-SPS 9
1.9 SSPS-OMEGA 10

2.1 Multiscale approach concept representation 12
2.2 Multiscale analysis procedure 13
2.3 RUC and RVE models for micromechanics analysis 15
2.4 Coordinate reference systems of a periodic heterogeneous material and its RUC 16
2.5 Linear to seventh-order, hierarchical Legendre-type F_τ expansion used for HLE models 19

3.1 Generic plate reference system 30
3.2 Kirchhoff-Love displacement distribution 31
3.3 Kirchhoff-Love displacement field 32
3.4 Reissner-Mindlin deformed plate 33
3.5 Reissner-Mindlin displacement field 34

4.1 QUAD element representation with element numeration. 38
4.2 Representation of the assembly procedure: the FN is the core, the loops on τ and s build the matrix for a given pair of i and j, the loops on i and j give the matrix of the elements, and the loop on the elements gives the global stiffness matrix 39
4.3 Plate model with TE and LE 42

6.1 Plate model illustrating the geometric dimensions and boundary conditions implemented in the finite element simulation. (ABAQUS image) 56
6.2 Layered configuration of the composite plate illustrating the arrangement of CFRP (blue), copper foil (orange), and RT/Duroid 5880 dielectric (green) layers 57
6.3 Initial Q9 in-plane meshes for the proposed LW and ESL CUF structural models. 58
6.4 Relative percentage difference [%] w.r.t. ABAQUS model versus TE expansion order and number of DOF 59
6.5 Relative percentage difference [%] w.r.t. ABAQUS model versus TE expansion order and number of elements 60
6.6 Relative percentage difference [%] w.r.t. ABAQUS model versus LE expansion order and number of DOF 61
6.7 Relative percentage difference [%] w.r.t. ABAQUS model versus LE expansion order and number of elements 61
6.8 (a) Comparison of out-of-plane displacement under a 100 K thermal load between the Abaqus model and the selected third-order TE expansion model yielding the best results; (b) Displacement detail at (100,-100) 64
6.9 (a) Comparison of out-of-plane displacement under a 100 K thermal load between the Abaqus model and the selected first-order LE expansion model yielding the best results; (b) Displacement detail at (100,-100) 65
6.10 Sub-array ABAQUS model illustrating the layered configuration of CFRP plate (blue) and RT/Duroid 5880 layer (green) 66
6.11 Relative percentage error [%] versus expansion order and number of DOF, showing faster convergence and higher accuracy with CUF high-order expansions. 68
6.12 Out-of-plane displacement under a thermal load of 100 K: comparison between TE expansions, LE expansions and ABAQUS model results with respective DOF 70
6.14 CUF out-of-plane displacement under a thermal load of 100 K using Lagrange Expansion of the second order 71
6.13 ABAQUS out-of-plane displacement under a thermal load of 100 K 71
6.15 (a) Out-of-plane displacement under a thermal load of 100 K: comparison between LE expansion models and ABAQUS model results with respective DOF. (b) Displacement detail at (100,-100) 72

6.16 Sub-array ABAQUS model illustrating the layered configuration of CFRP plate (blue), copper foil + RT/Duroid 5880 layer (purple) and copper patches (orange) 73
6.17 ABAQUS out-of-plane displacement under a thermal load of 100 K 75
6.18 CUF out-of-plane displacement under a thermal load of 100 K using Lagrange Expansion of the second order 76
6.19 Out-of-plane displacement under a thermal load of 100 K: comparison between TE expansions, LE expansions and ABAQUS model results with respective DOF 76
6.20 Out-of-plane displacement under a thermal load of 100 K: comparison between TE expansions and ABAQUS model results with respective DOF 77
6.21 Out-of-plane displacement under a thermal load of 100 K: comparison between TE expansions, LE expansions and ABAQUS model results with respective DOF 77
6.22 Out-of-plane displacement under a thermal load of 100 K: comparison between third order TE expansion and ABAQUS model results. 78
6.23 Out-of-plane displacement under a thermal load of 100 K: comparison between second order LE expansion and ABAQUS model results. 78
6.24 ABAQUS model 79
6.25 ABAQUS model results 81
6.26 Out-of-plane displacement: comparison between TE expansions, LE expansions and ABAQUS model results with respective DOF 82
6.27 CUF out-of-plane displacement under a thermal load of 100 K using Lagrange Expansion of the second order 83
6.28 Out-of-plane displacement: comparison between TE expansions, LE expansions and ABAQUS model results with respective DOF 83
6.29 (a) Displacement detail at (-100,-100), (b) Displacement detail at (100,-100) 84
6.30 Out-of-plane displacement: comparison between third-order TE expansion model and ABAQUS model results 85
6.31 Out-of-plane displacement detail for TE 3 model: (a) at (-100,-100); (b) at (100,-100) 86
6.32 CUF model showing the analysed patches: "Patch 1" is highlighted in red, "Patch 2" is highlighted in purple 87
6.33 (a) "Patch 1" and evaluated node (x,y)=(-73.95, -90.23) mm; (b) "Patch 2" and evaluated node (x,y)=(78.62, -91.67) mm 87

6.34 Effect of through-the-thickness mesh refinement on the σ_{zz} stress profile. The comparison between the baseline mesh ($LE1/LE1/LE1/LE1$) and the refined configurations (up to $3LE1/3LE1/18LE1/3LE1$) shows that the stress gradients are consistently captured, indicating a converged numerical solution 89
6.35 Effect of through-the-thickness mesh refinement on the σ_{xx} stress profile. 90
6.36 Effect of through-the-thickness mesh refinement on the σ_{yy} stress profile. 90
6.37 Effect of through-the-thickness mesh refinement on the σ_{xy} stress profile. 91
6.38 Effect of through-the-thickness mesh refinement on the σ_{zz} stress profile. It is shown the comparison between the solution obtained with baseline mesh ($LE2/LE2/LE2/LE2$) and the refined configurations (up to $3LE2/3LE2/18LE2/3LE2$) 92
6.39 Effect of through-the-thickness mesh refinement on the σ_{xx} stress profile. 93
6.40 Effect of through-the-thickness mesh refinement on the σ_{yy} stress profile. 93
6.41 Effect of through-the-thickness mesh refinement on the σ_{xy} stress profile. 94
6.42 Effect of through-the-thickness mesh refinement on the σ_{zz} stress profile. It is shown the comparison between the solution obtained with baseline mesh ($LE3/LE3/LE3/LE3$) and the refined configurations (up to $3LE3/3LE3/18LE3/3LE3$). 94
6.43 Effect of through-the-thickness mesh refinement on the σ_{xx} stress profile. 95
6.44 Effect of through-the-thickness mesh refinement on the σ_{yy} stress profile. 95
6.45 Effect of through-the-thickness mesh refinement on the σ_{xy} stress profile. 96
6.46 Effect of through-the-thickness mesh refinement on the σ_{zz} stress profile. It is shown the comparison between the solution obtained with baseline mesh ($LE1/LE1/LE1/LE1$) and the refined configurations (up to $3LE1/3LE1/18LE1/3LE1$) 97
6.47 Effect of through-the-thickness mesh refinement on the σ_{xx} stress profile. 97
6.48 Effect of through-the-thickness mesh refinement on the σ_{yy} stress profile. 98

6.49 Effect of through-the-thickness mesh refinement on the σ_{xy} stress profile. 99

7.1 Original sub-array ABAQUS model illustrating the layered configuration of CFRP (blue), copper foil layer (not visible in orange), RT/Duroid 5880 layer (green) and copper patches with microstrip lines (orange) 100
7.2 Final sub-array ABAQUS model illustrating the layered configuration of CFRP (blue), copper foil layer (not visible in orange), RT/Duroid 5880 layer (green) and copper patches with microstrip lines (orange) 101
7.3 Exploded view of the subarray assembly. The components include the CFRP plate (blue), the copper (Cu) foil (orange), and the RT/Duroid 5880 substrate (green) 102
7.4 Boundary conditions of CUF model 104
7.5 ABAQUS model results 105
7.6 Out-of-plane displacement: comparison between TE expansions, LE expansions and ABAQUS model results with respective DOF 106
7.7 Out-of-plane displacement: comparison between TE expansions models and ABAQUS model results with respective DOF 106
7.8 Out-of-plane displacement: comparison between Third-Order Taylor expansions model and ABAQUS model results 107
7.9 Displacement detail for the Third-Order Taylor expansions model: (a) at (-100,-100); (b) at (100,-100) 108
7.10 CUF out-of-plane displacement under thermal load of 100 K using Lagrange Expansions of the third order 109
7.11 Out-of-plane displacement: comparison between LE expansions models and ABAQUS model results with respective DOF 109
7.12 Out-of-plane displacement: comparison between Third-Order Lagrange expansions model and ABAQUS model results 110
7.13 Displacement detail for LE 3 model: (a) at (-100,-100); (b) at (100,-100) 111
7.14 CUF model showing the analysed patches: "Patch 1" is highlighted in red, "Patch 2" is highlighted in purple 112
7.15 (a) "Patch 1" and evaluated node (x,y)=(-73.71, -90.22) mm; (b) "Patch 2" and evaluated node (x,y)=(78.37, -91.36) mm 112

7.16 Effect of through-the-thickness mesh refinement on the σ_{zz} stress profile. The comparison between the baseline mesh ($LE1/LE1/LE1/LE1$) and the refined configurations (up to $3LE1/3LE1/18LE1/3LE1$) shows that the stress gradients are consistently captured, indicating a converged numerical solution 113
7.17 Effect of through-the-thickness mesh refinement on the σ_{xx} stress profile. 114
7.18 Effect of through-the-thickness mesh refinement on the σ_{yy} stress profile. 115
7.19 Effect of through-the-thickness mesh refinement on the σ_{xy} stress profile. 115
7.20 Effect of through-the-thickness mesh refinement on the σ_{zz} stress profile. The comparison between the baseline mesh ($LE2/LE2/LE2/LE2$) and the refined configurations (up to $3LE2/3LE2/12LE2/3LE2$) shows that the stress gradients are consistently captured, indicating a converged numerical solution 116
7.21 Effect of through-the-thickness mesh refinement on the σ_{xx} stress profile. 116
7.22 Effect of through-the-thickness mesh refinement on the σ_{yy} stress profile. 117
7.23 Effect of through-the-thickness mesh refinement on the σ_{xy} stress profile. 117
7.24 Effect of through-the-thickness mesh refinement on the σ_{zz} stress profile. The comparison between the baseline mesh ($LE3/LE3/LE3/LE3$) and the refined configurations (up to $3LE3/3LE3/6LE3/3LE3$) shows that the stress gradients are consistently captured, indicating a converged numerical solution 118
7.25 Effect of through-the-thickness mesh refinement on the σ_{xx} stress profile. 118
7.26 Effect of through-the-thickness mesh refinement on the σ_{yy} stress profile. 119
7.27 Effect of through-the-thickness mesh refinement on the σ_{xy} stress profile. 119
7.28 Effect of through-the-thickness mesh refinement on the σ_{zz} stress profile. The comparison between the baseline mesh ($LE1/LE1/LE1/LE1$) and the refined configurations (up to $3LE1/3LE1/18LE1/3LE1$) shows that the stress gradients are consistently captured, indicating a converged numerical solution 121
7.29 Effect of through-the-thickness mesh refinement on the σ_{xx} stress profile. 121

7.30 Effect of through-the-thickness mesh refinement on the σ_{yy} stress profile. 122
7.31 Effect of through-the-thickness mesh refinement on the σ_{xy} stress profile. 122

A.1 Effect of through-the-thickness mesh refinement on the σ_{zz} stress profile. It is shown the comparison between the solution obtained with baseline mesh ($LE2/LE2/LE2/LE2$) and the refined configurations (up to $3LE2/3LE2/18LE2/3LE2$). 126
A.2 Effect of through-the-thickness mesh refinement on the σ_{xx} stress profile. 126
A.3 Effect of through-the-thickness mesh refinement on the σ_{yy} stress profile. 127
A.4 Effect of through-the-thickness mesh refinement on the σ_{xy} stress profile. 127
A.5 Effect of through-the-thickness mesh refinement on the σ_{zz} stress profile.It is shown the comparison between the solution obtained with baseline mesh ($LE3/LE3/LE3/LE3$) and the refined configurations (up to $3LE3/3LE3/18LE3/3LE3$). 128
A.6 Effect of through-the-thickness mesh refinement on the σ_{xx} stress profile. 129
A.7 Effect of through-the-thickness mesh refinement on the σ_{yy} stress profile. 129
A.8 Effect of through-the-thickness mesh refinement on the σ_{xy} stress profile. 130

B.1 Effect of through-the-thickness mesh refinement on the σ_{zz} stress profile. The comparison between the baseline mesh ($LE2/LE2/LE2/LE2$) and the refined configurations (up to $3LE2/3LE2/12LE2/3LE2$) shows that the stress gradients are consistently captured, indicating a converged numerical solution 131
B.2 Effect of through-the-thickness mesh refinement on the σ_{xx} stress profile. 132
B.3 Effect of through-the-thickness mesh refinement on the σ_{yy} stress profile. 132
B.4 Effect of through-the-thickness mesh refinement on the σ_{xy} stress profile. 133

B.5 Effect of through-the-thickness mesh refinement on the σ_{zz} stress profile. the baseline mesh ($LE3/LE3/LE3/LE3$) and the refined configurations (up to $3LE3/3LE3/6LE3/3LE3$) shows that the stress gradients are consistently captured, indicating a converged numerical solution 133
B.6 Effect of through-the-thickness mesh refinement on the σ_{xx} stress profile. 134
B.7 Effect of through-the-thickness mesh refinement on the σ_{yy} stress profile. 134
B.8 Effect of through-the-thickness mesh refinement on the σ_{xy} stress profile. 135

List of Tables

1.1 Direct solar, reflected solar (albedo), and planetary infrared radiation at GEO. 3

6.1 Layer configuration and thicknesses. 56
6.2 Mechanical and thermal properties: CFRP fabric details. 57
6.3 Mechanical and thermal properties: Copper foil. 57
6.4 Mechanical and thermal properties: RT/Duroid 5880 details. . . 57
6.5 ABAQUS Model properties: Nodes, Elements, and Degrees of Freedom. 57
6.6 Finite Element Mesh details: Nodes and Q9 elements for the in-plane mesh per model. 59
6.7 Convergence analysis: TE 1 expansion. 60
6.8 Convergence analysis: TE 3 expansion. 60
6.9 Convergence analysis: TE 5 expansion. 62
6.10 Convergence analysis: LE 1 expansion. 62
6.11 Convergence analysis: LE 2 expansion. 62
6.12 Convergence analysis: LE 3 expansion. 63
6.13 Best ESL Model: TE 3 expansion with 260 Q9 elements. 63
6.14 Best LW Model: LE 1 expansion with 260 Q9 elements. 63
6.15 ABAQUS Model properties: Nodes, Elements, and Degrees of Freedom. 67
6.16 Mesh characteristics for CFRP fabric and RT/Duroid 5880 substrate 67
6.17 Materials mechanical and thermal properties 67
6.18 Finite Element Mesh details: Nodes and Q9 elements for the in-plane mesh per model. 68
6.19 Maximum displacement obtained through a TE 1 order expansion at the left vertex $(-100, -100)$ and the corresponding |% Difference| w.r.t. ABQ. 69
6.20 Maximum displacement obtained through a LE2 order expansion at the left vertex $(-100, -100)$ and the corresponding |% Difference| w.r.t. ABQ 69

6.21 CUF model characteristics and thermo-elastic analysis results with TE . . . 70
6.22 CUF model characteristics and thermo-elastic analysis results with LE . . . 70
6.23 ABAQUS displacement results at (x,y)=(-100,-100) and (x,y)=(100,-100) . . . 71
6.24 ABAQUS model mesh characteristics . . . 73
6.25 Abaqus model: nodal and elemental distribution per layer. . . . 74
6.26 CUF model mesh characteristics . . . 74
6.27 ABAQUS model characteristics and thermo-elastic analysis results 74
6.28 CUF model characteristics and thermo-elastic analysis results with TE . . . 75
6.29 CUF model characteristics and thermo-elastic analysis results with LE . . . 75
6.30 ABAQUS model mesh characteristics . . . 79
6.31 Abaqus model: nodal and elemental distribution per material. . 80
6.32 CUF model mesh characteristics . . . 80
6.33 ABAQUS model characteristics and thermo-elastic analysis results 81
6.34 CUF characteristics and thermo-elastic analysis results: TE models. . . . 81
6.35 CUF characteristics and thermo-elastic analysis results: LE models. 82
6.36 Selected best LE expansion model results. . . . 85
6.37 Selected best TE expansion model results. . . . 86
6.38 Interlayer stress convergence results along the plate thickness at $(x, y) = (-73.95, -90.23)$ mm: First-Order Lagrange expansion 89
6.39 Interlayer stress convergence results along the plate thickness at $(x, y) = (-73.95, -90.23)$ mm: Second-Order Lagrange expansion 91
6.40 Interlayer stress convergence results along the plate thickness at $(x, y) = (-73.95, -90.23)$ mm: Third-Order Lagrange expansion 92
6.41 Interlayer stress convergence results along the plate thickness at $(x, y) = (78.62, -91.67)$ mm: First-Order Lagrange expansion . 96

7.1 ABAQUS model mesh characteristics . . . 101
7.2 Detailed nodal and elemental distribution across different shell layers. . . . 102
7.3 CUF model in-plane mesh characteristics . . . 103
7.4 Comparison of Abaqus displacement results with and without lines. . . . 104
7.5 Abaqus reference values for out-of-plane displacement w at (x,y)=(-100,-100) and (x,y)=(100,-100). . . . 105

7.6 Convergence analysis of out-of-plane displacement w for Taylor Expansion (TE) models. 105
7.7 Convergence analysis of out-of-plane displacement w for Lagrange Expansion (LE) models. 108
7.8 Interlayer stress convergence results along the plate thickness at $(x, y) = (-73.71, 90.22)$ mm: First-Order Lagrange expansion . . 113
7.9 Interlayer stress convergence results along the plate thickness at (x, y) = (-73.71,90.22) mm: Second-Order Lagrange expansion. . 114
7.10 Interlayer stress convergence results along the plate thickness at (x, y) = (-73.71,90.22) mm: Third-Order Lagrange expansion . . 120
7.11 INterlayer stress convergence results along the plate thickness ate (x,y)=(78.37,-91.36) mm: First-Order Lagrange expansion . 120

A.1 Interlayer stress convergence results along the plate thickness at $(x, y) = (78.62, -91.67)$ mm: Second-Order Lagrange expansion 125
A.2 Interlayer stress convergence results along the plate thickness at $(x, y) = (78.62, -91.67)$ mm: Third-Order Lagrange expansion . 128

Chapter 1

Introduction

1.1 Scope and Objectives

The scope of this thesis is the investigation of the structural behaviour of large, ultra-light planar phased-array antennas operating in the geostationary space environment, with particular emphasis on the effect of the thermal loading and the resulting thermoelastic deformations. The study focuses on a 30 m class antenna, which is conceived both as a key enabling technology for geostationary precipitation radar missions and as an intermediate technological step toward the development of future Space Solar Power System (SSPS). This dual role places stringent requirements on structural accuracy, mass efficiency and long-term stability under harsh orbital conditions. Unlike spaceborne radar systems operating in Low Earth Orbit, which are characterized by limited revisit times and intermittent observation windows, geostationary radar platforms enable the continuous monitoring of fixed regions on Earth throughout the entire mission lifetime. This capability is particularly relevant for the observation of increasingly extreme and rapidly evolving climatological phenomena, for which real-time data acquisition and reduced reaction times are essential. In this context, maintaining the electromagnetic performance of the antenna, i.e. surface planarity and beam-pointing accuracy, is a critical design requirement. The antenna concept investigated in this work is based on an ultra-thin composite architecture, consisting in a carbon fiber reinforced polymer (CFRP) plate acting as the primary load-bearing substarte, onto which dielectric layers, copper patches and strip elements are integretated to form a radiating surface [1]. While this configuration offers significant advantages in terms of mass reduction and functional adaptability, it also results in a structure that is inherently sensitive to thermo-mechanical loading. In the geostationary orbital environment, prolonged solar exposure combined with periodic eclipse phases induces pronounced and non-uniform temperature gradients across the antenna surface. These thermal conditions generate thermo-elastic deformations driven by the anisotropic properties of the composite material and by mismatches in the coefficients of thermal expansion among the different constituents. The primary objective of this thesis is therefore to develop and apply an advanced macroscopic modeling framework capable of accurately predicting the structural response of large, ultra-thin anisotropic composite plates under decoupled thermal and mechanical loading conditions. Particular attention is devoted to the use of high-order structural theories, which are required to capture the complex deformation pattern arising in slender composite structures while maintaining computational efficiency for large-scale applications. The numerical framework adopted in this study is designed to represent material anisotropy and through-the-thickness effects with high fidelty. Finally, by characterizing the residual deofrmation patterns induced by the geostationary thermal environment, this thesis aims to provide a structural analysis basis that may support the future development of active mechanical mitigation strategies. Such strategies, including cable-based systems, are of particular interest for the realization of future large-scale space structures, such as space solar power systems, where passive structural solutions alone may be insufficient to guarantee the required geometric accuracy. Overall, this thesis seeks to contribute to the advancement of structural modeling techniques for ultra-light space structures and to provide design-oriented insights relevant to next-generation geostationary phased array antennas and future space solar power infrastructures.

1.2 GEO environment

A geosynchronous orbit lies at an altitude of about 35786 km above Earth's surface. At this distance, satellites complete one revolution in 23 hours, 56 minutes and 4 seconds, matching Earth's sidereal day. Maintaining this orbital period requires a velocity of approximately 3 km/s. When the orbit is positioned above the equator ad moves from west to east in the same direction as Earth's rotation, it is known as geostationary earth orbit (GEO). In this configuration, the satellite appears fixed above specific point on Earth because its orbital motion matches the planet's rotational speed [2].

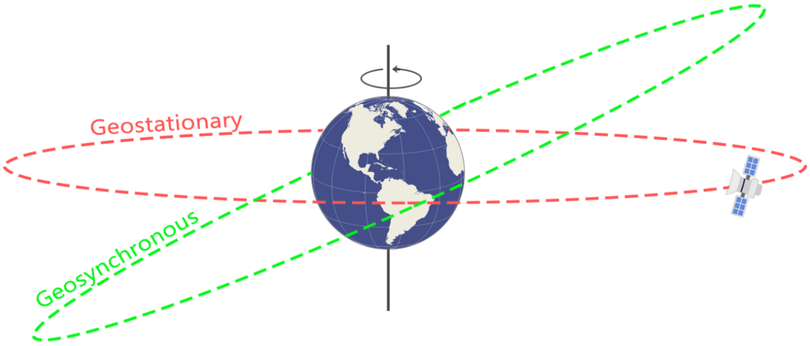

Figure 1.1: Geosynchronous Earth Orbit and Geostationary Earth Orbit

GEO is commonly used for satellites that must remain continuously above the same region, particularly telecommunication and broadcasting systems. The high altitude allows each satellite to observe a large portion of Earth's surface, so three equally spaced satellites can provide near-global coverage, as each one simultaneously monitors a wide area. Compared with Low Earth Orbit (LEO), GEO operates at a much greater distance from the planet. While LEO satellites orbit closer to Earth and require larger constellations to achieve global coverage, GEO satellites can observe broader regions due to their higher altitude. Satellites in GEO also experience eclipse periods when they enter Earth's shadow. These events occur twice a year and last for about $45 - 50$ days per season, with a maximum eclipse duration of approximately 71 minutes during each orbit. The thermal environment in GEO is characterized by a direct solar radiation that mainly varies with the time of year, except during eclipse seasons. The effects of reflected solar radiation (albedo) and planetary infrared radiation are minimal at this altitude. Since the orbital height remains constant, the view factor between the spacecraft and Earth does not change significantly, making these thermal contributions negligible compared with the direct solar input. [3]

Table 1.1: Direct solar, reflected solar (albedo), and planetary infrared radiation at GEO.

Radiation Source	**Perihelion**	**Aphelion**	**Mean**
Direct Solar $[W/m^2]$	1414	1323	1367.5
Reflected Solar - Subsolar Peak $[W/m^2]$	7.19	6.72	6.95
Reflected Solar - Orbit Average $[W/m^2]$	2.72	2.54	2.63
Planetary Infrared - Orbit Average $[W/m^2]$	5.52	5.52	5.52

1.3 Structural typologies in Large-Scale Space systems

Large-scale space systems such as ultralight phased array antennas, large deployable reflectors (LDRs) and Space Solar Power Systems (SSPS) pose structural challenges that differ fundamentally from those encountered in conventional spacecraft engineering. The characteristic dimensions of these structures ranges from tens of meters to several kilometers, subsequently, structural behavior is no longer governed primarily by material strength, but also by structural typology, geometric stability under thermal and orbital environments and trasmission mechanism. The choice of structural architecture determines not only mass efficiency and deployability, but also thermal stability, electromagnetic performance and scalability. The literature reveals a limited number of recurring structural typologies, each associated with a dominant mechanical regime and specific functional advanatges. This section reviews and classifies these typologies, emphasizing their structural principles and applicability to large space system.

1.3.1 Plate structures

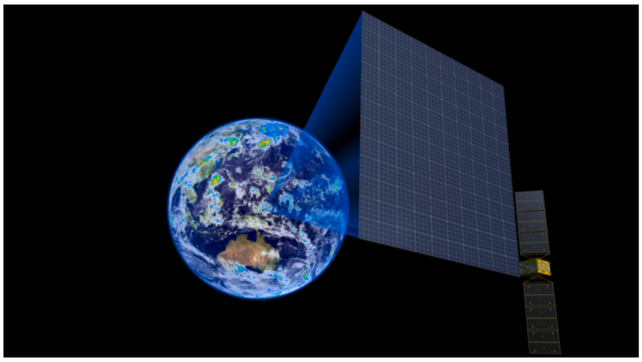

Figure 1.2: GPR stellite under investigation

Ultralight phased array antennas designed for SSPS and advanced communication missions frequently adopt a plate-like or membrane-based structural typology, typically realized through ultra-thin laminated composites such as carbon-fiber reinforced polymers (CFRP). IN this configuration, the antenna aperture itself acts as the primary load bearing element. Such antennas are not supported by discrete frames or trusses and they behave as 2-dimensional load-carrying continua. The structural role of the laminate is dual: it provides geometrical support while simultaneously serving as the substrate for radiating elements and embedded circuitry. As reported in the previous paragraph, in the work by Higuchi et al., a 30 m class phased array antenna is modeled as an anisotropic CFRP laminate populated by heterogeneous electronic inclusions. From a typological standpoint, the antenna is best described as an effective composite plate, rather than a homogeneous shell. Each radiating patch and condoctuive trace locally modifies the elastic and thermoelastic properties of the laminate, producing spatially varying stiffness and coefficients of thermal expansion. The dominant structural issue in this typology is thermally induced out-of-plane deformation. Extreme orbital temperature cycles generate intrinsic strain fields due to material mismatches, which induce bending and twisting moments. Geometric stability must be achieved through laminate tailoring and microstructural design rather than increased thickness or mass. This typology is particularly suited to large planar apertures requiring high functional integration and minimal mass, but it exhibits inherent sensitivity to thermal gradients and manufacturing imperfections.

1.3.2 Modular truss structure

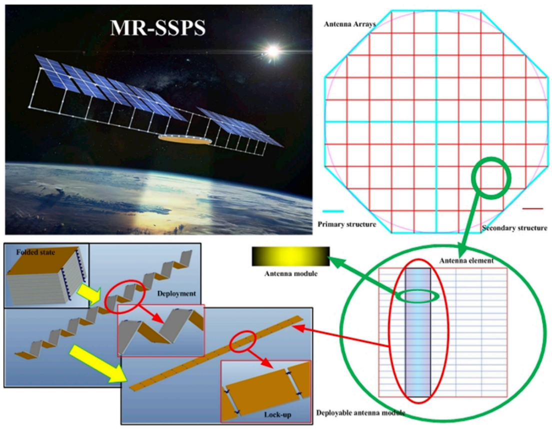

Figure 1.3: MR-SSPS

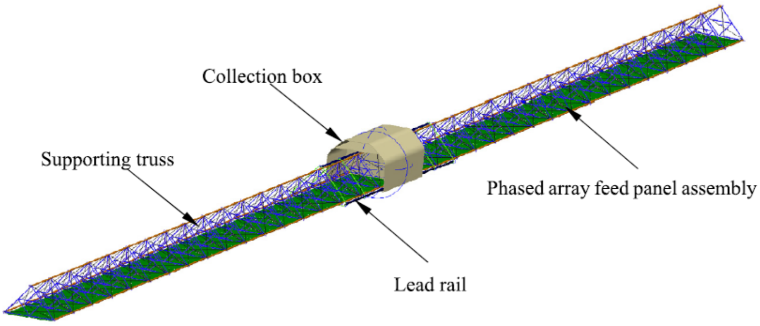

Figure 1.4: Supporting Truss

When continuous membranes become impractical due to size, handling and manufacturing constraints, large apertures are frequently realized through modular truss-based structures. This typology is characterized by assemblies of slender components by joints and forming spatial lattices with high stiffness-to-mass ratios. In phased array antennas and SSPS applications, the basic structural unit is typically a repeatable truss module, designed to be replicated and assembled into apertures extending over hundreds of meters or more [4]. Load transmission occurs primarily through axial forces in the members, while bending moments are minimized by geometry Structurally, modular truss systems exhibit:

- discrete load paths;
- localized compliance at joints;
- global stiffness emerging from aggregation rather than monolithic behavior.

However, as scale increases, these system develop extremely low natural frequencies and dense modal spectra. From a typological perspective, this is an unavoidable consequence of distributing mass and stiffness over large spatial extents. Small geometric deviations at the module level can propagate into significant global misalignments, directly affecting electromagnetic phase coherence.

The modular truss typology is therefore advantageous for scalability and assembly, but intrinsically sensitive to geometric tolerances and joint behavior. Its widespread adoption in SSPS concepts reflects the necessity of modular orbital assembly rather than structural optimality alone.

1.3.3 Tesion-Dominated cable network structures

Large deployable reflectors rely predominantly on tension-dominated structural typologies, in which geometric accuracy is achieved through pre-stress rather than bending stiffness. The most representative configuration is the peripheral ring cable-network reflector [5]

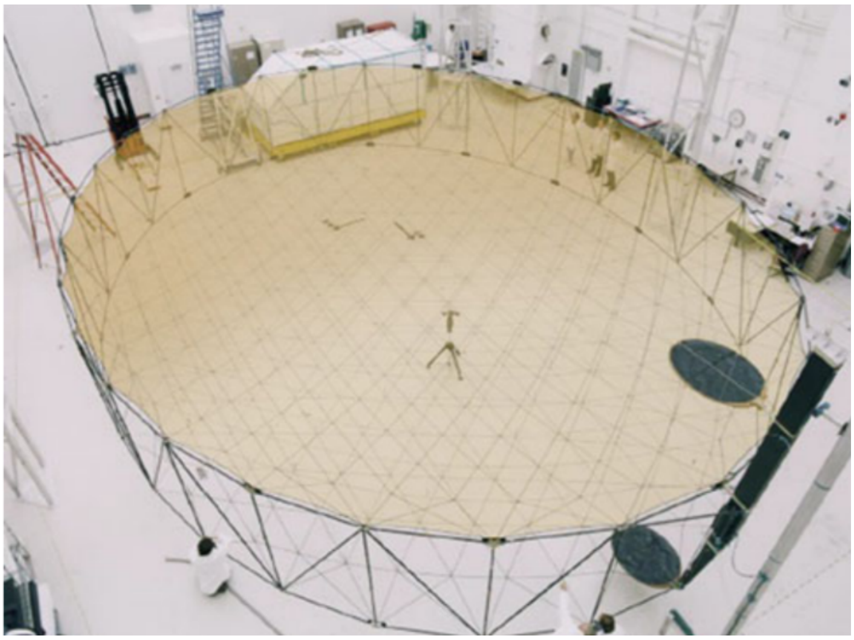

Figure 1.5: Astro MEsh

In this typology, a rigid or semi-rigid outer ring is placed in compression, while an interal cable net is pre-stressed in tension. The reflective mesh is supported by this cable network, which deifnes the desired parabolic surface through force equilibrium. From structural mechanics standpoint:

- the system is inherently nonlinear;
- stability depends on maintaining pre-stress;
- surface

The outer ring must resist compressive loads induced by the cabke net, making it susceptible to buckling. As aperture diameter increases beyond approximately 30-50 m, classical beam or plate-based approchase beocme mass-prohibitive, necessiting a shift toward pure tension systems. Simplified backbone concepts, such as radially supported mesh reflectors, reduce structural complexity by concentrating stiffness along primary load paths [6]

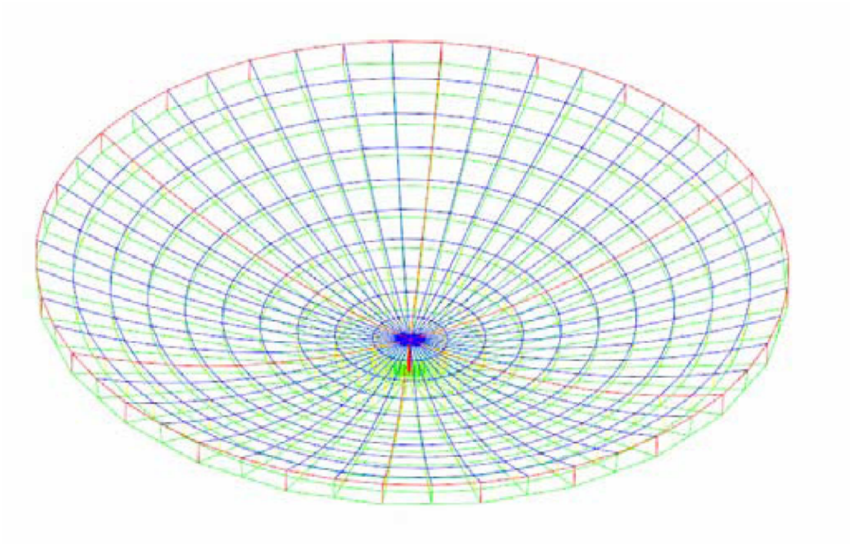

Figure 1.6: Astro MEsh

These designs demonstrate that surface precision can be preserved even with minimal rigid components, provided that cable geometry and tension are carefully optimized. This typology offers unmatched area-to-mass efficiency and excellent stowability, making it the dominant solution for very large reflector apertures.

1.3.4 Pure membrane structures in tension

An even more extreme tension-based typology is found in pure membrane structures, exemplified by sail-based SSPS concepts such as the European Sail Tower[7]. In these systems, ultra-thin membranes serve as both functional surfaces, e.g. photovoltaic arrays, and primarily structural elements. The membranes operate almost exclusively in tension, while compressive elements are minimized and relegated to deployment boom or a lightweight central mast. Structural stability is achieved not through rigidity, but through:

- membrame pre-stress;
- geometric configuration;
- coupling with orbital mechanics.

In the sail tower architecture, gravity-gradient forces are exploited as a passive stabilizing mechanism, effectively integrating celestial mechanics into structural concept. The resulting system represents a hybrid between a mechanical structure and an orbital dynamical configuration. This typology is attractive for kilometer-scale systems where any increase in bending stiffness would result in prohibitive mass penalties. However, it requires precise control of membrane tension and is highly sensitive to environmental perturbations.

1.3.5 Tether-based structural systems

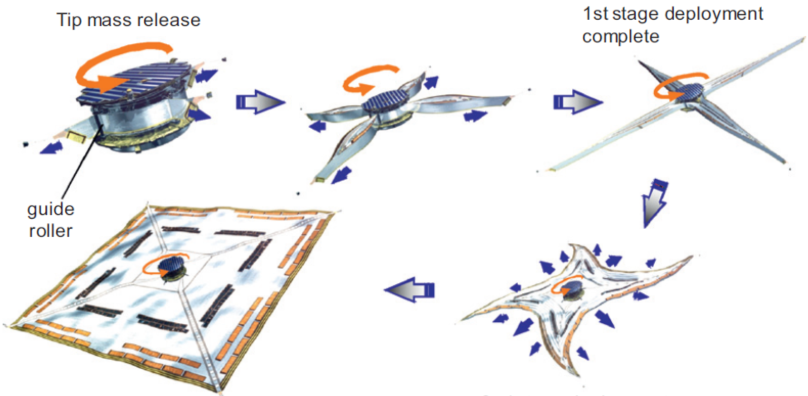

Figure 1.7: IKAROS solar sail

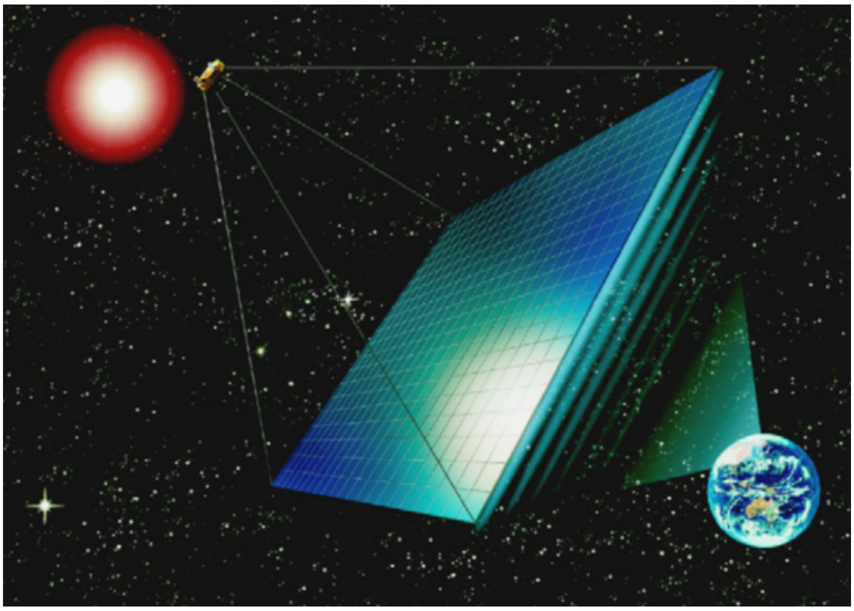

Figure 1.8: Artist conception of theter-SPS

Tethered SSPS concepts introduce a distinct structural typology in which long flexible cables replace rigid load-bearing members [8]. The system typically consists of two or more massive components connected by tethers that remain in tension due to gravity-gradient effects. From a structural perspective, the tether is the primary load-carrying element, while the connected bodies are not self-supporting in the traditional sense. The overall configuration behaves as a dynamically stabilized system rather than a statically determinate structure. Key characteristics of this typology include:

- structural stability derived from orbital mechanics;

- geometry dependent on mass distribution and tether length;
- strong coupling between structural deformation and attitude dynamics.

This approach eliminates the need for large rigid frameworks or rotary joints trading structural complexity for dynamical complexity. It represents a fundamental departure from classical spacecraft structural design.

1.3.6 Shell and spherical membrane structures

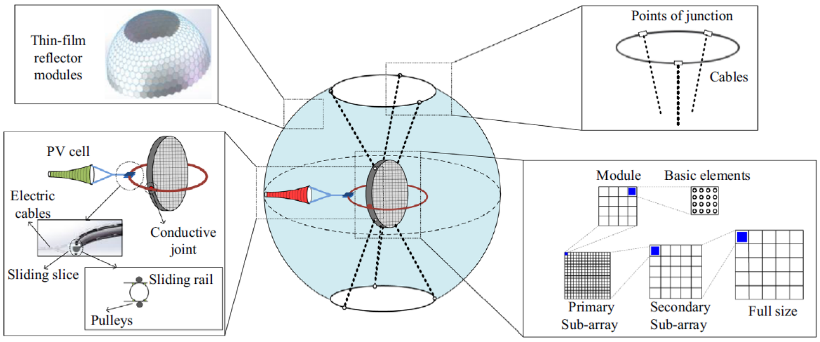

Figure 1.9: SSPS-OMEGA

The SSPS-OMEGA project introduces a spherical membrane-shell typology, in which structural efficiency is achieved through geometric symmetry [9]. The primary load-bearing element is a large, semi-transparent spherical membrane supported by a minimal internal frameworks. Structurally, spherical shells are inherently efficient, as membrane stresses are distributed isotropically. In an ideal configuration, bending moments are negligible and loads are carried almost entirely through uniform tension. This typology offers several structural advantages:

- minimized stress concentrations;
- reduced sensitivity to directional loading;
- favorable scaling behavior at very large sizes.

However, maintaining geometric precision in a membrane-based spherical structure presents significant challenges, particularly under thermal gradients and radiation pressure. In this case, structural simplicity shifts the engineering burden toward material stability and precision manufacturing.

1.3.7 Actively Deformable Structures

Actively controlled reflectors represent a hybrid typology in which structural flexibility is intentional [10]. Rather than maximizing passive stiffness, these systems are designed with reduced rigidity and equipped with actuators and sensors that impose the desired geometry. From a typological standpoint, such structures function as compliant substrates whose shape is actively maintained. Structural elements are dimensioned to remain within elastic limits while allowing controlled deformation.

This approach fundamentally alters the traditional trade-off between mass and stiffness, enabling lightweight structures to achieve high surface accuracy through active means. The structure itself becomes part of a closed-loop system, blurring the distinction between mechanical support and control infrastructures.

1.3.8 Multi-body flexible structures

The Itegrated Symmetrical Concentrator (ISC) exemplifies a multi-body flexible structural typology, consisting of large rigid subsystems connected by slender, flexible elements. The dominant structural challenge lies in the interaction between rigid-body motion and elastic deformation [11] Long booms connecting rotating concentrators introduce low-frequency flexible modes, making the structure highly sensitive to dynamic excitation. From a typological perspective, the ISC cannot be analyzed as a single structure, but rather as a coupled system of rigid and flexible bodies. This class of structures is particularly relevant for systems requiring large moving components, where traditional rigid architectures are infeasible.

Chapter 2

Multiscale Analysis

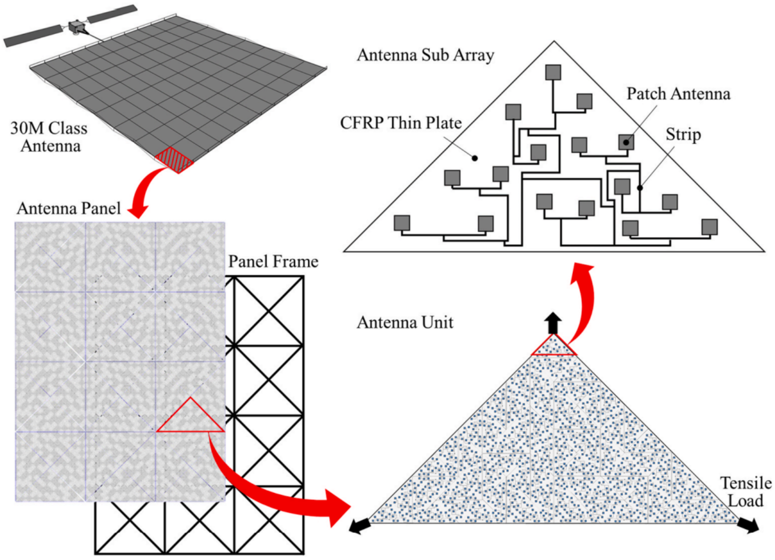

Figure 2.1: Multiscale approach concept representation

As anticipated in chapter 1, new space structures with ultra-thin thickness and materials characterized by anisotropic properties require structural analyses of various kinds to be addressed using new techniques, particularly multiscale models. In fact, for structures of such dimensions, it is no longer possible to neglect the micromechanical characteristics of the structure. Consequently, the analysis of the global structural response becomes computationally demanding. A multiscale analysis consists in establishing an interrelation between a micromechanical model and macroscale model. The flow of information between the micro- and macro- models is complex and currently several possible methods exist to accomplish this coupling.

2.1 Multiscale analysis procedure with CUF

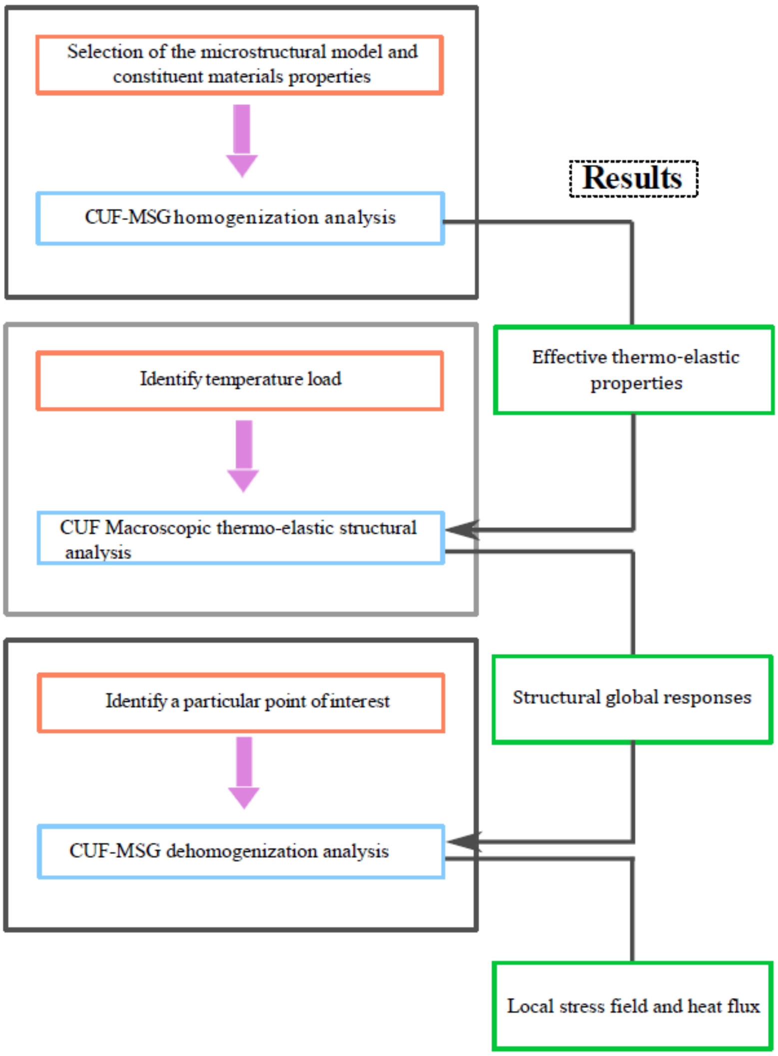

Figure 2.2: Multiscale analysis procedure

The procedure followed for multiscale analysis is commonly referred to as the "Up-Down" approach, which follows the logical workflow illustrated in the Figure 2.2. The first step consists of the homogenization phase, also known as the scale-up step, where the analysis starts from the microscale details. In this stage, the microstructural model is defined and, starting from the actual material properties, the corresponding homogenized properties are obtained. These homogenized properties represent the overall behaviour of the portion considered. This is achieved through the use of the Mechanics of Structure Genome (MSG) in combination with structural models, based on high-order Carrera Unified Formulation (CUF), allowing the microstructural behaviour of the structure to be analysed. As a result, a homogenized stiffness matrix is obtained, which accurately describes the global mechanical behaviour of the material. An introduction to micromechanics is provided in the following section. The second step, which is the stage discussed and analysed in terms of results in this work involves a preliminary macroscale model. At this level, external load and boundary conditions are applied. By employing CUF, the displacement and stress fields of the plate are obtained. Finally, the last step corresponds to dehomogenization phase, also referred to as the scale-down step. Using the CUF-MSG approach, the global results are then applied to the initial microscopic model. This procedure allows the actual stress distribution whithin the material to be reconstructed, for example the stresses at the fibre-matrix interface.

2.2 Introduction to micromechanics

A first challenge arises in developing an efficient and realistic model of the micromechanics of the structure. According to the current state of the art, micromechanical models aim to describe how microscal characteristics, such as the volume fraction and fibers' spatial distribution, influence the global structure behavior. Microstructural modeling is based on the definition of a representative unit, which can take different forms depending on the chosen approach:

- the Representative Volume Element (RVE) [12] [13], defined as the smallest structural volume composed of heterogeneous material that is still statistically representative of the entire composite composite. In this case, uniform displacement or uniform stress boundary conditions are typically applied;

- the Repeating Unit Cell (RUC), defined as the smallest geometric unit that can be periodically repeated in space to reconstruct the entire microstructure of the material and provide exact information about the local fields. In this case, fiber or inclusions are assumed to be arranged according a repetitive pattern and the applied boundary conditions must therefore be periodic or symmetric.

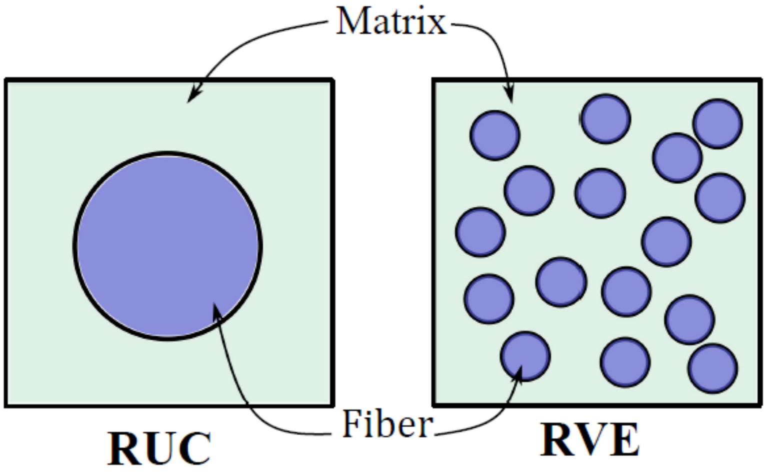

Figure 2.3: RUC and RVE models for micromechanics analysis

The extraction of information from RVE and RUC models can be performed using both analytical and numerical methods. Among the analytical methods, the following are commonly used:

- the Voigt [14] and Reuss [15] methods, which respectively assume that fiber and matrix experience the same strain (Voigt assumption) or the same stress (Reuss assumption). ;
- the Hashin-Shtrikman method [16], which provides a range of possible stiffness values for the material, independently of the shape of the fibers, starting from the elastic properties of the constituents and their volume fractions;
- the Mori-Tanaka method [17] considers an average field whitin which inclusions, i.e. the fibers, are embedded. It is commonly used to compute the global stiffness of composites reinforced with particles or short fibers. However, the contact between the fibers and the resulting stresses are neglected.

Among the classical numerical methods, it is possible to find:

- the Method of Cells (MOC) [18], in which the RUC is subdivided into a minimum of four building blocks. Within each of them, linear displacement variations are assumed;
- the Generalized Method of Cells (GMC) [19] represents an evolution of the previous model. In this case, the RUC is divided into a very fine grid of sub-cells. This method is particularly useful when the material is characterized by several different phases, such as fibers, coatings and matrix;

- the High-Fidelity Generalized Method of Cells (HFGMC) [20] uses more complex mathematical functions for each sub-cell in order to avoid approximation errors and it is used to predict material failure more accurately.

Lastly, advanced numerical approaches can be identified:

- the Mechanics of Structure Genome (MSG) [21], which employs the Variational Asymptotic Method (VAM) with the aim of minimizing the energy discrepancy between the microscopic and macroscopic models;
- he Carrera Unified Formulation (CUF), in which the fiber is modeled as a one-dimensional beam, while HLE functions are used to describe the information over the cross-section.

2.2.1 Variational asymptotic method for the thermo-elastic unit cell

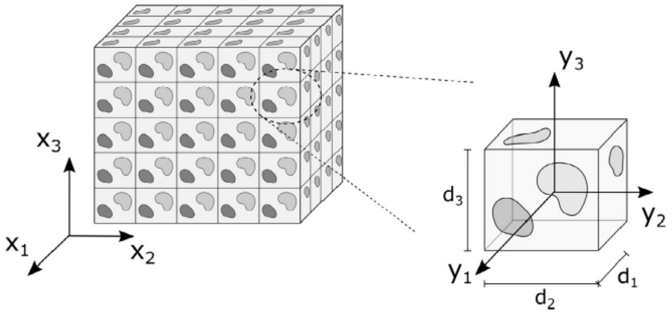

Figure 2.4: Coordinate reference systems of a periodic heterogeneous material and its RUC

The Representative Unit Cell (RUC) has dimensions that are significantly smaller than those of the global structure [22] . Two coordinate system are introduced: **x**, representing the global coordinate system and **y**, representing the local coordinate system of the RUC. These coordinates are related through the following expression:

$$\mathbf{y} = \frac{\mathbf{x}}{\delta} \tag{2.1}$$

where δ is a small scaling parameter describing the separation between the macro- and micro-scales. The local solutions are defined such that their volume average over the RUC corresponds to the global solution of the macroscopic problem .Considering the displacement field, these assumptions lead to a multiscale formulation in which the displacement field is decomposed in two contributions:

- a mean displacement field $\bar{u}(x)$, which depends only on the global coordinates;
- a local fluctuation field $u(x;y)$, which depends on both the global and local coordinates.

$$\bar{u}(x) = \frac{1}{V}\int_V u(x;y)dV \tag{2.2}$$

Boundary conditions may be periodic or symmetric. In the present work, periodic boundary conditions are adopted as an example. The MSG framework is based on minimizing the difference between the strain energy of the heterogeneous material and that of the homogenized equivalent material. This principle can be expressed through an appropriate energy functional:

$$\Pi = \frac{1}{2}\langle C_{ijkl}\varepsilon_{ij}\varepsilon_{kl} + 2\beta_{ij}\varepsilon_{ij}\theta + c_v\frac{\theta^2}{T_0}\rangle - \frac{1}{2}(C^*_{ijkl}\bar{\varepsilon}_{ij}\bar{\varepsilon}_{kl} + 2\beta^*_{ij}\bar{\varepsilon}_{ij}\theta + c^*_v\frac{\theta^2}{T_0}) \tag{2.3}$$

The terms appearing in the formulation include:

- the fourth-order elastic tensor C_{ijkl};
- the second-order strain tensor β_{ij};
- the thermal stress tensor β_{ij};
- the reference temperature T_0 corresponding to the stress-free condition;
- the specific heat per unit volume at constant volume c_v;
- θ, which represents the temperature difference with respect to the reference temperature.

The exact solution of the displacement field u can be expressed as the sum of the global displacement field and the fluctuations of the global displacements χ scaled by the parameter δ:

$$u(x;y) = \bar{u}(x) + \delta\chi(x;y) \tag{2.4}$$

The presence of two coordinate systems in the multiscale formulation requires that the derivatives of a field of the type u(x;y) be computed by considering both coordinate dependencies. The strain variables are therefore functions of both the global and locale coordinates:

$$\varepsilon_{ij}(x;y) = \bar{\varepsilon}(x) + \chi_{(ij)}(x;y) \tag{2.5}$$

in which

$$\bar{\varepsilon}(x) = \frac{1}{2}\Big(\frac{\partial \bar{u}_i(x)}{\partial x_j} + \frac{\partial \bar{u}_j(x)}{\partial x_i}\Big) \tag{2.6}$$

and

$$\chi_{(ij)}(x;y) = \frac{1}{2}\Big(\frac{\partial \bar{\chi}_i(x)}{\partial y_j} + \frac{\partial \bar{\chi}_j(x)}{\partial y_i}\Big) \tag{2.7}$$

If $\bar{u}_i = \langle u_i \rangle$ and $\bar{\varepsilon}_{ij} = \langle \varepsilon_{ij} \rangle$, which implies that the fluctuation are $\langle \chi_i \rangle = 0$ and $\langle \chi_{(ij)} \rangle = 0$- The unknown fluctuation terms can be solved by minimising the following functional:

$$\Pi^* = \frac{1}{2}\Big\langle C_{ijkl}[\bar{\varepsilon}_{ij} + \chi_{(i,j)}][\bar{\varepsilon}_{kl} + \chi_{(k,l)}] + 2\beta_{ij}[\bar{\varepsilon}_{ij} + \chi_{(i,j)}]\theta + c_v\frac{\theta^2}{T_0}\Big\rangle \tag{2.8}$$

The thermo-elastic problem can be solved by using refined and geometrically accurate beam models.

2.2.2 Refined beam models for thermo-elastic RUC problem

The MSG approach is not limited to a single type of material, but can be applied depending on the specific characteristics of the material under investigation; materials whose phases vary only within a single direction, i.e. unidirectional long-fiber reinforced composites, are treated as two-dimensional problems, where multi-phase materials, such as particulate composites or woven fiber composites, are treated as three-dimensional problems. The use of refined beam models for the RUC problem introduces an important innovation, particularly with the reference to three-dimensional cells obtained through the MSG approach. In this case, thanks to the Carrera Unified Formulation (CUF), it is possible to transform a complex cell into a refined one-dimensional model through higher-order expansion such as Hierarchical Legendre Expansions (HLE). This provides the opportunity to maintain accuracy in the description of local stress and strain fields, allowing the identification of critical points where material failure may occur. The beam axis, with length L, coincides with the fiber direction y_1, while the $y_2 - y_3$ plane defines the cross-section Ω of the beam model. Classical beam models are suitable only for cases characterized by high slenderness ratios, since they assume from a kinematic point of view that the cross-section remains plane and rigid. In contrast, CUF allows the definition and description of higher-order cross-sectional deformations, such as :

- warping, in which the RUC deforms out-of-plane;
- in-plane deformations, such as local contraction or expansion of the cross-section;

- component-wise solution fields, in which expansion of fibers and matrix are treated independently in order to account for their interactions at the interface.

The unknown fluctuations of the RUC are mathematically described as expansions over the cross-sections by means of arbitrary functions of the y_2 and y_3 coordinates [23]:

$$\chi(x; y_1, y_2, y_3) = F_\tau(y_2, y_3)\chi_\tau(x; y_1) \tag{2.9}$$

Here, χ denotes the vector of fluctuations, F_τ represents the expansion functions and χ_τ is the vector of generalized beam fluctuations along the fiber direction. The repeated index $\tau = 1, ..., M$ implies summation, while M indicates the total number of expansion terms assumed for the kinematic field. The specific choice of the functions F_s determines the beam theory adopted in the analysis.

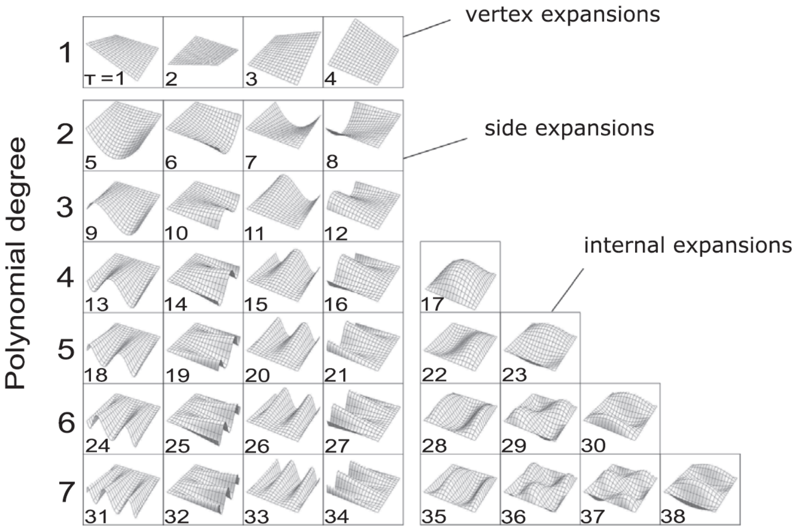

Figure 2.5: Linear to seventh-order, hierarchical Legendre-type F_τ expansion used for HLE models

Hierarchical Legendre expansions (HLE) beam models make use of the hierarchical nature of Legendre-based polynomials to generate sets of high-order polynomials employed as arbitrary expansion functions over the cross-section F_τ. The expansion functions are initially defined in a natural coordinate plane and subsequently mapped onto the beam cross-section, which allows for a straightforward formulation of Layer-Wise and Component-wise models. It can be observed that the displacement field and the solution accuracy improves with the inclusion of higher-order polynomials. Three categories of expansion functions are available: vertex, side and internal functions. The vertex functions corresponding to the first-order model are defined as:

$$F_\tau = \frac{1}{4}(1 - r_\tau r)(1 - s_\tau s) \qquad\qquad \tau = 1, 2, 3, 4 \tag{2.10}$$

The variables r and s span the domain form -1 and $+1$, while r_τ ands_τ are the coordinates of the vertices in the natural plane. Side expansions are defined for polynomial degree $p \geq 2$ in the natural plane as:

$$\begin{aligned} F_\tau(r,s) &= \frac{1}{2}(1-s)\phi_p(r) \quad p = 5, 9, 13, 18, \ldots \\ F_\tau(r,s) &= \frac{1}{2}(1+r)\phi_p(s) \quad p = 6, 10, 14, 19, \ldots \\ F_\tau(r,s) &= \frac{1}{2}(1+s)\phi_p(r) \quad p = 7, 11, 15, 20, \ldots \\ F_\tau(r,s) &= \frac{1}{2}(1-r)\phi_p(s) \quad p = 8, 14, 16, 21, \ldots \end{aligned} \tag{2.11}$$

Internal expansions F_τ are built by multiplying 1D internal modes. Consequently, they are expressed as:

$$\begin{aligned} F_{28}(r,s) &= \phi_4(r)\phi_2(s) \\ F_{29}(r,s) &= \phi_3(r)\phi_3(s) \\ F_{30}(r,s) &= \phi_2(r)\phi_4(s) \end{aligned} \tag{2.12}$$

A more detailed description of Legendre polynomials and Cross-section mapping are reported in [24],[25] and [26].

2.2.3 Unified high-order finite beam elements

The numerical problem along the y_1 beam axis can be solved with the finite element method (FEM). The $\chi_\tau(\boldsymbol{x}; y_1)$ in the Equation 2.9 are interpoled with Lagrange shape functions N_i on the y_1 direction as

$$\chi_\tau(\boldsymbol{x}; y_1) = N_i(y_1)\chi_{\tau i}(\boldsymbol{x}) \tag{2.13}$$

where $i = 1, ..., N$ and N i sthe numer of beam nodes. The global strain in the Voigt notation and the geometrical relation are:

$$\bar{\varepsilon}^T = \left\{ \bar{\varepsilon}_{11} \quad \bar{\varepsilon}_{22} \quad \bar{\varepsilon}_{33} \quad 2\bar{\varepsilon}_{13} \quad 2\bar{\varepsilon}_{23} \quad 2\bar{\varepsilon}_{12} \right\} \tag{2.14}$$

$$\varepsilon = \bar{\varepsilon} + B\chi \tag{2.15}$$

In the thermo-elastic problem [25], the Hooke's law can be written as

$$\sigma = C\varepsilon + \beta\theta \tag{2.16}$$

$$\Pi^* = \frac{1}{2}\int_V \left[(\bar{\varepsilon} + B\chi)^T C(\bar{\varepsilon} + B\chi) + 2\beta(\bar{\varepsilon} + B\chi)\theta + c_v\frac{\theta^2}{T_0}\right]dV \tag{2.17}$$

Where β is the 6 × 1 matrix

$$\Pi^* = \frac{1}{2}\Big(\chi_{sj}^T \boldsymbol{E}^{\tau sij}\chi_{\tau i} + 2\chi_{sj}^T \boldsymbol{D}_{h\varepsilon}^{sj}\bar{\boldsymbol{\varepsilon}} + \bar{\boldsymbol{\varepsilon}}^T D_{\varepsilon\varepsilon}\bar{\varepsilon} + 2\chi_{sj}^T D_{h\theta}^{sj}\theta + 2\bar{\varepsilon}^T D_{\varepsilon\theta}\theta + D_{\theta\theta}\frac{\theta^2}{T_0}\Big) \tag{2.18}$$

In the equation above there can be identified the following elements:

- $E^{\tau sij}$ and $D_{h\varepsilon}^{sj}$, the 3 × 3 and the 3 × 6 fundamental nuclei of the purely elastic RUC problem;
- $D_{\varepsilon\varepsilon}$, the averaged stiffness matrix;
- $D_{h\theta}^{sj}$ is the 3 × 1 FN as a result of thermal effects,
- $D_{\epsilon\theta}$ and $D_{\theta\theta}$ are respectively the average thermal stiffness matrix and averaged specific heat of the material.

For the RUC problem, the matrices E and $D_{h\varepsilon}$ are assembled throughout the τ, s, i and j indices, while $D_{h\theta}$ on the s and j indices. The integrals of the above components are the following:

$$\boldsymbol{E}^{\tau sij} = \int_\Omega\int_l (\boldsymbol{B}(F_s N_j \boldsymbol{I}))^T \boldsymbol{C}\boldsymbol{B}(F_\tau N_i \boldsymbol{I})d\Omega dy_1 C \tag{2.19}$$

$$\boldsymbol{D}_{h\varepsilon}^{sj} = \int_\Omega\int_l (\boldsymbol{B}(F_s N_j \boldsymbol{I}))^T \boldsymbol{C}d\Omega dy_1 \tag{2.20}$$

$$\boldsymbol{D}_{\varepsilon\varepsilon} = \int_V \boldsymbol{C}dV \tag{2.21}$$

and

$$\boldsymbol{D}_{h\theta}^{sj} = \int_\Omega\int_l (B(F_s N_j I))^T \beta d\Omega dy_1 \tag{2.22}$$

$$\boldsymbol{D}_{\varepsilon\theta} = \int_V \beta dV \tag{2.23}$$

$$\boldsymbol{D}_{\theta\theta} = \int_V c_V dV \tag{2.24}$$

The extended expression of $\boldsymbol{D}_{h\varepsilon}^{sj}$ are

$$\begin{aligned}
D_{h\varepsilon,11}^{sj} &= C_{11}\int_l N_j dy_1 \int_A F_{s,x} dA + C_{16}\int_l N_{j,y} dy_1 \int_A F_s dA \\
D_{h\varepsilon,12}^{sj} &= C_{12}\int_l N_j dy_1 \int_A F_{s,x} dA + C_{26}\int_l N_{j,y} dy_1 \int_A F_s dA \\
D_{h\varepsilon,13}^{sj} &= C_{13}\int_l N_j dy_1 \int_A F_{s,x} dA + C_{36}\int_l N_{j,y} dy_1 \int_A F_s dA \\
D_{h\varepsilon,14}^{sj} &= C_{44}\int_l N_j dy_1 \int_A F_{s,z} dA \\
D_{h\varepsilon,15}^{sj} &= C_{45}\int_l N_j dy_1 \int_A F_{s,z} dA \\
D_{h\varepsilon,16}^{sj} &= C_{16}\int_l N_j dy_1 \int_A F_{s,x} dA + C_{66}\int_l N_{j,y} dy_1 \int_A F_s dA \\
D_{h\varepsilon,21}^{sj} &= C_{12}\int_l N_{j,y} dy_1 \int_A F_s dA + C_{16}\int_l N_j dy_1 \int_A F_{s,x} dA \\
D_{h\varepsilon,22}^{sj} &= C_{22}\int_l N_{j,y} dy_1 \int_A F_s dA + C_{26}\int_l N_j dy_1 \int_A F_{s,x} dA \\
D_{h\varepsilon,23}^{sj} &= C_{23}\int_l N_{j,y} dy_1 \int_A F_s dA + C_{36}\int_l N_j dy_1 \int_A F_{s,x} dA \\
D_{h\varepsilon,24}^{sj} &= C_{45}\int_l N_j dy_1 \int_A F_{s,z} dA \\
D_{h\varepsilon,25}^{sj} &= C_{55}\int_l N_j dy_1 \int_A F_{s,z} dA \\
D_{h\varepsilon,26}^{sj} &= C_{26}\int_l N_{j,y} dy_1 \int_A F_s dA + C_{66}\int_l N_j dy_1 \int_A F_{s,x} dA \\
D_{h\varepsilon,31}^{sj} &= C_{13}\int_l N_j dy_1 \int_A F_{s,z} dA \\
D_{h\varepsilon,32}^{sj} &= C_{23}\int_l N_j dy_1 \int_A F_{s,z} dA \\
D_{h\varepsilon,33}^{sj} &= C_{33}\int_l N_j dy_1 \int_A F_{s,z} dA \\
D_{h\varepsilon,34}^{sj} &= C_{44}\int_l N_j dy_1 \int_A F_{s,x} dA + C_{45}\int_l N_{j,y} dy_1 \int_A F_s dA \\
D_{h\varepsilon,35}^{sj} &= C_{45}\int_l N_j dy_1 \int_A F_{s,x} dA + C_{55}\int_l N_{j,y} dy_1 \int_A F_s dA \\
D_{h\varepsilon,36}^{sj} &= C_{36}\int_l N_j dy_1 \int_A F_{s,z} dA
\end{aligned} \tag{2.25}$$

The extended expression of $\boldsymbol{D}^{sj}_{h\theta}$ is:

$$\begin{aligned}
D^{sj}_{h\theta,11} &= \beta_{11}\int_l N_{j,y_1} dy_1 \int_\Omega F_s d\Omega + \beta_{13}\int_l N_j dy_1 \int_\Omega F_{s,y_3} d\Omega + \\
&\qquad + \beta_{12}\int_l N_j d_{y_1} \int_\Omega F_{s,y_2} d\Omega \\
D^{sj}_{h\theta,21} &= \beta_{22}\int_l N_j dy_1 \int_\Omega F_{s,y_2} d\Omega + \beta_{23}\int_l N_j dy_1 \int_\Omega F_{s,y_3} d\Omega + \\
&\qquad + \beta_{12}\int_l N_{j,y_1} d_{y_1} \int_\Omega F_s d\Omega \\
D^{sj}_{h\theta,31} &= \beta_{33}\int_l N_j dy_1 \int_\Omega F_{s,y_3} d\Omega + \beta_{23}\int_l N_j dy_1 \int_\Omega F_{s,y_3} d\Omega + \\
&\qquad + \beta_{12}\int_l N_{j,y_1} d_{y_1} \int_\Omega F_s d\Omega
\end{aligned} \tag{2.26}$$

To minimize the functional reported in Equation 2.18, the following system of equations with unknown fluctuations needs to be solved

$$\boldsymbol{E}\chi = -\boldsymbol{D}_{h\varepsilon}\bar{\boldsymbol{\varepsilon}} - \boldsymbol{D}_{h\theta}\theta \tag{2.27}$$

Linear proportionality between χ and the terms $\bar{\boldsymbol{\varepsilon}}$ and θ is assumed:

$$\chi = \chi_0\bar{\boldsymbol{\varepsilon}} + \chi_\theta\theta \tag{2.28}$$

where χ_θ is a 3×1 matrix Consequently:

$$\begin{cases} \boldsymbol{E}\chi_0 = -\boldsymbol{D}_{h\varepsilon} \\ \boldsymbol{E}\chi_\theta = -\boldsymbol{D}_{h\theta} \end{cases} \tag{2.29}$$

Considering Equation 2.17 and Equation 2.28, the next expression is obtained

$$\Pi^* = \frac{1}{2}\bar{\boldsymbol{\varepsilon}}^T\boldsymbol{C}^*\bar{\boldsymbol{\varepsilon}} + \bar{\boldsymbol{\varepsilon}}^T\bar{\boldsymbol{\beta}}\theta + \frac{1}{2}\bar{c}_v\frac{\theta^2}{T_0} \tag{2.30}$$

The terms of the equation can be written explicitly:

$$\boldsymbol{C}^* = \frac{1}{\Omega}\Big[\chi_0^T\boldsymbol{D}_{h\varepsilon} + \boldsymbol{D}_{\varepsilon\varepsilon}\Big] \tag{2.31}$$

$$\bar{\boldsymbol{\beta}} = \frac{1}{\Omega}\Big[\frac{1}{2}(\boldsymbol{D}^T_{h\varepsilon}\chi_\theta + \chi_0^T\boldsymbol{D}_{h\theta}) + \boldsymbol{D}_{\varepsilon\theta}\Big] \tag{2.32}$$

$$\bar{c}_v = \frac{1}{\Omega}\Big[\chi_\theta^T\boldsymbol{D}_{h\theta}T_0 + \boldsymbol{D}_{\theta\theta}\Big] \tag{2.33}$$

The effective coefficient of thermal expansion are redefined as:

$$\bar{\boldsymbol{\alpha}} = -\boldsymbol{C}^{*-1}\bar{\boldsymbol{\beta}} \tag{2.34}$$

The fluctuation function as

$$\chi = \chi_0 \bar{\varepsilon} + \chi_\theta \theta \tag{2.35}$$

Subsequently, the local strain field becomes

$$\varepsilon = \bar{\varepsilon} + B(F_\theta N_i \chi) \tag{2.36}$$

The local stress field of the initial heterogeneous material, accordingly to the Hooke's law, is given by

$$\sigma = C\varepsilon + \beta\theta \tag{2.37}$$

Chapter 3

Theoretical Framework for plate macroscale models

This chapter provides the theoretical framework for the beam and plate models adopted in this study [27] [28] [26]. The first section is devoted to a review of classical advanced beam theories, including the Euler-Bernoulli and Timoshenko formulations, as well as classical and shear-deformable plate theories, . Kirchhoff-Love and Reissner-Mindlin. The second section introduces the high-order theory employed in the present research, which offers a unified and flexible approach for of beam- and plate-like structures.

3.1 3D elasticity problem

3.1.1 Equilibrium equation

Considering a continuous body of arbitrary shape, characterized by a volume **V** and a boundary surface **S** at any generic point **Q** within the volume, the differential form of the dynamic equilibrium equations must be satisfied along the three directions of the Cartesian reference system. A general case is considered in which volume **V** is subjected to body forces g_x, g_y g_z per unit volume.

$$\begin{aligned}
&\frac{\delta\sigma_{xx}}{\delta x}+\frac{\delta\tau_{yx}}{\delta y}+\frac{\delta\tau_{zx}}{\delta z}=g_x\\
&\frac{\delta\tau_{xy}}{\delta x}+\frac{\delta\sigma_{yy}}{\delta y}+\frac{\delta\tau_{zy}}{\delta z}=g_y\\
&\frac{\delta\tau_{xz}}{\delta x}+\frac{\delta\tau_{yz}}{\delta y}+\frac{\delta\sigma_{zz}}{\delta z}=g_z
\end{aligned}\tag{3.1}$$

The equations can also be written in vectorial form

$$\boldsymbol{b}^T\boldsymbol{\sigma}=\boldsymbol{g}\tag{3.2}$$

Where

$$\boldsymbol{\sigma} = \{\sigma_{xx}, \sigma_{yy}, \sigma_{zz}, \sigma_{xz}, \sigma_{yz}, \sigma_{xy}\} \tag{3.3}$$

$$\boldsymbol{b} = \begin{bmatrix} \frac{\delta}{\delta x} & 0 & 0 \\ 0 & \frac{\delta}{\delta y} & 0 \\ 0 & 0 & \frac{\delta}{\delta z} \\ \frac{\delta}{\delta z} & 0 & \frac{\delta}{\delta x} \\ 0 & \frac{\delta}{\delta z} & \frac{\delta}{\delta y} \\ \frac{\delta}{\delta y} & \frac{\delta}{\delta x} & 0 \end{bmatrix} \tag{3.4}$$

and

$$\boldsymbol{g}^T = \{g_x, g_y, g_z\} \tag{3.5}$$

3.1.2 Boundary conditions

The mechanical boundary conditions met on the surface S_m, where the loading vector is applied per unit of area, are

$$\begin{cases} \sigma_{xx} n_x + \tau_{xy} n_y + \tau_{xz} n_z = p_x \\ \tau_{xy} n_x + \sigma_{yy} n_y + \tau_{yz} n_z = p_y \\ \tau_{xz} n_x + \tau_{yz} n_y + \sigma_{zz} n_z = p_z \end{cases} \tag{3.6}$$

3.1.3 Geometrical relations

The relation between the engineering strain components and the displacement components is defined with the following differential equations.

$$\begin{cases} \varepsilon_{xx} = \frac{\delta u_x}{\delta x} = u_{x,x} \\ \varepsilon_{yy} = \frac{\delta u_y}{\delta y} = u_{y,y} \\ \varepsilon_{zz} = \frac{\delta u_z}{\delta z} = u_{z,z} \\ \gamma_{xy} = \frac{\delta u_x}{\delta y} + \frac{\delta u_y}{\delta x} = u_{x,y} + u_{y,x} \\ \gamma_{zx} = \frac{\delta u_x}{\delta z} + \frac{\delta u_z}{\delta x} = u_{x,z} + u_{z,y} \\ \gamma_{zy} = \frac{\delta u_y}{\delta z} + \frac{\delta u_z}{\delta y} = u_{y,z} + u_{z,y} \end{cases} \tag{3.7}$$

In this case as well, the relations may be expressed in a compact vectorial form:

$$\boldsymbol{\varepsilon} = \mathbf{bu} \tag{3.8}$$

Where

$$\mathbf{u}^T = \{u_x, u_y, u_z\} \tag{3.9}$$

$$\boldsymbol{\varepsilon}^T = \{\epsilon_{xx}, \epsilon_{yy}, \epsilon_{zz}, \epsilon_{xz}, \epsilon_{yz}, \epsilon_{xy}\} \tag{3.10}$$

3.1.4 Hooke's law

The Hooke's law represents the physical relation between stress and strain components:

$$\boldsymbol{\sigma} = \boldsymbol{C}\boldsymbol{\varepsilon} \tag{3.11}$$

where **C** is the stiffness matrix. Its form is determined by the constitutive properties of the material.

- The stiffness matrix for a generic isotropic material is

$$\boldsymbol{C} = \begin{bmatrix} C_{11} & C_{12} & C_{12} & 0 & 0 & 0 \\ C_{21} & C_{11} & C_{12} & 0 & 0 & 0 \\ C_{21} & C_{21} & C_{11} & 0 & 0 & 0 \\ 0 & 0 & 0 & C_{44} & 0 & 0 \\ 0 & 0 & 0 & 0 & C_{44} & 0 \\ 0 & 0 & 0 & 0 & 0 & C_{44} \end{bmatrix} \tag{3.12}$$

  The elastic response of an isotropic material is completely defined by two independent engineering constants: Young's modulus **E** and Poisson's ratio ν. All the components of the stiffness matrix can be expressed in terms of these two parameters. In particular, the relevant coefficients are given by:

$$C_{11} = \frac{(1-\nu)E}{(1+\nu)(1-2\nu)}$$

$$C_{12} = \frac{\nu(1-\nu)E}{(1+\nu)(1-2\nu)} \tag{3.13}$$

$$C_{44} = G = \frac{E}{2(1+\nu)}$$

  where G denotes the shear modulus. These relations highlight that only two independent constants are sufficient to characterize the mechanical behavior of isotropic materials.

- The symmetrical mechanical properties of an orthotropic material are defined with respect to three mutually orthogonal planes, typically identified as the (1,2), (2,3) and (3,1) planes. The principal material axes are referred to (1,2,3) directions. The stiffness matrix for a generic orthotropic material is

$$\boldsymbol{C} = \begin{bmatrix} C_{11} & C_{12} & C_{13} & 0 & 0 & 0 \\ C_{12} & C_{22} & C_{23} & 0 & 0 & 0 \\ C_{13} & C_{23} & C_{33} & 0 & 0 & 0 \\ 0 & 0 & 0 & C_{44} & 0 & 0 \\ 0 & 0 & 0 & 0 & C_{55} & 0 \\ 0 & 0 & 0 & 0 & 0 & C_{66} \end{bmatrix} \tag{3.14}$$

Unlike isotropic materials, orthotropic materials are characterized by nine independent elastic constants: the Young's moduli E_1, E_2, E_3, the shear moduli G_{12}, G_{13}, G_{23}, the Poisson's ratio ν_{12}, ν_{13} and ν_{23}. The engineering constants are defined as

$$E_i = \frac{\sigma_i}{\epsilon_i}$$

$$G_{ij} = \frac{\sigma_{ij}}{\epsilon_{ij}} \tag{3.15}$$

$$\nu_{ij} = -\frac{\epsilon_j}{\epsilon_i}$$

Due of the symmetry of the stiffness matrix, the reciprocal relation must be satisfied:

$$\frac{\nu_{ij}}{E_i} = \frac{\nu_{ji}}{E_j} \tag{3.16}$$

The stiffness coefficients can be expressed in terms of engineering constants through explicit relations involving the parameter

$$\Delta = 1 - \nu_{12}\nu_{21} - \nu_{23}\nu_{32} - \nu_{31}\nu_{13} - 2\nu_{12}\nu_{23}\nu_{31} \tag{3.17}$$

The shear components are directly related to shear moduli, namely:

$$C_{44} = G_{23}$$

$$C_{55} = G_{13} \tag{3.18}$$

$$C_{66} = G_{12}$$

- The stiffness components for a generic anisotropic material is

$$\boldsymbol{C} = \begin{bmatrix} C_{11} & C_{12} & C_{13} & C_{14} & C_{15} & C_{16} \\ C_{21} & C_{22} & C_{23} & C_{24} & C_{25} & C_{26} \\ C_{31} & C_{32} & C_{33} & C_{34} & C_{35} & C_{36} \\ C_{41} & C_{42} & C_{43} & C_{44} & C_{45} & C_{46} \\ C_{51} & C_{52} & C_{53} & C_{54} & C_{55} & C_{56} \\ C_{61} & C_{62} & C_{63} & C_{64} & C_{65} & C_{66} \end{bmatrix} \tag{3.19}$$

For the most general elastic material, there are 21 independent stiffness coefficients.

Hooke's law is expressed in the material coordinate system, aligned with the principal axes of orthotropy. Since structural analyses are generally performed in a global reference frame, it is necessary to establish transformation relations between stresses and strains defined in the material and global systems. These relations can be written as:

$$\boldsymbol{\sigma} = T\boldsymbol{\sigma}_m \tag{3.20}$$

$$\boldsymbol{\varepsilon}_m = \boldsymbol{T}^T\boldsymbol{\varepsilon} \tag{3.21}$$

where T is the transformation matrix. By substituting these relations into Hooke's law, it can be rewritten in the global reference system as:

$$\boldsymbol{\sigma} = \boldsymbol{TCT}^T\boldsymbol{\varepsilon} = \tilde{\boldsymbol{C}}\boldsymbol{\varepsilon} \tag{3.22}$$

The coefficients $\tilde{C}_{ij}$ represent the elastic constants of the orthotropic material expressed in the global coordinate system, and therefore incorporate the effect of the rotation between the material and structural reference frames. For brevity, the explicit form of these transformed coefficients is not reported here.

3.2 Classical Theories

Plate theories are reduced-order formulations developed to analyze structural elements whose thicknessis considerably smaller than their in-plane dimensions. When this geometric condition is satisfied, the full 3D elasticity problem can be efficiently reformulated as a 2D problem defined on a reference surface, typically the mid-surface of the plate.

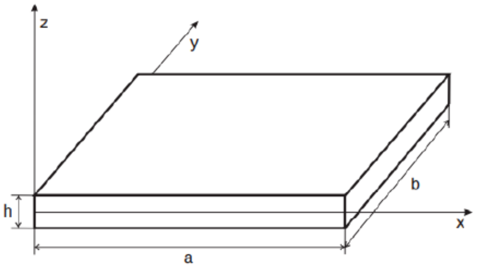

Figure 3.1: Generic plate reference system

This dimensional reduction significantly decreases computational cost while retaining the essential mechanical features of the structural response. The reduction is achieved by introducing an assumed distribution of the displacement field along the thickness coordinate z, which represents the directional normal to the the mid-surface. Instead of solving for the complete spatial dependence for the displacement components, their variation through the thickness is approximated analytically and the unknowns become functions of the in-plane coordinates only. Different methodologies can be adopted to define the through-the-thickness kinematics. Asymptotic approaches derive plate models directly from 3D elasticity through systematic expansion procedures, whereas axiomatic approaches assume a priori forms of the displacement field based on physically motivated hypotheses. IN axiomatic formulations, the displacement components are typically expressed as polynomial expansions in the thickness coordinate and its order determines the degree of the refinement of the theory. Classical models, such as the Classical Laminated Theory (CLT) and the First-Order Shear Deformation Theory (FSDT), are based on linear expansions in z. Although computationally efficient, these models may not accurately capture transverse shear effects in moderately thick or composite plates. High-Order Theories (HOTs) introduce polynomial expansions of greater degree improving the representation of transverse shear strains and stress distributions at the cost of additional computational effort. The Carrera Unified Formulation (CUF) provides a systematic and flexible framework capable of generating plate theories of arbitrary order whitin a unified athematical setting.

3.2.1 Kirchhoff-Love plate theory

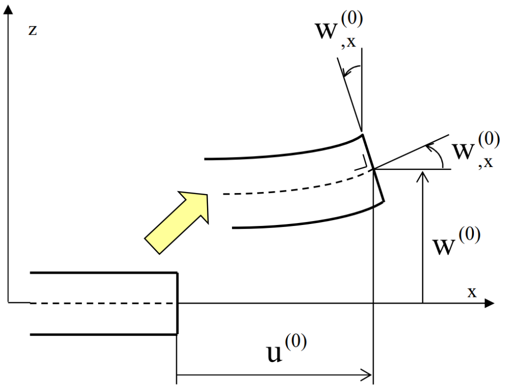

Figure 3.2: Kirchhoff-Love displacement distribution

In the framework of the Kirchhoff-Love theory, the kinematic assumptions are

- line segments normal to the mid-surface and initially straight remain straight after deformation;
- line segments normal to the mid-surface do not undergo extension, their length remains unchanged after deformation ($\epsilon_z z = 0$);
- line segments initially perpendicular to the mid-surface remain perpendicular to the deformed mid-surface, i.e. transverse shear strains are neglected ($\gamma_{xz} = \gamma_{yz} = 0$).
- the normal stress through the thickness are considered negligible ($\sigma_{zz} = 0$).

Considering the described hypothesis, the kinematic field is the following:

$$\begin{cases} u(x,y,z) = u^0(x,y) - zw^0_{,x}(x,y) \\ v(xy,z) = v^0(x,y) - zw^0_{,y}(x,y) \\ w(x,y,z) = w^0(x,y) \end{cases} \tag{3.23}$$

The terms u^0, v^0 and w^0 are the displacements on the plate reference surface, which is usually the mid surface.

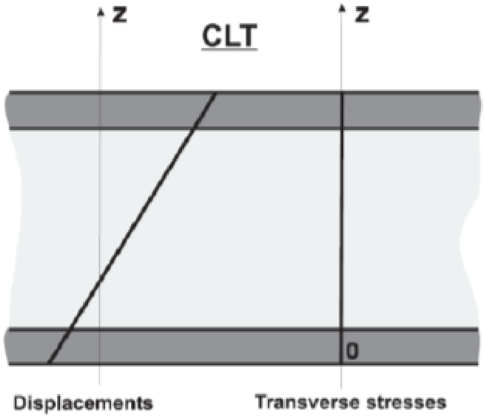

Figure 3.3: Kirchhoff-Love displacement field

The total deformations are written as

$$\{\epsilon_P\} = \{\epsilon_P^{(0)}\} + z\{\kappa_P\} \tag{3.24}$$

Where it is possible to differentiate between membrane deformation and bending deformation, respectively:

$$\{\epsilon_P^0\} = \begin{Bmatrix} \epsilon_{xx}^0 \\ \epsilon_{yy}^0 \\ \epsilon_{xy}^0 \end{Bmatrix} = \begin{Bmatrix} u_{,x}^0 \\ v_{,y}^0 \\ u_{,y}^0 + v_{,x}^0 \end{Bmatrix} \tag{3.25}$$

$$\{\kappa_P^0\} = \begin{Bmatrix} \kappa_{xx} \\ \kappa_{yy} \\ \kappa_{xy} \end{Bmatrix} = - \begin{Bmatrix} w_{,xx}^0 \\ w_{,yy}^0 \\ 2w_{,xy}^0 \end{Bmatrix} \tag{3.26}$$

The numerical code that corresponds to the present theory is the Classical Laminated Theory (CLT). In this case, rotations are directly related to the transverse displacement through spatial derivatives. This kinematic assumptions simplifies the formulation by reducing the number of independent degrees of freedom, since rotational variables are not introduces as additional primary unknowns. However, this semplification comes at the expense of an increased order of differentiation in the governing equations. Consequently, when the problem is discretized using the Finite Element Method (FEM), higher-continuity requirements arise and more complex shape functions are needed to ensure convergence and numerical stability.

3.2.2 Reissner-Mindlin plate theory

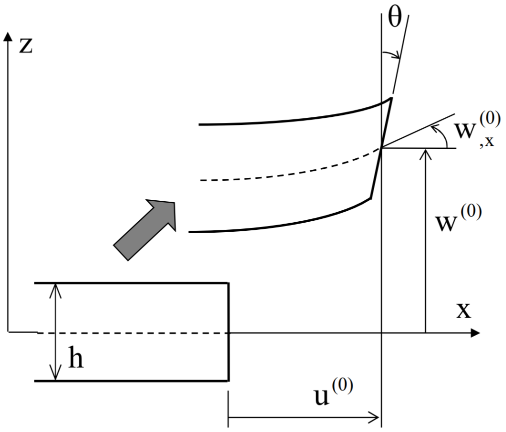

Figure 3.4: Reissner-Mindlin deformed plate

In Reissner-Mindlin theory, the kinematic assumptions are modified as follows:

- line segments initially straight and normal to the mid-surface remain straight after deformation;
- the length of these lie segments remains unchanged after deformation;
- line segments initially perpendicular to the mid-surface do not necessarily remain perpendicular to the deformed mid-surface, i.e. transverse shear deformation is accounted for

Considering the described hypothesis, the kinematic field is the following:

$$\begin{cases} u(x,y,z) = u^0(x,y) + z\theta(x,y) \\ v(x,y,z) = v^0(x,y) + z\varphi(x,y) \\ w(x,y,z) = w^0(x,y) \end{cases} \tag{3.27}$$

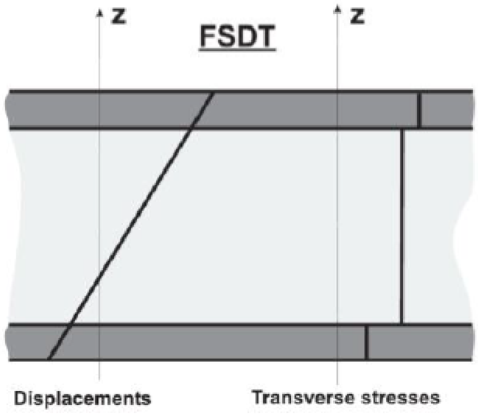

Figure 3.5: Reissner-Mindlin displacement field

The five independent variables are the displacements on the plate reference surface u^0, v^0 and w^0 and the rotations θ and φ. The total in-plane deformations are written as

$$\{\epsilon_P^0\} = \begin{Bmatrix} \epsilon_{xx}^0 \\ \epsilon_{yy}^0 \\ \epsilon_{xy}^0 \end{Bmatrix} = \begin{Bmatrix} u_{,x}^0 \\ v_{,y}^0 \\ u_{,y}^0 + v_{,x}^0 \end{Bmatrix} \tag{3.28}$$

Where it is possible to differentiate between membrane deformation and bending deformation, respectively:

$$\{\kappa_P^0\} = \begin{Bmatrix} \kappa_{xx} \\ \kappa_{yy} \\ \kappa_{xy} \end{Bmatrix} = \begin{Bmatrix} \theta_{,x} \\ \varphi_{,y} \\ \theta_{,y} + \varphi_{,x} \end{Bmatrix} \tag{3.29}$$

In addition, it is necessary to consider the transverse shear strain

$$\{\gamma_t\} = \begin{Bmatrix} \gamma_{xz} \\ \gamma_{yz} \end{Bmatrix} = \begin{Bmatrix} w_{,x}^0 + \theta \\ w_{,y}^0 + \varphi \end{Bmatrix} \tag{3.30}$$

This theory is implemented in the FSDT for all the commercial codes for the shell finite elements. In the First-Order Shear Deformation Theory, transverse shear deformation is explicitly accounted for, making the formulation more accurate than CLT when moderately thick plates are considered. Unlike CLT, rotations are treated as independent kinematic variables, allowing a more realistic representation of the displacement field through the thickness. Form a numerical standpoint, FSDT is often preferred over CLT in finite element implementations because the governing equations involve a lower order of spatial derivatives. As a result, a standard C^0- continuous shape functions can be employed, simplifying the formulation and implementation whitin the FEM framework.

3.3 High Order Theories (HOT)

High-Order Theories (HOT) describe the through-the thickness behavior by adopting polynomial expansions of increasing order in the z-direction. The complexity of the expansion directly influences both the accuracy of the kinematic representation and the associated computational cost. Classical models such as CLT and FSDT represent the simplest approximations for two-dimensional structural problems, as they rely on low-order expansions and simplified kinematic assumptions. Refined high-order theories provide a more accurate description of the displacement field and transverse shear effects, particularly in the analysis of thick plates and shells, where classical theories may exhibit limitations. An important advantage of these advanced formulations is their ability to represent the transverse shear strain distribution more realistically, often eliminating the need for shear correction factors required in the first-order models. The order of the through-the-thickness expansion can be tailored to the specific problem under consideration, including only the necessary terms to balance accuracy and computational efficiency. Different functional bases can be employed to approximate the displacement field. Among the most widely used are the Taylor Expansion (TE), based on polynomial terms of increasing degree in z, and the Lagrange Expansion (LE), which uses interpolation functions defined at selected points through the thickness.

Chapter 4

Carrera Unified Formulation

4.1 Introduction to CUF for 2D models

The Carrera Unified Formulation (CUF) generalizes classical structural models through an index notation that extends both the standard finite element indices $(i, j)$and the structural expansion indices (τ,s) [27]. As a result, the three-dimensional displacement field is described by four indices, enabling a compact and unified representation of a wide class of plate and shell theories. Plate models are characterized by an explicit assumption regarding the through-thickness kinematics. The thickness dependence may be approximated by linear or higher-order polynomials, or alternatively by Lagrange-type functions. In all cases, the displacement field is expressed as the product of:

- a known function of the thickness coordinate z;
- an unknown generalized displacement vector depending on the in-plane coordinates (x, y).

Using Einstein's summation convention for repeated indices, any two-dimensional structural theory can be expressed as:

$$\boldsymbol{U}(x, y, z) = F_\tau(z) U_\tau(x, y) \qquad \tau = 1, 2, ..., N \tag{4.1}$$

Where

- $F_\tau(z)$ are the thickness expansion functions;
- $u_\tau(x, y)$ are the generalized displacement vectors;
- N is the order of the expansion

The choice of the expansion functions determines the specific structural theory. Classical models such as the Classical Lamination Theory (CLT) and the First-Order Shear Deformation Theory (FSDT) can be obtained as special cases of a Taylor expansion by suitably reorganizing the stiffness matrix and enforcing appropriate constraints.

4.2 Finite Element Formulation and Fundamental Nuclei

In the finite element framework, the displacement field is approximated using nodal degrees of freedom and shape functions. For a displacement-based formulation, the internal virtual work considering linear kinematics is:

$$\delta L_{int} = \int_V \delta\varepsilon^T \boldsymbol{\sigma} dV = \int_V (\boldsymbol{B}_l \delta U)^T \boldsymbol{C} (\boldsymbol{B}_l U) dV \tag{4.2}$$

where B_l is the linear strain-displacement operator and C is the constitutive matrix. Using the finite element formulation, the dependence of the displacement field on the in-plane coordinates (x, y) is introduced through suitable shape functions. The interpolation of the displacement field is written as

$$u(x, y) = N_i(x, y) q_i \tag{4.3}$$

where

- q_i are nodal displacement vectors;
- N_i are the shape functions, whose analytical form is known and depends exclusively on the in-plane coordinates;
- i runs over the element nodes.

The finite element method provides a weak formulation of the structural problem by expressing the displacement at any point of the domain in terms of nodal values through the interpolation functions. Two-dimensional finite elements can be triangular (TRIA) or quadrilateral (QUAD), characterized by three or four sides, respectively. In the present work, quadrilateral elements are adopted to ensure improved convergence properties.

Different interpolation orders may be employed, leading to elements such as QUAD4 or QUAD9, the one used in the present work. Regardless of the number of nodes, Lagrange polynomials are used as shape functions, since they allow a straightforward and consistent interpolation of the displacement field.

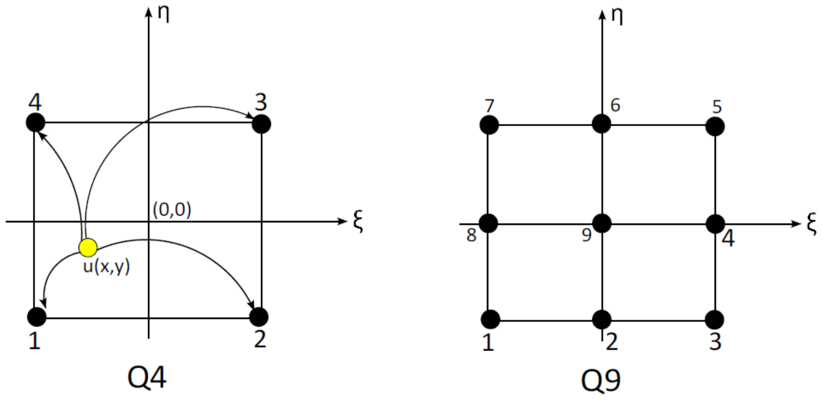

Figure 4.1: QUAD element representation with element numeration.

For a four-node quadrilateral element (QUAD4), the shape functions defined in the natural coordinate system (ξ, η) are given by:

$$N_1 = \frac{1}{4}(1-\xi)(1-\eta) \tag{4.4}$$

$$N_2 = \frac{1}{2}(1+\xi)(1-\eta) \tag{4.5}$$

$$N_3 = \frac{1}{4}(1+\xi)(1+\eta) \tag{4.6}$$

$$N_4 = \frac{1}{2}(1-\xi)(1+\eta) \tag{4.7}$$

For a nine-node quadrilateral element (QUAD9), the shape functions defined in the natural coordinate system (ξ, η) are given by:

$$N_1 = \frac{1}{4}(\xi^2-\xi)(\eta^2-\eta) \tag{4.8}$$

$$N_2 = \frac{1}{2}(1-\xi^2)(\eta^2-\eta) \tag{4.9}$$

$$N_3 = \frac{1}{4}(\xi^2+\xi)(\eta^2-\eta) \tag{4.10}$$

$$N_4 = \frac{1}{2}(\xi^2+\xi)(1-\eta^2) \tag{4.11}$$

$$N_5 = \frac{1}{4}(\xi^2+\xi)(\eta^2+\eta) \tag{4.12}$$

$$N_6 = \frac{1}{2}(1-\xi^2)(\eta^2+\eta) \tag{4.13}$$

$$N_7 = \frac{1}{4}(\xi^2-\xi)(\eta^2+\eta) \tag{4.14}$$

$$N_8 = \frac{1}{2}(\xi^2-\xi)(1-\eta^2) \tag{4.15}$$

$$N_9 = (1-\xi^2)(1-\eta^2) \tag{4.16}$$

The interpolation functions are formulated in the natural coordinate space.

For quadrilateral elements, the displacement at any generic point inside the element domain depends on the nodal values through the previously defined shape functions.

Substituting Equations (3.1) and (3.3) into the internal virtual work expression (3.2), the finite element discretization can be derived. The indices j and s are associated with the virtual variations and correspond to i and τ, respectively.

$$\begin{aligned}\int_V (\mathbf{B}_l\delta\mathbf{u})^T\mathbf{C}(\mathbf{B}_l\mathbf{u})\,dV &= \int_\Omega\int_h (\mathbf{B}_l F_s(z)\delta\mathbf{u}_s(x,y))^T\mathbf{C}\mathbf{B}_l F_\tau(z)\mathbf{u}_\tau(x,y)\,d\Omega\,dz\\ &= \int_\Omega\int_h (\mathbf{B}_l F_s(z)N_j(x,y)\delta\mathbf{q}_{sj})^T\mathbf{C}\mathbf{B}_l F_\tau(z)N_i(x,y)\mathbf{q}_{\tau i}\,d\Omega\,dz\\ &= \int_\Omega\int_h \delta\mathbf{q}_{sj}^T\mathbf{B}_{sj}^{lT}\mathbf{C}\mathbf{B}_{\tau i}^l\mathbf{q}_{\tau i}\,d\Omega\,dz\\ &= \delta\mathbf{q}_{sj}^T\left(\int_\Omega\int_h \mathbf{B}_{sj}^{lT}\mathbf{C}\mathbf{B}_{\tau i}^l\,d\Omega\,dz\right)\mathbf{q}_{\tau i} \qquad (3.4)\end{aligned}$$

The quantity

$$\mathbf{K}_{\tau sij} = \int_\Omega\int_h \mathbf{B}_{sj}^{lT}\mathbf{C}\mathbf{B}_{\tau i}^l\,d\Omega\,dz$$

defines the 3 × 3 stiffness Fundamental Nucleus (FN) for purely mechanical problems. The FN is independent of the specific plate theory adopted since only the thickness functions F_τ vary according to the selected kinematic model.

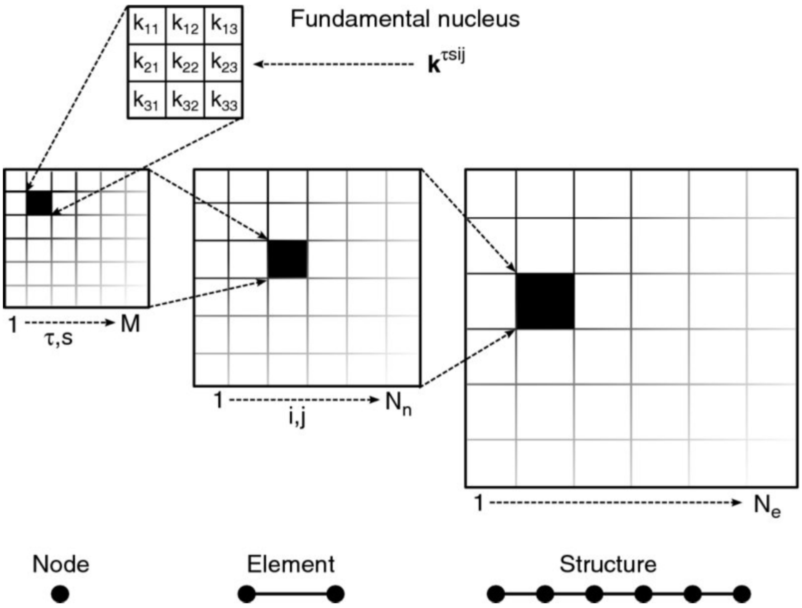

Figure 4.2: Representation of the assembly procedure: the FN is the core, the loops on τ and s build the matrix for a given pair of i and j, the loops on i and j give the matrix of the elements, and the loop on the elements gives the global stiffness matrix

The mehcanical Fundamental Nuclei can be explicitly written as:

$$\begin{aligned}K_{xx}^{\tau sij} = {} & C_{11}\int_{\Omega} N_{i,x}N_{j,x}d\Omega\int_{h} F_{\tau}F_{s}dz + C_{16}\int_{\Omega} N_{i,x}N_{j,y}d\Omega\int_{h} F_{\tau}F_{s}dz+\\ & +C_{16}\int_{\Omega} N_{i,y}N_{j,x}d\Omega\int_{h} F_{\tau}F_{s}dz + C_{44}\int_{\Omega} N_{i}N_{j}d\Omega\int_{h} F_{\tau,z}F_{s,z}dz+\\ & +C_{66}\int_{\Omega} N_{i,y}N_{j,y}d\Omega\int_{h} F_{\tau}F_{s}dz\end{aligned}\tag{4.17}$$

$$\begin{aligned}K_{xy}^{\tau sij} = {} & C_{12}\int_{\Omega} N_{i,y}N_{j,x}d\Omega\int_{h} F_{\tau}F_{s}dz + C_{62}\int_{\Omega} N_{i,y}N_{j,y}d\Omega\int_{h} F_{\tau}F_{s}dz+\\ & +C_{16}\int_{\Omega} N_{i,x}N_{j,x}d\Omega\int_{h} F_{\tau}F_{s}dz + C_{45}\int_{\Omega} N_{i}N_{j}d\Omega\int_{h} F_{\tau,z}F_{s,z}dz+\\ & +C_{66}\int_{\Omega} N_{i,x}N_{j,y}d\Omega\int_{h} F_{\tau}F_{s}dz\end{aligned}\tag{4.18}$$

$$\begin{aligned}K_{xz}^{\tau sij} = {} & C_{13}\int_{\Omega} N_{i}N_{j,x}d\Omega\int_{h} F_{\tau,z}F_{s}dz + C_{63}\int_{\Omega} N_{i}N_{j,y}d\Omega\int_{h} F_{\tau,z}F_{s}dz+\\ & +C_{44}\int_{\Omega} N_{i,x}N_{j}d\Omega\int_{h} F_{\tau}F_{s,z}dz + C_{45}\int_{\Omega} N_{i,y}N_{j}d\Omega\int_{h} F_{\tau}F_{s,z}dz\end{aligned}\tag{4.19}$$

$$\begin{aligned}K_{yx}^{\tau sij} = {} & C_{21}\int_{\Omega} N_{i,x}N_{j,y}d\Omega\int_{h} F_{\tau}F_{s}dz + C_{61}\int_{\Omega} N_{i,x}N_{j,x}d\Omega\int_{h} F_{\tau}F_{s}dz+\\ & +C_{26}\int_{\Omega} N_{i,y}N_{j,y}d\Omega\int_{h} F_{\tau}F_{s}dz + C_{45}\int_{\Omega} N_{i}N_{j}d\Omega\int_{h} F_{\tau,z}F_{s,z}dz+\\ & +C_{66}\int_{\Omega} N_{i,y}N_{j,x}d\Omega\int_{h} F_{\tau}F_{s}dz\end{aligned}\tag{4.20}$$

$$\begin{aligned}K_{yy}^{\tau sij} = {} & C_{22}\int_{\Omega} N_{i,y}N_{j,y}d\Omega\int_{h} F_{\tau}F_{s}dz + C_{62}\int_{\Omega} N_{i,y}N_{j,x}d\Omega\int_{h} F_{\tau}F_{s}dz+\\ & +C_{26}\int_{\Omega} N_{i,x}N_{j,y}d\Omega\int_{h} F_{\tau}F_{s}dz + C_{55}\int_{\Omega} N_{i}N_{j}d\Omega\int_{h} F_{\tau,z}F_{s,z}dz+\\ & +C_{66}\int_{\Omega} N_{i,x}N_{j,x}d\Omega\int_{h} F_{\tau}F_{s}dz\end{aligned}\tag{4.21}$$

$$\begin{aligned}K_{yz}^{\tau sij} = {} & C_{23}\int_{\Omega} N_{i}N_{j,y}d\Omega\int_{h} F_{\tau,z}F_{s}dz + C_{63}\int_{\Omega} N_{i}N_{j,x}d\Omega\int_{h} F_{\tau,z}F_{s}dz+\\ & +C_{55}\int_{\Omega} N_{i,y}N_{j}d\Omega\int_{h} F_{\tau}F_{s,z}dz + C_{45}\int_{\Omega} N_{i,x}N_{j}d\Omega\int_{h} F_{\tau}F_{s,z}dz\end{aligned}\tag{4.22}$$

$$\begin{aligned}K_{zx}^{\tau sij} = {} & C_{31}\int_{\Omega} N_{i,x}N_{j}d\Omega\int_{h} F_{\tau}F_{s,z}dz + C_{44}\int_{\Omega} N_{i}N_{j,x}d\Omega\int_{h} F_{\tau,z}F_{s}dz+\\ & +C_{45}\int_{\Omega} N_{i}N_{j,y}d\Omega\int_{h} F_{\tau,z}F_{s}dz + C_{36}\int_{\Omega} N_{i,y}N_{j}d\Omega\int_{h} F_{\tau}F_{s,z}dz\end{aligned}\tag{4.23}$$

$$\begin{aligned}K_{zy}^{\tau sij} = C_{32}\int_\Omega N_{i,y}N_j d\Omega \int_h F_\tau F_{s,z} dz + C_{55}\int_\Omega N_i N_{j,y} d\Omega \int_h F_{\tau,z} F_s dz + \\ + C_{45}\int_\Omega N_i N_{j,x} d\Omega \int_h F_{\tau,z} F_s dz + C_{36}\int_\Omega N_{i,x} N_j d\Omega \int_h F_\tau F_{s,z} dz\end{aligned} \tag{4.24}$$

$$\begin{aligned}K_{zz}^{\tau sij} = C_{33}\int_\Omega N_i N_j d\Omega \int_h F_{\tau,z} F_{s,z} dz + C_{44}\int_\Omega N_{i,x} N_{j,x} d\Omega \int_h F_\tau F_s dz + \\ + C_{45}\int_\Omega N_{i,x} N_{j,y} d\Omega \int_h F_\tau F_s dz + C_{45}\int_\Omega N_{i,y} N_{j,x} d\Omega \int_h F_\tau F_s dz + \\ + C_{55}\int_\Omega N_{i,y} N_{j,y} d\Omega \int_h F_\tau F_s dz\end{aligned} \tag{4.25}$$

The constitutive coefficients C_{ij} refer to the material stiffness matrix expressed in the global reference system.

For the external load contribution, the virtual work of applied forces is written as

$$\delta L_{\text{ext}} = \int_\Omega \delta \mathbf{u}^T \mathbf{p}(x,y)\, d\Omega = \int_\Omega \delta \mathbf{U}_{sj}^T F_s(z) N_j^T(x,y) \mathbf{p}(x,y)\, d\Omega = \delta \mathbf{U}_{js}^T \mathbf{P} \tag{3.6}$$

where $\mathbf{P}$ denotes the nodal load vector.

The static equilibrium condition is therefore expressed as

$$\delta L_{\text{int}} = \delta L_{\text{ext}} \tag{4.26}$$

which yields

$$\delta \mathbf{q}_{sj}^T \mathbf{K}_{\tau sij} \mathbf{q}_{\tau i} = \delta \mathbf{q}_{js}^T \mathbf{P} \tag{3.7}$$

and, consequently,

$$\mathbf{K}_{\tau sij} \mathbf{q}_{\tau i} = \mathbf{P} \tag{4.27}$$

where $\mathbf{U}_{\tau i}$ represents the nodal displacement vector of the finite element discretization.

4.3 Layer Wise (LW) and Equivalent Single Layer (ESL) models

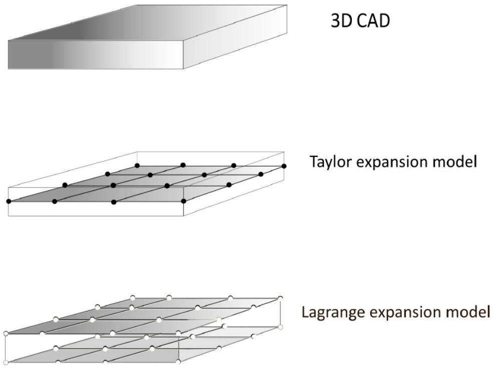

Figure 4.3: Plate model with TE and LE

4.3.1 Taylor Expansion (TE)

The Taylor Expansion (T) approach employs a complete polynomial expansion to describe the through-the-thickness displacement fiels. The order of the expansion is denoted by N, which determines the degree of the polynomial adopted in the thickness coordinate z. For example, a second-order expansion ($N = 2$) leads to a parabolic distribution of the displacement components along the thickness. In this case, the displacement field can be expressed as:

$$\begin{cases} u(x,y,z) = u_0(x,y) + zu_1(x,y) + z^2u_2(x,y) \\ v(x,y,z) = v_0(x,y) + zv_1(x,y) + z^2v_2(x,y) \\ w(x,y,z) = w_0(x,y) + zw_1(x,y) + z^2w_2(x,y) \end{cases} \tag{4.28}$$

With a second-order Taylor expansion, the three displacement components are described by a total of nine generalized two-dimensional variables, namely $u_i(x,y)$, $v_i(x,y)$ and $w_i(x,y)$, where $i = 0, 1, 2$. The same procedure can be systematically extended to higher-order models, for example generic $N - th$ order expansions, increasing the number of generalized variables and enhancing the capability of the model to capture complex through-the-thickness kinematic effects.

4.3.2 Lagrange Expansion (LE)

The second family of plate models is based on Lagrange polynomials and is generally referred to as the Lagrange Expansion (LE). This formulation exhibits two distinctive characteristics:

- the kinematic variables and boundary conditions can be directly assigned on the physical top and bottom surfaces of the structures;
- the fundamental unknowns consist solely of displacement components, without the introduction of independent rotational variables or additional higher-order generalized terms.

In traditional two-dimensional theories, the problem is typically formulated with respect to a single reference surface and all field variables are defined on that surface. Conversely, the LE describes the structural response interpolating the displacement field between the bottom and top surfaces of each layer. This feature enables boundary conditions to be imposed directly on the actual displacement components at the outer surfaces of the structure. In the case of multilayer structures, the Layer Wise (LW) approach employs LE, since each layer can be modeled independently while maintaining interlaminar displacement compatibility. According to the Lagrange kinematic assumption, the displacement field is expressed through interpolation functions defined along the thickness direction:

$$\begin{cases} u(x,y,z) = F_t(z)u_t(x,y) + F_b(z)u_b(x,y) \\ v(x,y,z) = F_t(z)v_t(x,y) + F_b(z)v_b(x,y) \\ w(x,y,z) = F_t(z)w_t(x,y) + F_b(z)w_b(x,y) \end{cases} \tag{4.29}$$

where $F_t(z)$ and $F_b(z)$ denote the Lagrange interpolation functions and subscripts t and b identify the displacement components evaluated respectively at the top and bottom surfaces of the layer. It is introduced a natural thickness coordinate $\zeta \in [-1, 1]$. Whitin this framework, the interpolation fuctions assume a simple and general expression:

$$F_t(\zeta) = \frac{1+\zeta}{2} \tag{4.30}$$

$$F_b(\zeta) = \frac{1+\zeta}{2} \tag{4.31}$$

This formulation ensures displacement compatibility across layers and allows direct enforcement of boundary conditions on the external surfaces.

Chapter 5

Thermo-elastic problem

5.1 Fundamentals of thermoelasticity

5.1.1 Stress tensor, Displacement and Strain tensor

In a deformable continuum initially at equilibrium, the resultant of external forces actig on any portion of tehe body is zero. When deformation occurs, internal forces arise to maintain equilibrium and are described by the stress tensor σ_{ij}. Owing to symmetry, it has six independent components: three normal stresses $\sigma_{xx}, \sigma_{yy}, \sigma_{zz}$ and three shear stresses $\sigma_{xy}, \sigma_{xz}, \sigma_{yz}$. [29] The traction vector on a plane with unit normal n_j is given by Cauchy's relation

$$t_i^{(n)} = \sigma_{ij} n_j \tag{5.1}$$

When the traction is parallel to the normal direction, shear components vanish and the normal stresses attain extreme values, called principal stresses. These are obtained form the characteristic equation

$$\sigma^3 - I_1 \sigma^2 - I_2 \sigma + I_3 = 0 \tag{5.2}$$

where the invariants $I_1 = \mathrm{tr}(\sigma), I_2$ and $I_3 = \det(\sigma)$ are independent of the reference frame. When subjected to mechanical or thermal loads, the body undergoes deformation described by the strain tensor ε_{ij}, which is symmetric and therefore has six independent components: three normal strains and three shear strains. Engineering shear strains are defined as $\gamma_{ij} = 2\varepsilon_{ij}$ for $i \neq j$. Strains are related to the displacement field u_i. In finite kinematics, the Green–Lagrange strain tensor is

$$\varepsilon_{ij} = \tfrac{1}{2}(\partial_j u_i + \partial_i u_j + \partial_i u_k \partial_j u_k) \tag{5.3}$$

$$\varepsilon_{ij} = \tfrac{1}{2}(\partial_j u_i + \partial_i u_j + \partial_i u_k \partial_j u_k) \tag{5.4}$$

For small displacement gradients, quadratic terms are neglected and the linear (Cauchy) strain tensor is obtained:

$$\varepsilon_{ij} = \tfrac{1}{2}(\partial_j u_i + \partial_i u_j) \tag{5.5}$$

$$\varepsilon_{ij} = \tfrac{1}{2}(\partial_j u_i + \partial_i u_j) \tag{5.6}$$

Like stresses, strains can be diagonalized, defining principal strains. Since six strain components depend on only three displacement components, geometric consistency requires the compatibility conditions

$$\varepsilon_{ij,kl} + \varepsilon_{kl,ij} - \varepsilon_{ik,jl} - \varepsilon_{jl,ik} = 0 \tag{5.7}$$

$$\varepsilon_{ij,kl} + \varepsilon_{kl,ij} - \varepsilon_{ik,jl} - \varepsilon_{jl,ik} = 0 \tag{5.8}$$

which ensure the existence of a continuous and single-valued displacement field.

5.1.2 Conservative laws

The governing equations of continuum mechanics are derived from the local forms of the conservation laws of linear momentum, angular momentum, and energy. Assuming constant density, mass conservation is automatically satisfied. The balance of linear momentum, obtained from Newton's second law and the divergence theorem, leads to the local equations of motion:

$$\sigma_{ij,j} + \rho b_i = \rho \ddot{u}_i \tag{5.9}$$

These equations describe dynamic equilibrium at each material point and require appropriate boundary conditions in terms of prescribed tractions or displacements. The conservation of angular momentum further implies that, in the absence of body couples, the Cauchy stress tensor is symmetric ($\sigma_{ij} = \sigma_{ji}$) The energy balance for an elastic continuum accounts for thermal and mechanical contributions. The rate of change of internal energy within a control volume equals the internally generated heat minus the heat flux leaving the domain. Assuming partial thermo-mechanical coupling, the internal energy depends only on temperature. Its rate form can be written as:

$$\dot{u} = \rho c(T)\dot{T} \tag{5.10}$$

where $c(T)$ is the specific heat capacity. Including volumetric heat sources and conductive heat flux, and applying the divergence theorem, the local energy equation becomes:

$$\rho c(T)\frac{\partial T}{\partial t} + \frac{\partial h_i}{\partial x_i} - Q = 0 \tag{5.11}$$

This expression represents the heat conduction equation in an elastic medium, linking temperature evolution to heat flux and internal heat generation.
In isotropic linear thermoelasticity, the total strain at a material point is composed of a mechanical contribution due to external forces and a thermal contribution proportional to the temperature change ΔT. The stress–strain–temperature relationship is expressed by the Duhamel–Neumann law:

$$\sigma_{ij} = 2\mu\epsilon_{ij} + [\lambda\epsilon_{kk} - \alpha(3\lambda + 2\mu)\Delta T]\delta_{ij} \tag{5.12}$$

where:

- δ_{ijis} the Kronecker delta, equal to 1 if i=jand 0 otherwise;
- α is the coefficient of linear thermal expansion, describing the material's tendency to expand or contract with temperature;
- $\lambda$and μ are the Lamé constants, which characterize the isotropic elastic response;
- K is the bulk modulus, measuring resistance to uniform volumetric compression

The elastic behavior of isotropic materials can be equivalently expressed using the standard engineering constants: Young's modulus E, shear modulus G, Poisson's ratio ν, bulk modulus K, and Lamé parameters $\lambda$and μ. These constants are mutually related through:

$$\mu = G = \frac{E}{2(1+\nu)} \tag{5.13}$$

$$\lambda = \frac{\nu E}{(1+\nu)(1-2\nu)} \tag{5.14}$$

$$K = \frac{E}{3(1-2\nu)} \tag{5.15}$$

Specifying any two independent elastic constants is sufficient to fully characterize the material's isotropic linear elastic response. This formulation allows the stress field to account for both mechanical deformation and thermal effects, providing a complete description of linear thermo-elastic behavior.

5.1.3 Hamilton's principle and the Principle of Virtual Displacements

The Principle of Virtual Displacements (PVD) is derived from Hamilton's principle. In the present formulation viscous effects are neglected; in more general cases they may be included through Rayleigh's dissipation function. Hamilton's principle states

$$\int_{t_1}^{t_2} \delta L^k dt = 0 \tag{5.16}$$

where L^k is the Lagrangian of the $k-th$ layer

$$L^k = T^k - \Pi^k \tag{5.17}$$

with T^k and Π^k denoting kinetic and total potential energy, respectively:

$$T^k = \frac{1}{2}\int_{V^k} \rho^k \dot{\boldsymbol{u}}\dot{\boldsymbol{u}} dV^k \tag{5.18}$$

$$\Pi^k = \Pi^k_{se} + \Pi^k_{ef} = \frac{1}{2}\int_{V^k} \left(\boldsymbol{\varepsilon}^{k^T}_{pG}\boldsymbol{\sigma}^k_{pC} + \boldsymbol{\varepsilon}^{k^T}_{nG}\boldsymbol{\sigma}^k_{nC}\right) dV^k + \frac{1}{2}\int_{V^k} \left(\boldsymbol{\varepsilon}^{k^T}_{pnl}\tilde{\boldsymbol{\sigma}}^k_{p0}\right) dV^k \tag{5.19}$$

Substituting Equation 5.17 into Equation 5.16 yields

$$\delta \int_{t_1}^{t_2} \Pi^k dt \delta \int_{t_1}^{t_2} T^k dt = 0 \tag{5.20}$$

The variation of the kinetic energy gives

$$\delta \int_{t_1}^{t_2} T^k dt = \int_{t_1}^{t_2} \int_{V^k} \rho^k \ddot{u} \delta u dV^k dt \tag{5.21}$$

since admissible variations satisfy $\delta u = 0$ at t_1 and t_2. This corresponds to the virtual work of inertial forces,

$$\delta \int_{t_1}^{t_2} T^k dt \text{Ĺ} \int_{t_1}^{t_2} \delta L^k_{in} dt \tag{5.22}$$

For conservative systems

$$\delta L^k_{int} = \delta \Pi^k_{se}, \qquad \delta L^k{}_{ext} = -\delta \Pi^k{}_{ef} \tag{5.23}$$

Which leads to

$$\int_{t_1}^{t_2} \delta L^k_{int} dt \int_{t_1}^{t_2} \delta L^k_{ext} dt \int_{t_1}^{t_2} \delta L^k_{in} dt \tag{5.24}$$

Removing the time integral provides the PVD at the layer level:

$$\delta L^k_{int} = \delta L^k_{ext} - \delta L^k_{in} \tag{5.25}$$

or equivalently

$$\int_{V^k} \left(\delta \boldsymbol{\varepsilon}^{k^T}_{pG} \boldsymbol{\sigma}^k_{pC} + \delta \boldsymbol{\varepsilon}^{k^T}_{nG} \boldsymbol{\sigma}^k_{nC} \right) dV^k \delta L^k_{ext} \delta L^k_{in} \tag{5.26}$$

This variational statement represents the weak form of equilibrium for the $k-th$ layer and constitutes the basis for finite element discretization.

5.1.3.1 PVD-based formulation for partially coupled thermoelastic analysis

In the context of thermal stress analysis, the Principle of Virtual Displacements (PVD) can be extended by treating temperature effects as an external load, assuming no direct coupling between mechanical and thermal fields. Under this assumption, the total stress in the $k-th$ layer is expressed as the algebraic combination of mechanical and thermal contributions:

$$\sigma^{pC}_k = \sigma^{pd}_k - \sigma^{pt}_k \tag{5.27}$$

$$\sigma^{nC}_k = \sigma^{nd}_k - \sigma^{nt}_k \tag{5.28}$$

where σ^{pd}_k and σ^{nd}_k represent the purely mechanical stress components in the layer, while σ^{pt}_k and σ^{nt}_k denote the thermal stress contributions. Based on this decomposition, the thermoelastic variational formulation of the PVD can be written as

$$\int_{\Omega_k} \int_{A_k} \delta \boldsymbol{\varepsilon}^{TpG}_k (\sigma^{pd}_k - \sigma^{pt}_k) + \delta \boldsymbol{\varepsilon}^{TnG}_k (\sigma^{nd}_k - \sigma^{nt}_k) d\Omega_k dz = \delta L^{F_{ext}}_k - \delta L^{F_{in}}_k \tag{5.29}$$

This statement provides the weak form of equilibrium for the k-th layer in the presence of thermal effects and forms the foundation for finite element implementation in thermoelastic problems.

5.1.3.2 PVD-based formulation for coupled thermoelastic analysis

A coupled thermoelastic variational principle based on the Principle of Virtual Displacements (PVD) can be formulated by incorporating the internal virtual work associated with thermal effects into the classical PVD framework. Accordingly, the general variational statement for the k-th layer can be expressed as

$$\int_{\Omega_k}\int_{A_k}(\delta\boldsymbol{\varepsilon}_{pG}^{k^T}\boldsymbol{\sigma}_{pC}^{k}+\delta\boldsymbol{\varepsilon}_{nG}^{k^T}\boldsymbol{\sigma}_{nC}^{k}-\delta\theta_k\eta_C^k-\delta\boldsymbol{\theta}_{pG}^{k^T}\boldsymbol{h}_{pC}^{k}-\delta\boldsymbol{\theta}_{nG}^{k^T}\boldsymbol{h}_{nC}^{k})d\Omega_k dz=\delta L_{F_{ext}}^k-\delta L_{F_{in}}^k \tag{5.30}$$

where θ_k denotes the temperature, η_k^C is the entropy per unit volume, θ_k^{pG} and θ_k^{nG} represent the spatial temperature gradients, and h_k^{pC} and h_k^{nC} correspond to the associated heat fluxes. In the particular case of free vibration analysis, variations in the temperature gradients are absent, so that the terms $\delta\theta_k^{T_{pG}}h_k^{pC}$ and $\theta_k^{T_{nG}}h_k^{nC}$ can be neglected. Under assumption, the coupled thermoelastic variational formulation simplifies to

$$\int_{\Omega_k}\int_{A_k}(\delta\boldsymbol{\varepsilon}_k^{T_{pG}}\boldsymbol{\sigma}_k^{pC}+\delta\boldsymbol{\varepsilon}_k^{T_{nG}}\boldsymbol{\sigma}_k^{nC}-\delta\theta_k\eta_k^C)d\Omega_k dz=\delta L_k^{F_{ext}}-\delta L_k^{F_{in}} \tag{5.31}$$

This simplified statement retains the essential coupling between mechanical strains, stresses, and thermal effects, while eliminating contributions due to temperature gradient variations, thereby providing a concise and rigorous basis for finite element modeling in thermoelastic free vibration problems.

5.2 Thermoelastic analysis and Unified Formulation

5.2.1 Compact formulation of governing and constitutive equations

Assuming small displacements/rotations and quasi-static temperature changes, total strain is the sum of mechanical and thermal contributions [30] [28] [31]:

$$\{\boldsymbol{\varepsilon}\}=\{\boldsymbol{\varepsilon}^M\}+\{\boldsymbol{\varepsilon}^T\} \tag{5.32}$$

Specifically

$$\{\varepsilon^M\}=\frac{1}{2G}\Big(\{\boldsymbol{\sigma}\}-\frac{\nu}{1+\nu}tr(\{\boldsymbol{\sigma}\})\{\boldsymbol{I}\}\Big) \tag{5.33}$$

$$\{\varepsilon^T\}=\alpha\theta\{\boldsymbol{I}\} \tag{5.34}$$

where $\theta=T-T_0$ consequently,the pure displacement formulation is

$$\{\boldsymbol{\sigma}\}=2G\Big[\{\varepsilon\}+\frac{\nu}{1-2\nu}(tr(\{\varepsilon\})-\frac{1+\nu}{\nu}\alpha\theta)\{I\}\Big] \tag{5.35}$$

$$\{\boldsymbol{\sigma}\}=2\mu\{\epsilon\}+\Big[\lambda tr(\{\epsilon\})-\alpha(3\lambda+2\mu)\theta\Big]\{\boldsymbol{I}\} \tag{5.36}$$

Considering the Cauchy's theorem for the elastic problem:

$$\nabla \cdot \{\boldsymbol{\sigma}\} + \{\boldsymbol{b}\} = \mu\Delta\{b\} + (\lambda+\mu)\nabla\cdot\{u\} - \alpha(3\lambda+2\mu)\nabla\theta + \{\boldsymbol{b}\} = 0 \tag{5.37}$$

The Fourier heat conduction equation introduces the temperature, the fourth variable:

$$\frac{\partial}{\partial x}\left(k_x\frac{\partial T}{\partial x}\right) + \frac{\partial}{\partial y}\left(k_y\frac{\partial T}{\partial y}\right) + \frac{\partial}{\partial z}\left(k_z\frac{\partial T}{\partial z}\right) = -\tau + \rho c\frac{\partial T}{\partial t} \tag{5.38}$$

Where ρ denotes the material density, T represents the temperature field, k_i are the thermal conductivity coefficients, τ is the rate of heat generation within the solid, and c is the specific heat of the material. Mechanical strains are represented in compact form based on linear geometric relations (small displacements and rotations):

$$\{\varepsilon_m\} = [\boldsymbol{b}]\{\boldsymbol{u}\} \tag{5.39}$$

Thermal strains are explicitly expressed via the vector of thermal expansion coefficients. Thermal expansion induced by a temperature field produces only normal strains, with no shear components

$$\{\varepsilon_t\} = \{\alpha\}\theta \tag{5.40}$$

where

$$\{\alpha\} = \{\alpha_1, \alpha_2, \alpha_3, 0, 0, 0\} \tag{5.41}$$

The constitutive law in vector form can then be written as:

$$\{\sigma\} = [C]\{\varepsilon_m\} - [C]\{\varepsilon_t\} = [C][\boldsymbol{b}]\{\boldsymbol{u}\} - \{\lambda\}\theta \tag{5.42}$$

The vector λ represents the thermoelastic coupling coefficients. For a general orthotropic material, the most general form of λ is:

$$\{\lambda\} = [C]\{\alpha\} = \begin{bmatrix} C_{11} & C_{12} & C_{12} & 0 & 0 & C_{16} \\ C_{12} & C_{11} & C_{12} & 0 & 0 & C_{26} \\ C_{12} & C_{12} & C_{11} & 0 & 0 & C_{36} \\ 0 & 0 & 0 & C_{44} & C_{45} & 0 \\ 0 & 0 & 0 & C_{45} & C_{55} & 0 \\ C_{16} & C_{26} & C_{36} & 0 & 0 & C_{66} \end{bmatrix} \begin{Bmatrix} \alpha_1 \\ \alpha_2 \\ \alpha_3 \\ 0 \\ 0 \\ 0 \end{Bmatrix} = \begin{Bmatrix} \lambda_1 \\ \lambda_2 \\ \lambda_3 \\ 0 \\ 0 \\ \lambda_6 \end{Bmatrix} \tag{5.43}$$

5.2.2 Decoupled approach

The mechanical and thermal components of stress and strain are independent. The mechanical part does not enter the heat conduction equation. As stated in subsubsection 5.1.3.1, the temperature field is assumed to be known and is not treated as an unknown variable: the heat conduction equation is not solved.

$$\int_v \{\delta\varepsilon\}^T\{\boldsymbol{\sigma}\}dV = \int_V \{\delta\boldsymbol{u}\}^T\{\boldsymbol{g}\}dV \tag{5.44}$$

Since mechanical and thermal contributions to strain are uncoupled constitutively, within the variational principle, stresses are explicitly included through the two separate contributions.

$$\begin{aligned}\delta L_{int} = \int_V \{\delta\varepsilon\}^T[\{\sigma_m\} + \{\sigma_t\}]dV = \\ = \int_V \{\delta\varepsilon\}^T[[C][\boldsymbol{b}]\{\boldsymbol{u}\} - [C]\{\alpha\}\theta]dV = \\ = \int_V \{\delta\boldsymbol{u}\}^T[\boldsymbol{b}]^T[C][\boldsymbol{b}]\{\boldsymbol{u}\}dV - \int_V \{\delta\boldsymbol{u}\}^T[\boldsymbol{b}]^T\{\lambda\}\theta dV\end{aligned} \tag{5.45}$$

The weak form of the decoupled thermo-elastic problem is

$$\int_V \{\delta\boldsymbol{u}\}^T[\boldsymbol{b}]^T[C][\boldsymbol{b}]\{\boldsymbol{u}\}dV = \int_V \{\delta\boldsymbol{u}\}^T[\boldsymbol{b}]^T\{\lambda\}\theta dV + \int_V \{\delta\boldsymbol{u}\}^T\{\boldsymbol{g}\}dV \tag{5.46}$$

Assuming a known and constant temperature field during system evolution allows the effects of temperature gradients on the structure to be reformulated simply, defining a physical quantity analogous to a purely mechanical load.

After establishing the variational principle, the problem variables are discretized, in this case considering only the displacement field. The kinematic field is approximated in terms of generalized nodal displacements, which are introduced into the expressions for internal work, equivalent decoupled thermal work, and external work.

$$\begin{aligned}\int_V \{\delta\boldsymbol{u}_{sj}\}^T F_s N_j[\boldsymbol{b}]^T[C][\boldsymbol{b}]F_\tau N_i\{\boldsymbol{u}_{\tau i}\}dV = \\ = \int_V \{\delta\boldsymbol{u}_{sj}\}^T F_s N_j[\boldsymbol{b}]^T\{\lambda\}\theta dV + \int_V \{\delta\boldsymbol{u}_{sj}\}^T F_s N_j\{\boldsymbol{g}\}dV\end{aligned} \tag{5.47}$$

Following the standard procedure adopted in purely mechanical analyses, the generalized nodal displacements are extracted from the integral expressions, leading to the discrete formulation. By applying the polynomial identity principle to the summation over the indices s and j, the governing algebraic system of equations is obtained.

$$\int_V [\boldsymbol{B}^{sj}]^T[C][\boldsymbol{B}^{\tau i}]dV]\{\boldsymbol{u}_{\tau i}\} = \int_V [\boldsymbol{B}^{sj}]^T\{\lambda\}\theta dV + \int_V F_s N_j\{\boldsymbol{g}\}dV \tag{5.48}$$

$$[\boldsymbol{K}^{\tau sij}]\{\boldsymbol{u}_{\tau i}\} = \{\boldsymbol{T}^{sj}\} + \{\boldsymbol{F}^{sj}\} \tag{5.49}$$

The vector T represents the equivalent nodal load vector, energetically consistent with the work produced by the temperature field acting on the virtual displacements.

When the temperature distribution is known a priori, it is not necessary to couple the structural analysis with the heat diffusion problem in order to determine the temperature field within the body. The plate is thermally loaded by prescribing a temperature distribution over the mid-plane θ_Ω. The temperature field is

$$\theta(x, y, z) = \theta_z \cdot \theta_\Omega \tag{5.50}$$

The through-thickness temperature profile θ_Ω is usually linear in thin structures and exponential in the case of a bisinusoidal in-plane temperature field θ_Ω. For plate-like structures whose thickness is small compared to their in-plane dimensions, the resulting temperature profile varies linearly along the thickness coordinate z:

$$\theta_z = \theta_{bot} + \frac{\theta_{top} - \theta_{bot}}{h}(z + \frac{h}{2}) \tag{5.51}$$

where $z \in [-h/2, h/2]$ The quantities θ_{top} and θ_{bot} generally correspond to the prescribed thermal boundary conditions, and the temperature varies linearly between these two values.

5.2.3 Coupled approach

With the coupled approach the PVD can be formulated as follows:

$$\int_V (\{\delta\varepsilon\}^T\{\boldsymbol{\sigma}\} - \{\delta\tilde{\theta}\}^T \cdot \{\boldsymbol{q}\} - \{\delta\theta\} \cdot \eta)dV = \delta L_{ext} \tag{5.52}$$

Here, $\tilde{\theta}$ denotes the temperature gradient, $\{\boldsymbol{q}\}$ represents the heat flux vector and η indicates the entropy produced by thermal exchange associated with a virtual variation of temperature. In analogy with stresses and strains, both the temperature gradient and the heat flux are written in compact vector form.

$$\tilde{\theta} = \begin{Bmatrix} \frac{\partial}{\partial x} \\ \frac{\partial}{\partial y} \\ \frac{\partial}{\partial z} \end{Bmatrix} \theta = [\boldsymbol{d}]\theta \tag{5.53}$$

$$\{q\} = \begin{bmatrix} K_{11} & K_{12} & 0 \\ K_{12} & K_{22} & 0 \\ 0 & 0 & K_{33} \end{bmatrix} \tilde{\theta} = [K][\boldsymbol{d}]\theta \tag{5.54}$$

The entropy response must be specified through a constitutive assumption, whereas the heat flux is governed by the classical theory of heat conduction. The linear elastic constitutive relation, the heat flux and the entropy are described as follow:

$$\{\sigma\} = [C][\boldsymbol{b}]\{\boldsymbol{u}\} - \{\lambda\}\theta \tag{5.55}$$

$$\{q\} = [K]\tilde{\theta} = [K][\boldsymbol{d}]\theta \tag{5.56}$$

$$\{\eta\} = \{\lambda\}^T\{\varepsilon\} + \chi\theta = \{\lambda\}^T[\boldsymbol{b}]\{\boldsymbol{u}\} + \chi\theta \tag{5.57}$$

where $\chi = \frac{c_v\rho}{T_0}$ Hamilton's principle can be reformulated accordingly.

$$\begin{gathered}\int_V \{\delta\boldsymbol{u}\}^T[\boldsymbol{b}]^T[C][\boldsymbol{b}]\{\boldsymbol{u}\}dV - \int_V \{\delta\boldsymbol{u}\}^T[\boldsymbol{b}]^T\{\lambda\}\theta dV + \\ + \int_V \delta\theta[\boldsymbol{d}]^T[K][\boldsymbol{d}]\theta dV - \int_V \delta\theta\{\lambda\}^T[\boldsymbol{b}]\{\boldsymbol{u}\}dV - \int_V \delta\theta\chi\theta dV = \delta L_{ext}\end{gathered} \tag{5.58}$$

As previously done, the problem variables—namely the displacement components and the temperature field—are discretized, and the individual contributions are examined separately. The FN of the stiffness matrix obtained from mechanical strain energy is:

$$\begin{aligned}\int_V \{\delta\boldsymbol{u}\}^T[\boldsymbol{b}]^T[C][\boldsymbol{b}]\{\boldsymbol{u}\}dV = \{\delta\boldsymbol{u}_{sj}\}^T\Big[\int_V [\boldsymbol{B}^{sj}]^T[C][\boldsymbol{B}^{\tau i}]dV\Big]\{\boldsymbol{u}_{\tau i}\} = \\ = \{\delta\boldsymbol{u}_{sj}\}^T[\boldsymbol{K}_{uu}^{\tau sij}]\{\boldsymbol{u}_{\tau i}\}\end{aligned} \tag{5.59}$$

The FN of the stiffness matrix obtained from thermally induced stresses is

$$\begin{aligned}\int_V \{\delta\boldsymbol{u}_{sj}\}^T F_s N_j[\boldsymbol{b}]^T\{\lambda\}\theta dV = \{\delta\boldsymbol{u}_{sj}\}^T\Big[\int_V [\boldsymbol{B}^{sj}]^T\{\lambda\}F_\tau N_i dV\Big]\theta_{\tau i} = \\ = \{\delta\boldsymbol{u}_{sj}\}^T[\boldsymbol{K}_{s\theta}^{\tau sij}]\theta_{\tau i}\end{aligned} \tag{5.60}$$

The FN of the stiffness matrix obtained from energy associated with heat flux is

$$\int_V \delta\theta[\boldsymbol{d}]^T[K][\boldsymbol{d}]\theta dV = \delta\theta_{sj}\Big[\int_V [\boldsymbol{D}^{sj}]^T[K][\boldsymbol{D}^{\tau i}]dV\Big]\theta_{\tau i} = \delta\theta_{sj}[\boldsymbol{K}_{\theta\theta}]_1^{\tau sij}\theta_{\tau i} \tag{5.61}$$

The entropy due to the displacement field results in the FN of a coupling matrix:

$$\int_V \delta\theta\{\lambda\}^T[\boldsymbol{b}]\{\boldsymbol{u}\}dV = \delta\theta_{sj}\Big[\int_V F_s N_j\{\lambda\}^T[\boldsymbol{B}^{\tau i}]dV\Big]\{\boldsymbol{u}_{\tau i}\} = \delta\theta_{sj}[\boldsymbol{K}_{\theta u}^{\tau sij}]\{\boldsymbol{u}_{\tau i}\} \tag{5.62}$$

Entropy due to temperature variations defines a purely thermal matrix component

$$\int_V \delta\theta\chi\theta dV = \delta\theta_{sj}\Big[\int_V F_s N_j\chi F_\tau N_i dV\Big]\theta_{\tau i} = \delta\theta_{sj}[\boldsymbol{K}_{\theta\theta}^{\tau sij}]_2 \tag{5.63}$$

Compact representation of the resulting equivalent algebraic system

$$\begin{bmatrix} [K_{uu}] & [K_{u\theta}] \\ [K_{\theta u}] & [K_{\theta\theta}] \end{bmatrix} \begin{Bmatrix} \{u\} \\ \{\theta\} \end{Bmatrix} = \begin{Bmatrix} \{F\} \\ \{0\} \end{Bmatrix} \tag{5.64}$$

where

$$[K_{\theta\theta}] = [K_{\theta\theta}]_1 + [K_{\theta\theta}]_2 \tag{5.65}$$

Chapter 6

Sub-array preliminary models and thermo-elastic analysis results

This study focuses on the structural response of a complex sub-array model operation in a geostationary environment, as anticipated in the introduction chapter, in which the structure is subjected to a thermal gradient of $\Delta\theta = 100K$. Therefore, the results obtained from an uncoupled thermo-elastic analysis, corresponding to Procedure 199, are presented. Prior to the investigation of the complete model, in this chapter a series of preliminary configurations was examined in order to assess the stability and reliability of the numerical code in performing uncoupled thermo-elastic analyses. This validation was carried out through systematic comparisons with results obtained using ABAQUS. The analysis of the sub-array is therefore conducted by progressively increasing the level of model complexity. In particular, four configurations are considered:

- triangular sub-array with four ultra-thin layers;
- a triangular plate model including only dielectric patches;
- a triangular plate model consisting of both substrate and patches characterized by different different in-plane geometries;
- a triangular plate model consisting of a more elaborate copper foil and RT/Duroid 5880 substrate and patches witout the microstrip lines .

The geometry and material properties are described in the corresponding subsection for each model, together with the applied boundary conditions.

6.1 Triangular sub-array with four ultra-thin layers

6.1.1 Problem set-up and model description

The triangular plate model under investigation has a base of 200 mm, a height of 100 mm and inclined sides of 144.4 mm, as shown in Figure 6.1. The model is constrained by two clamped boundary conditions, located at the upper vertex of the triangular plate and at the midpoint of the base. From this point onward, a thermal load corresponding to $\Delta\theta = 100K$ is consistently applied.

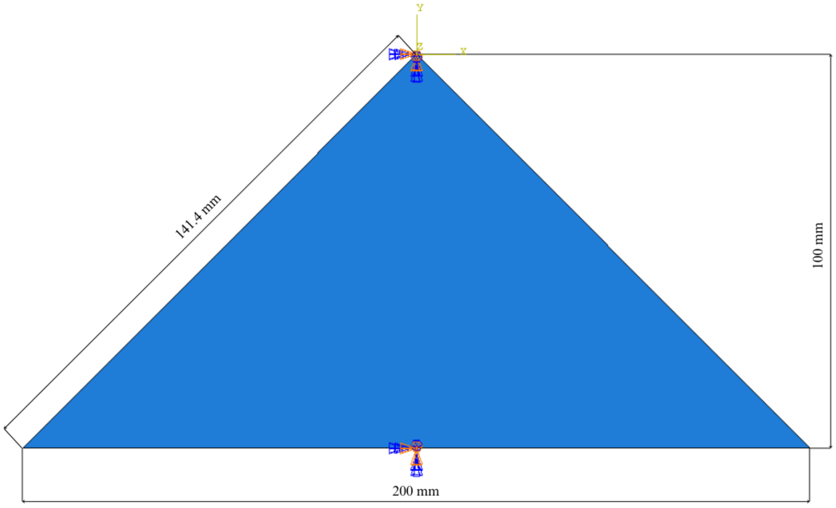

Figure 6.1: Plate model illustrating the geometric dimensions and boundary conditions implemented in the finite element simulation. (ABAQUS image)

The plate has a total thickness of 0.658 mm. In this model, the stacking sequence of materials intended for the final plate configuration has been maintained: CFRP fabric, Cu foil, RT/Duroid 5880 (dielctric material) and, finally, the outer Cu layer. The following tables report the mechanical and thermal properties of the individual materials together with their respective thickness.

Table 6.1: Layer configuration and thicknesses.

Layer	**Plate**	**Grounding**	**Dielectric**	**Antenna**
Material	CFRP fabric	Copper foil	RT/Duroid 5880	Copper foil
Thickness [mm]	0.08	0.035	0.508	0.035

Table 6.2: Mechanical and thermal properties: CFRP fabric details.

Young's Modulus E [MPa]	**Poisson's Ratio ν [-]**	**CTE $\alpha_{1,2}$ [-]**	**CTE α_3 [-]**
54900	0.182	1.44×10^{-7}	0

Table 6.3: Mechanical and thermal properties: Copper foil.

Young's Modulus E [MPa]	**Poisson's Ratio ν [-]**	**CTE α_1 [-]**
14000	0.34	1.60×10^{-5}

Table 6.4: Mechanical and thermal properties: RT/Duroid 5880 details.

E_1 **[MPa]**	E_2 **[MPa]**	E_3 **[MPa]**	ν **[-]**	G_{12} **[MPa]**	G_{13} **[MPa]**	G_{23} **[MPa]**	**CTE** $\alpha_{1,2,3}$
1076	863	938	0.34	517	308	451	4.0×10^{-5}

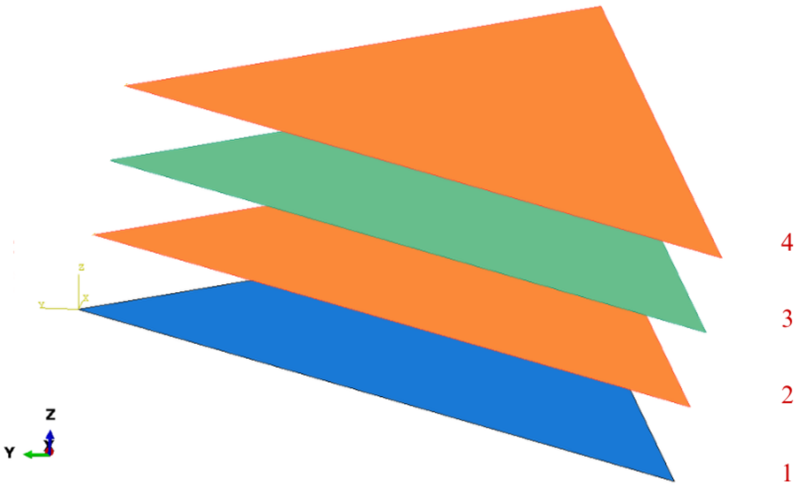

Figure 6.2: Layered configuration of the composite plate illustrating the arrangement of CFRP (blue), copper foil (orange), and RT/Duroid 5880 dielectric (green) layers

A 3D shell model was developed in Abaqus, consisting of an assembly of four parts, each representing one layer of the dub-array. The interacion between the layers is ensured by the presence of tie constraints between the corresponding surfaces. The number of nodes, number of S8R elements and degrees of freedom of the abaqus model are reported in Table 6.5.

Table 6.5: ABAQUS Model properties: Nodes, Elements, and Degrees of Freedom.

Total # of nodes	**Total # of elements**	**DOF**
17368	5572	104208

A distinction must be made between the ABAQUS model and the CUF models. The CUF models are developed using a single through-the-thickness expansion configuration, corresponding to the CFRP + Cu foil + RT/Duroid 5880 + Cu patches sequence. This assumption is justified by the absence of in-plane geometric variations across the considered layers, other than the thickness.

6.1.2 Convergence Analysis results

A convergence analysis was carried out by comparing CUF models based on Layer-Wise (LW) and Equivalent Single Layer (ESL) theories with the results obtained from the Abaqus model. Nine models were developed with in-plane meshes ranging from coarser to progressively finer to determine the configuration that yields the smallest relative percentage difference with respect to the Abaqus model. The Figure 6.3 shows the nine initial in-plane meshes used to construct the LW and ESL models. The Table 6.7 report the number of nodes and the total number of in-plane Q9 elements for each model.

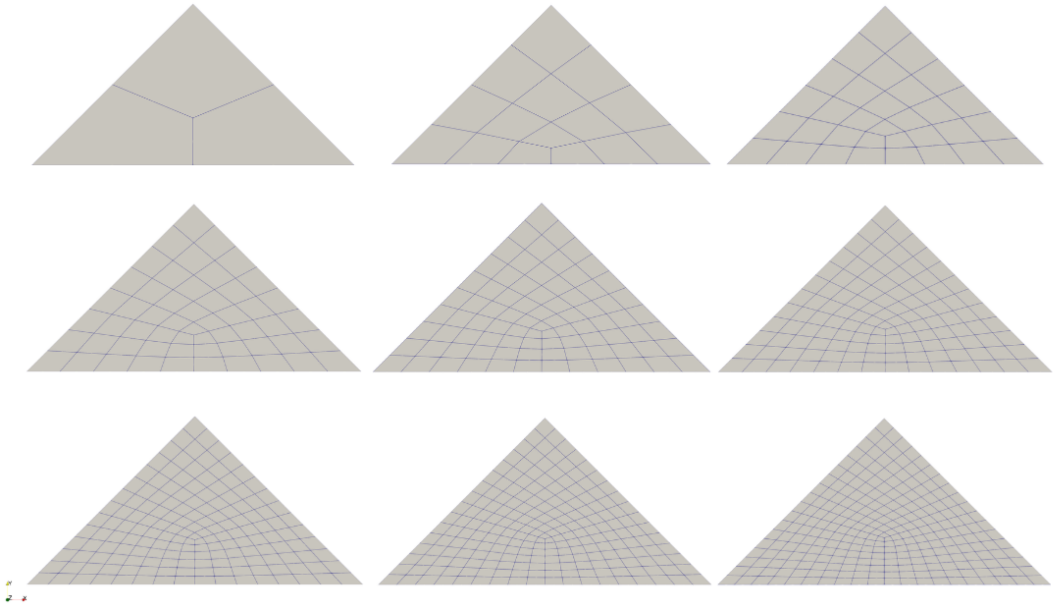

Figure 6.3: Initial Q9 in-plane meshes for the proposed LW and ESL CUF structural models.

The consistency between CUF and ABAQUS models, following uncoupled thermo-elastic analyses, is assessed by evaluating the out-of-plane displacement along the base of the triangular plate. In particular, the displacements at the vertices $(x, y) = (-100, -100)$ mm and $(x, y) = (100, -100)$ mm are considered. The comparison is performed using the percentage difference with respect to

Table 6.6: Finite Element Mesh details: Nodes and Q9 elements for the in-plane mesh per model.

Model	Total # of nodes	Total # of Q9 elements
1	19	3
2	75	15
3	149	32
4	247	55
5	369	84
6	515	119
7	685	160
8	879	207
9	1097	260

the ABAQUS model, defined as:

$$|\%Difference|w.r.t.ABQ = \frac{|u_{CUF} - u_{ABQ}|}{|u_{ABQ}|} \tag{6.1}$$

The metric is consistently adopted for all subsequent model comparisons.

The Figure 6.4, Figure 6.5, Figure 6.6 and Figure 6.7 show the convergence trends as a function of the number of in-plane Q9 elements and the degrees of freedom. Each curve corresponds to a different type and order of expansion and illustrates how the results vary accordingly. Taylor Expansions are used for ESL models and Lagrange expansions for LW models.

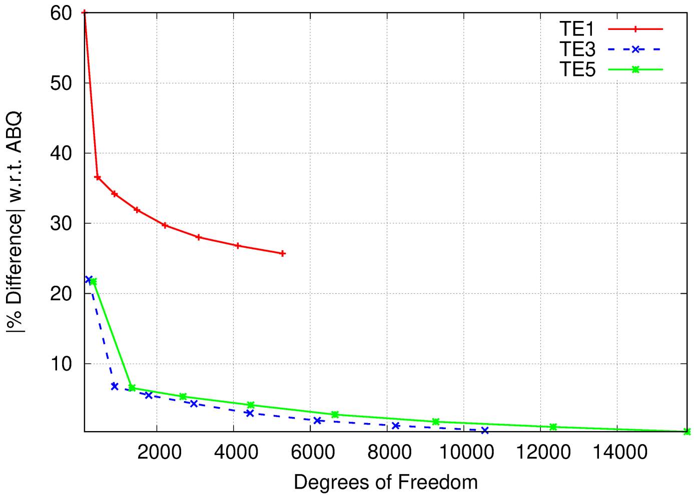

Figure 6.4: Relative percentage difference [%] w.r.t. ABAQUS model versus TE expansion order and number of DOF

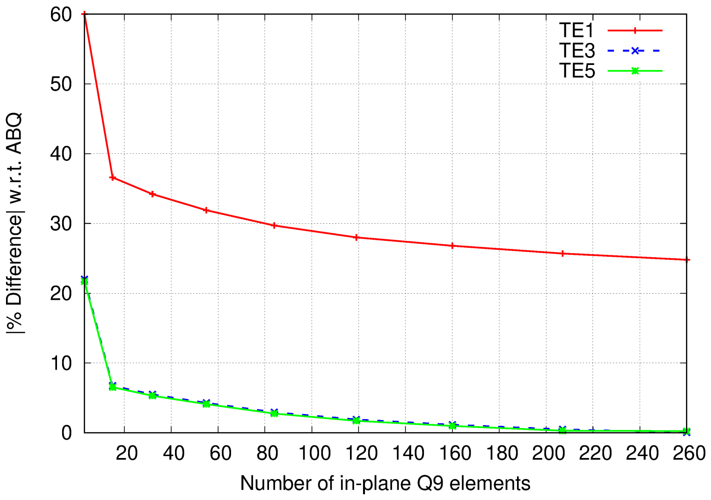

Figure 6.5: Relative percentage difference [%] w.r.t. ABAQUS model versus TE expansion order and number of elements

Table 6.7: Convergence analysis: TE 1 expansion.

Number of Elements	DOF	|Max Displacement| [mm]	|% Difference| w.r.t. ABQ
3	114	3.42×10^1	6.00×10^1
15	450	2.92×10^1	3.66×10^1
32	894	2.87×10^1	3.42×10^1
55	1482	2.82×10^1	3.19×10^1
84	2214	2.77×10^1	2.97×10^1
119	3090	2.73×10^1	2.80×10^1
160	4110	2.71×10^1	2.68×10^1
207	5274	2.68×10^1	2.57×10^1
260	6582	2.67×10^1	2.48×10^1

Table 6.8: Convergence analysis: TE 3 expansion.

Number of Elements	DOF	|Max Displacement| [mm]	|% Difference| w.r.t. ABQ
3	228	2.60×10^1	2.20×10^1
15	900	2.28×10^1	6.74×10^0
32	1788	2.25×10^1	5.50×10^0
55	2964	2.23×10^1	4.29×10^0
84	4428	2.20×10^1	2.94×10^0
119	6180	2.18×10^1	1.90×10^0
160	8220	2.16×10^1	1.16×10^0
207	10548	2.15×10^1	4.89×10^{-1}
260	13164	2.13×10^1	6.31×10^{-2}

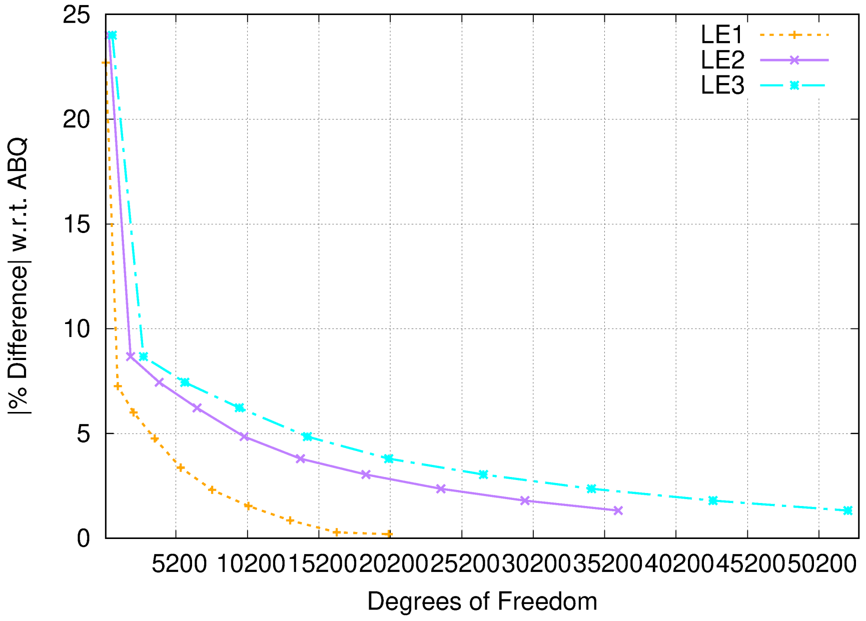

Figure 6.6: Relative percentage difference [%] w.r.t. ABAQUS model versus LE expansion order and number of DOF

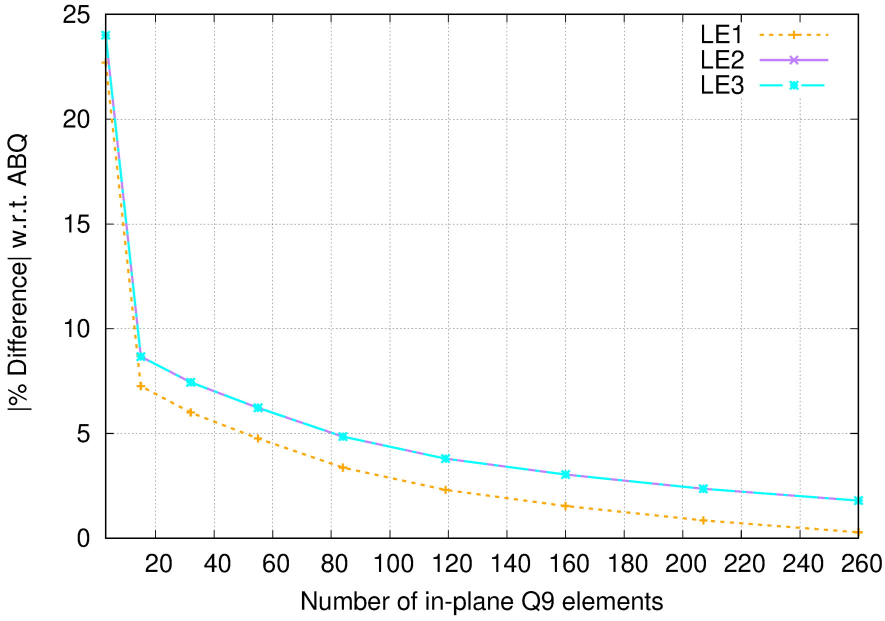

Figure 6.7: Relative percentage difference [%] w.r.t. ABAQUS model versus LE expansion order and number of elements

Table 6.9: Convergence analysis: TE 5 expansion.

Number of Elements	DOF	|Max Displacement| [mm]	|% Difference| w.r.t. ABQ
3	342	2.60×10^{1}	2.20×10^{1}
15	1350	2.27×10^{1}	6.74×10^{0}
32	2682	2.25×10^{1}	5.50×10^{0}
55	4446	2.22×10^{1}	4.29×10^{0}
84	6642	2.19×10^{1}	2.94×10^{0}
119	9270	2.17×10^{1}	1.90×10^{0}
160	12330	2.16×10^{1}	1.16×10^{0}
207	15822	2.14×10^{1}	4.89×10^{-1}
260	19746	2.13×10^{1}	6.31×10^{-2}

Table 6.10: Convergence analysis: LE 1 expansion.

Number of Elements	DOF	|Max Displacement| [mm]	|% Difference| w.r.t. ABQ
3	285	2.62×10^{1}	2.27×10^{1}
15	1125	2.29×10^{1}	7.26×10^{0}
32	2235	2.26×10^{1}	6.00×10^{0}
55	3705	2.24×10^{1}	4.76×10^{0}
84	5535	2.21×10^{1}	3.37×10^{0}
119	7725	2.18×10^{1}	2.31×10^{0}
160	10275	2.17×10^{1}	1.54×10^{0}
207	13185	2.15×10^{1}	8.55×10^{-1}
260	16455	2.14×10^{1}	2.84×10^{-1}

Table 6.11: Convergence analysis: LE 2 expansion.

Number of Elements	DOF	|Max Displacement| [mm]	|% Difference| w.r.t. ABQ
3	513	2.65×10^{1}	2.40×10^{1}
15	2025	2.32×10^{1}	8.67×10^{0}
32	4023	2.29×10^{1}	7.44×10^{0}
55	6669	2.27×10^{1}	6.22×10^{0}
84	9963	2.24×10^{1}	4.85×10^{0}
119	13905	2.22×10^{1}	3.80×10^{0}
160	18495	2.20×10^{1}	3.04×10^{0}
207	23733	2.19×10^{1}	2.36×10^{0}
260	29619	2.17×10^{1}	1.80×10^{0}

Table 6.12: Convergence analysis: LE 3 expansion.

Number of Elements	DOF	|Max Displacement| [mm]	|% Difference| w.r.t. ABQ
3	741	2.65×10^1	2.40×10^1
15	2925	2.32×10^1	8.67×10^0
32	5811	2.29×10^1	7.44×10^0
55	9633	2.27×10^1	6.23×10^0
84	14391	2.24×10^1	4.85×10^0
119	20085	2.22×10^1	3.80×10^0
160	26715	2.20×10^1	3.04×10^0
207	34281	2.19×10^1	2.36×10^0
260	42783	2.17×10^1	1.80×10^0

6.1.3 Macroscopic thermo-elastic deformation

The convergence analysis shows that the Layer-WIse and Equivalent Single Layer models that provide results closely matching those obtained with ABAQUS are the one developed with a third-order Taylor expansions and a First-order Lagrange expansions, both with 260 Q9 in-plane elements. From a theoretical standpoint, the most accurate models are generally those based on second- and third-order Lagrange expansions, which often yield comparable results, as will be shown in the following sections. In this case, the apparent agreement between the Layer-Wise LE1 model and the ABAQUS model is mainly attributed to the relatively coarse mesh adopted in ABAQUS. For subsequent models, it is observed that achieving results comparable to higher-order CUF Layer-Wise models requires a significantly refined ABAQUS mesh, with element sizes on the order of 1 mm or less. A slight discrepancy is observed near the clamped boundary at the base, likely due to local effects and mesh sensitivity.

Table 6.13: Best ESL Model: TE 3 expansion with 260 Q9 elements.

Number of Elements	DOF	|Max Displacement|	|% Difference| w.r.t. ABQ
260	16455	2.14×10^1	2.84×10^{-1}

Table 6.14: Best LW Model: LE 1 expansion with 260 Q9 elements.

Number of Elements	DOF	|Max Displacement|	|% Difference| w.r.t. ABQ
260	19746	2.13×10^1	6.31×10^{-2}

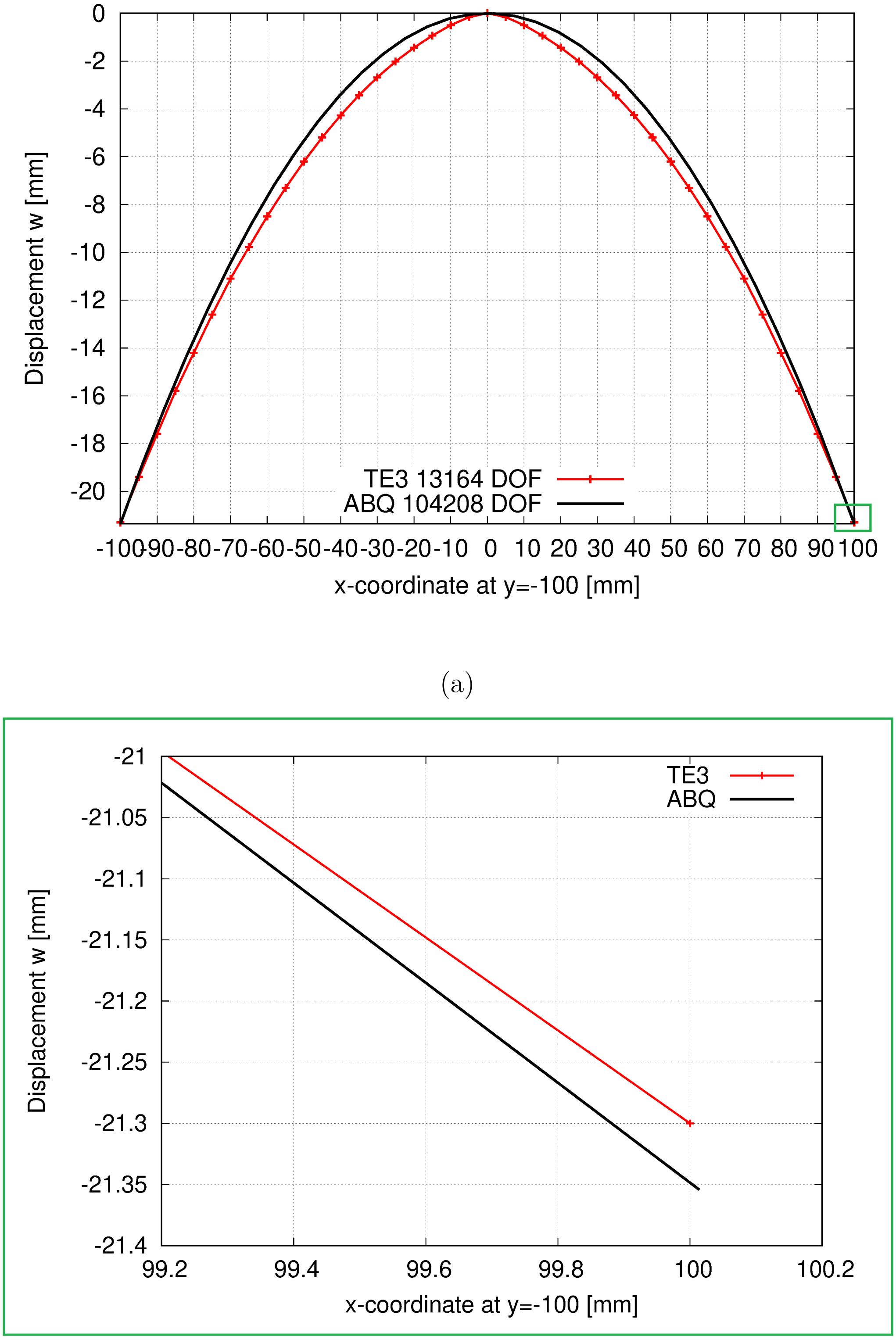

(a)

(b)

Figure 6.8: (a) Comparison of out-of-plane displacement under a 100 K thermal load between the Abaqus model and the selected third-order TE expansion model yielding the best results; (b) Displacement detail at (100,-100)

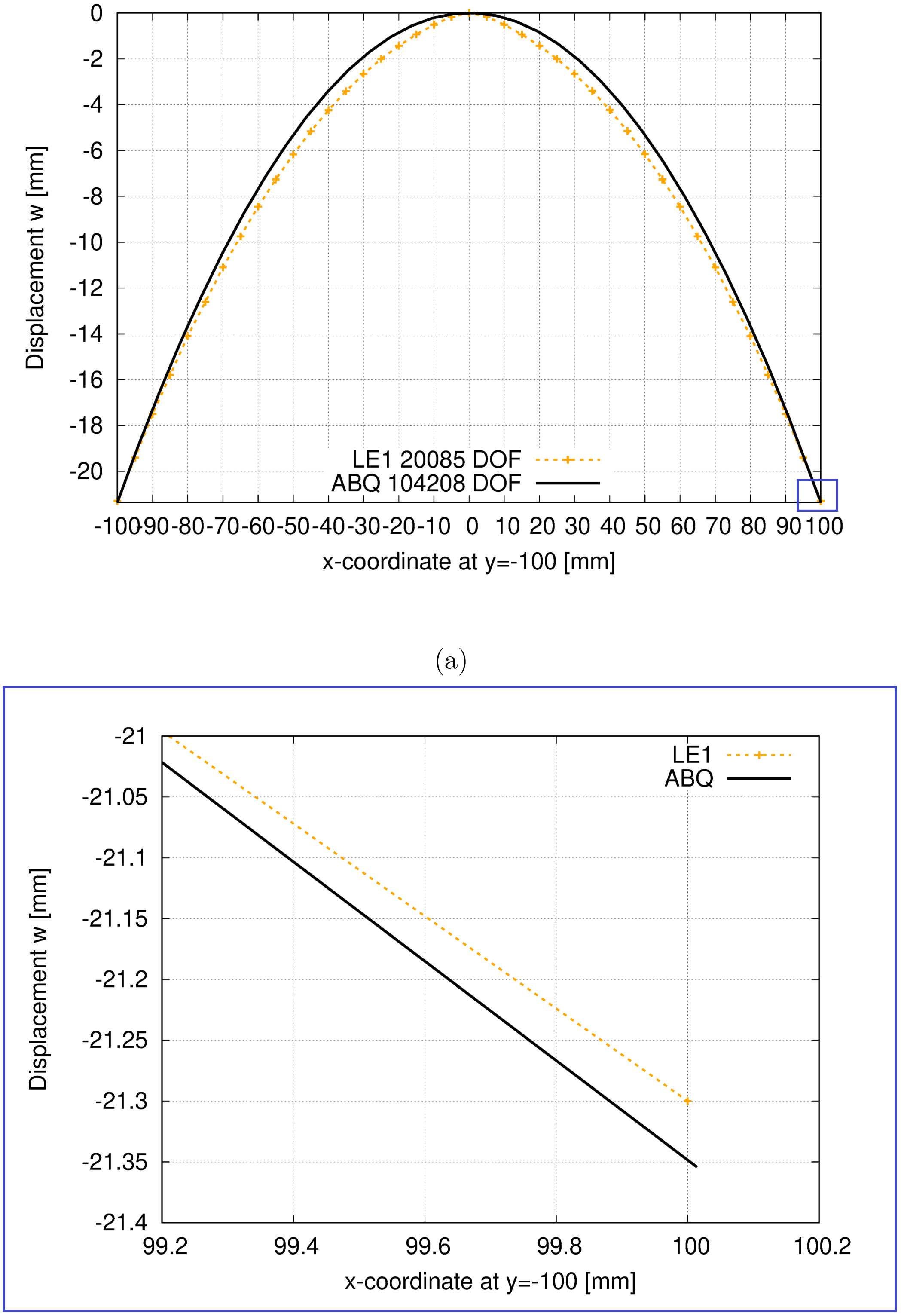

(a)

(b)

Figure 6.9: (a) Comparison of out-of-plane displacement under a 100 K thermal load between the Abaqus model and the selected first-order LE expansion model yielding the best results; (b) Displacement detail at (100,-100)

6.2 Triangular sub-array with two ultra-thin layers with two in-plane geometries

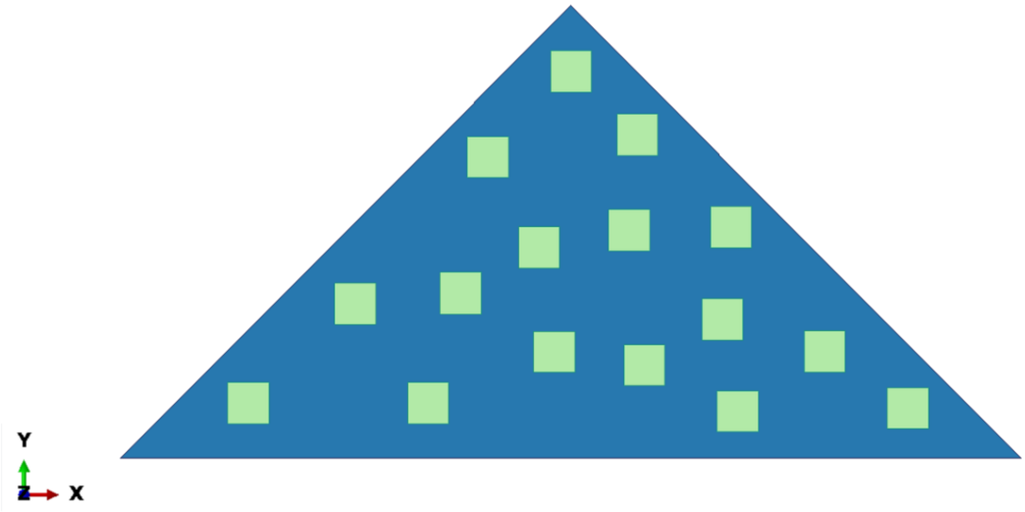

Figure 6.10: Sub-array ABAQUS model illustrating the layered configuration of CFRP plate (blue) and RT/Duroid 5880 layer (green)

In this section, a simplified representation of the subarray is introduced. The electrical circuits and the reference support structure have been neglected in order to isolate the structural behavior. At this preliminary stage, the model consists of two layers only, corresponding to the CFRP plate and the DUROID dielectric patches. The in-plane discretization of the CUF model has been progressively refined, starting from a coarse mesh and moving toward finer configurations. A convergence analysis has been performed to determine the mesh density that guarantees a close agreement with the benchmark results obtained using ABAQUS. It should be emphasized that shell elements have been employed for both the CUF-based models and the ABAQUS reference analyses. For each in-plane mesh configuration, both Layer-Wise (LW) and Equivalent Single Layer (ESL) models with different expansion orders have been implemented and compared. As a result of the convergence study, the most effective configuration was identified as the Layer-Wise (LW) model based on a second-order Lagrange Expansion (LE). The comparison among the different formulations has been primarily carried out in terms of the total number of degrees of freedom (DOFs) required by each model.

In this section, particular attention is devoted to the comparison of the transverse displacements along the z-axis between the CUF-based models and the ABAQUS results.

6.2.1 Problem set-up and model description

In the present case, the analysis focuses on the influence of the dielectric layer on the deformation of the plate. This layer exhibits anisotropic properties and represents the thickest component, as previously reported. The triangular plate, maintaining the same global dimensions, includes square dielectric patches with side lengths of approximately 8 mm. The boundary condition adopted for this and subsequent models consists of a clamped constraint that restricts both displacements and rotations in all directions, applied near the center of the plate and shifted by 2 mm along the positive x-axis As a result, the displacement field exhibits a slight asymmetry, also influenced by the non-uniform distribution of the patches.

Table 6.15: ABAQUS Model properties: Nodes, Elements, and Degrees of Freedom.

Total # of nodes	Total # of elements	DOF
10412	3299	62472

Table 6.16: Mesh characteristics for CFRP fabric and RT/Duroid 5880 substrate

	CFRP fabric	RT/Duroid 5880
Number of nodes	9372	1040
Number of elements	3093	256

Table 6.17: Materials mechanical and thermal properties

Layer	**2**	**1**
Material	**RT/Duroid 5880**	**CFRP fabric**
Thickness [mm]	0.5	0.1
Young's Modulus E [GPa]	0.9	50
Poisson's Ratio ν [-]	0.3	0.2
CTE α [K^{-1}]	4.0×10^{-5}	1.44×10^{-7}

CUF models with different in-plane meshes are used, whose characteristics are reported Table 6.18. Regarding the through-the-thickness expansions, two configurations are considered: CFRP laminate expansions and CFRP + RT/Duroid 5880 expansions.

Table 6.18: Finite Element Mesh details: Nodes and Q9 elements for the in-plane mesh per model.

Model	Total # of nodes	Total # of Q9 elements
1	1131	264
2	2369	562
3	2687	637
4	2881	705
5	3895	939

6.2.2 Convergence Analysis results

The convergence analysis is performed considering five different in-plane meshes for the CUF model, from which both Layer-Wise (LW) and Equivalent Single Layer (ESL) formulations are derived. The most accurate results are obtained using Layer-Wise models based on second- and third-order Lagrange expansions, with an in-plane discretization consisting of 705 Q9 elements. Since these models provide nearly identical results, the optimal choice is the LE2 model, due to its lower computational cost.

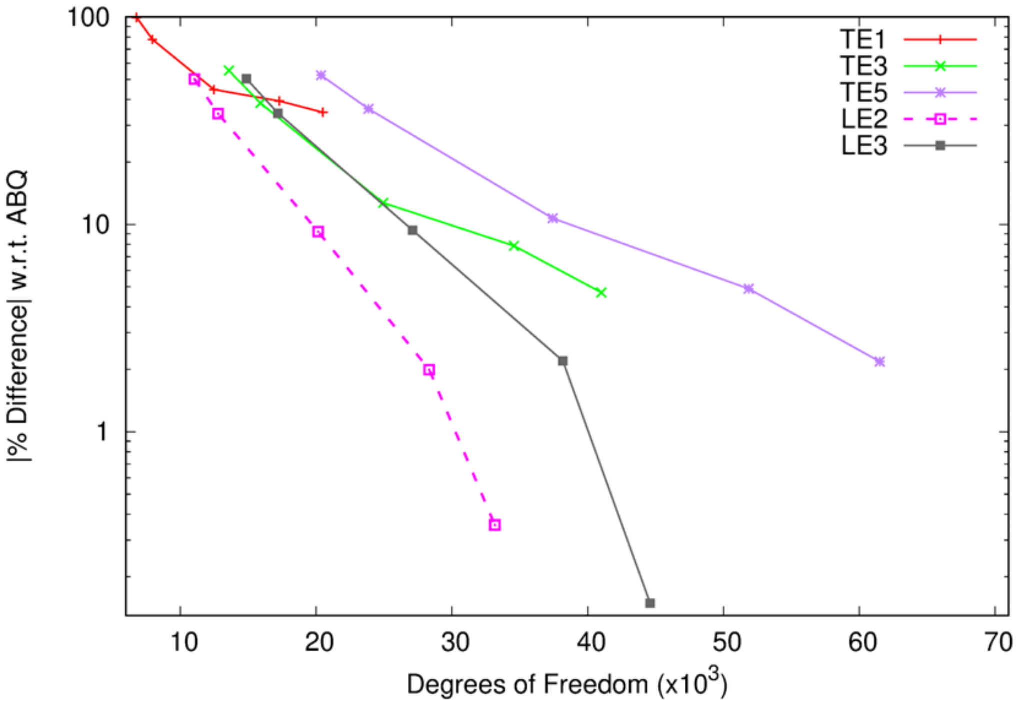

Figure 6.11: Relative percentage error [%] versus expansion order and number of DOF, showing faster convergence and higher accuracy with CUF high-order expansions.

Table 6.19: Maximum displacement obtained through a TE 1 order expansion at the left vertex $(-100, -100)$ and the corresponding |% Difference| w.r.t. ABQ.

DOF	**|Maximum displacement| [mm]**	**|% Difference| w.r.t. ABQ**
6786	15.16	9.96×10^1
7950	13.52	7.79×10^1
12474	11.00	4.47×10^1
17286	10.59	3.94×10^1
20502	10.23	3.47×10^1

Table 6.20: Maximum displacement obtained through a LE2 order expansion at the left vertex $(-100, -100)$ and the corresponding |% Difference| w.r.t. ABQ

DOF	**|Maximum displacement| [mm]**	**|% Difference| w.r.t. ABQ**
11043	11.41	5.02×10^1
12789	10.20	3.42×10^1
20151	8.30	9.23×10^0
28329	7.75	1.99×10^0
33153	7.57	3.55×10^{-1}

6.2.3 Macroscopic thermo-elastic deformation

The Figure 6.12 illustrates the out-of-plane displacement distribution for both Layer-Wise and ESL models based on the optimal 705-element mesh. Except for the TE1 model, which exhibits the lowest accuracy, both LW and ESL approaches provide results consistent with the reference solution, while significantly reducing computational cost. These results confirm that the linear thermo-elastic response of the structure is accurately captured.

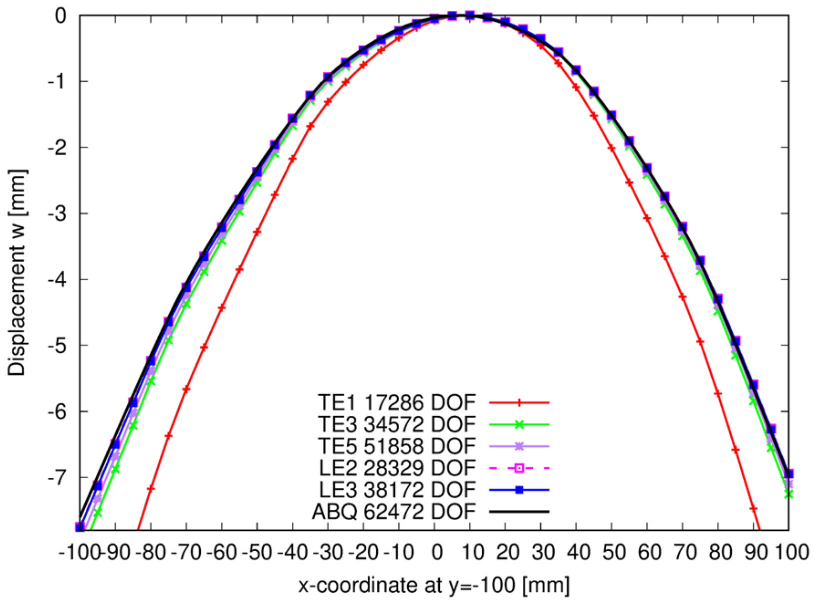

Figure 6.12: Out-of-plane displacement under a thermal load of 100 K: comparison between TE expansions, LE expansions and ABAQUS model results with respective DOF

Table 6.21: CUF model characteristics and thermo-elastic analysis results with TE

Exp. Order	**DOF**	**|Disp. w| at (-100,-100) [mm]**	**|% Diff.| wrt ABQ**	**|Disp. w| at (100,-100)[mm]**	**|% Diff.| wrt ABQ**
TE 1	17286	1.06×10^1	3.94×10^1	6.25×10^0	3.28×10^1
TE 3	34572	8.19×10^0	7.89×10^0	3.73×10^0	3.78×10^0
TE 5	51858	7.97×10^0	4.89×10^0	3.27×10^0	1.59×10^0

Table 6.22: CUF model characteristics and thermo-elastic analysis results with LE

Exp. Order	**DOF**	**|Disp. w| at (-100,-100)**	**|% Diff.| wrt ABQ**	**|Disp. w| at (100,-100)**	**|% Diff.| wrt ABQ**
LE 2	28329	7.75×10^0	1.99×10^0	6.25×10^0	7.50×10^{-1}
LE 3	38172	7.76×10^0	2.19×10^0	3.27×10^0	5.60×10^{-1}

The displacement field of the optimal LE2 model is visually compared with the ABAQUS results, showing excellent agreement, as confirmed by the contour plots.

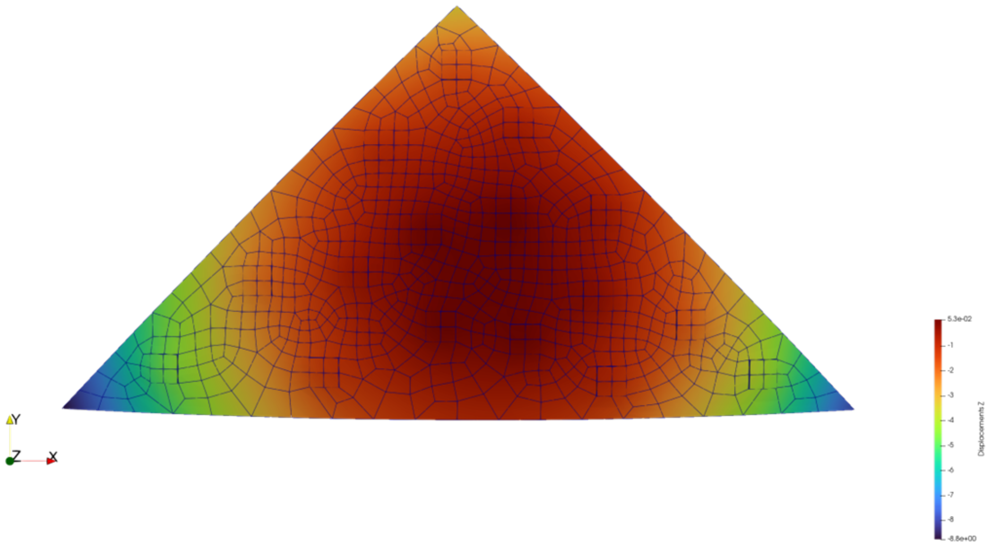

Figure 6.14: CUF out-of-plane displacement under a thermal load of 100 K using Lagrange Expansion of the second order

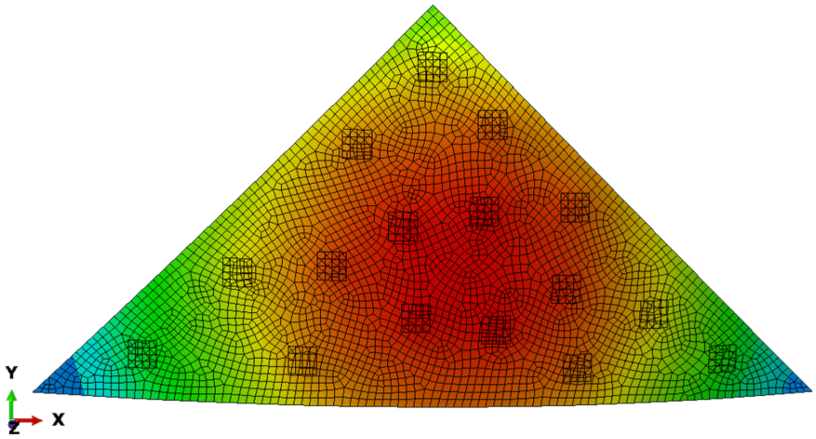

Figure 6.13: ABAQUS out-of-plane displacement under a thermal load of 100 K

|Displacement w| at (-100, -100) [mm]	**|Displacement w| at (100, -100) [mm]**
7.6	6.99

Table 6.23: ABAQUS displacement results at (x,y)=(-100,-100) and (x,y)=(100,-100)

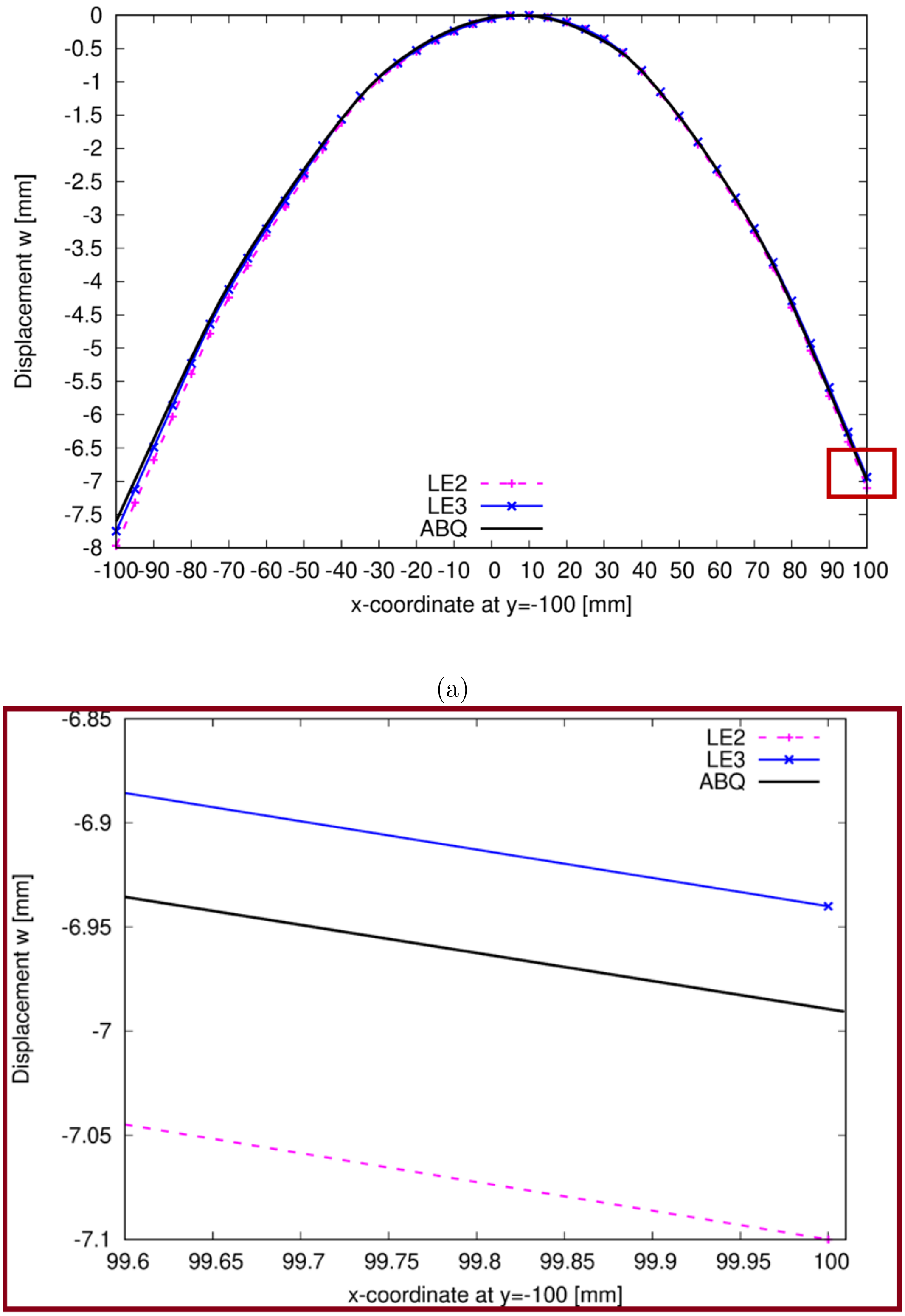

(a)

(b)

Figure 6.15: (a) Out-of-plane displacement under a thermal load of 100 K: comparison between LE expansion models and ABAQUS model results with respective DOF. (b) Displacement detail at (100,-100)

6.3 Triangular sub-array with four ultra-thin layers with three in-plane geometries

The complexity of the problem is progressively increased in this model. The same boundary conditions are retained, with the addition of two layers: a copper foil layer positioned between the CFRP plate and the Duroid dielectric, and copper patches representing the actual antenna. The substrate, composed of copper and dielectric layers, has slightly larger dimensions than the patches and serves as their base

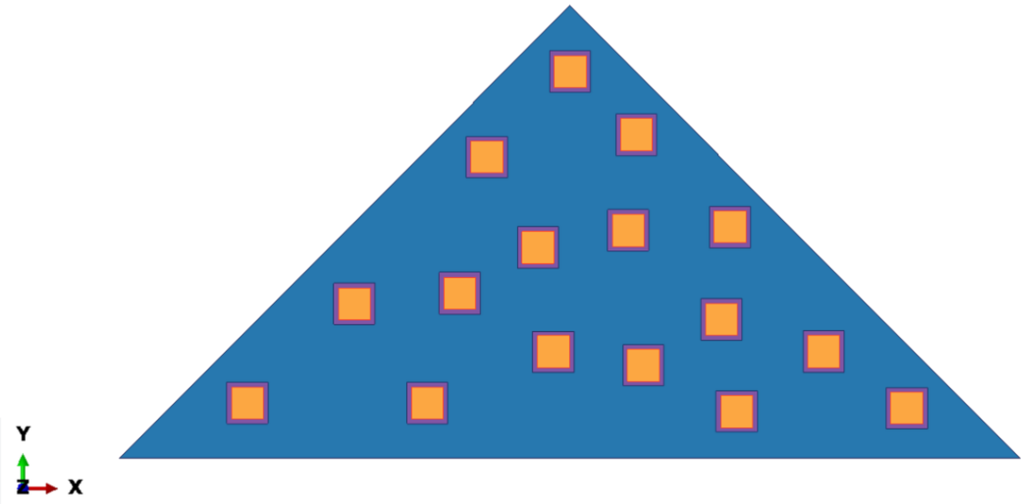

Figure 6.16: Sub-array ABAQUS model illustrating the layered configuration of CFRP plate (blue), copper foil + RT/Duroid 5880 layer (purple) and copper patches (orange)

6.3.1 Problem set-up and models description

In ABAQUS, this model is constructed using three separate parts assembled together and connected via tie costraints: the CFRP plate, the substrate defined as composite lay-up of copper foil and Duroid and the patches layer. This modeling strategy ensures proper coupling between the components, enabling the analysis of bending–torsional deformation behavior. The ABAQUS model is discretized using quadrilateral S8R elements with a characteristic size of approximately 1 mm, ensuring a level of accuracy consistent with the complexity of the model.

Table 6.24: ABAQUS model mesh characteristics

Total # of nodes	Total # of elements
21166	126996

Table 6.25: Abaqus model: nodal and elemental distribution per layer.

	CFRP fabric	**Copper foil 1 + RT/Duroid 5880**	**Patches**
Number of nodes	16910	2128	2128
Number of elements	5529	576	576

The CUF model adopts the in-plane mesh characteristics reported in the table. For the through-the-thickness expansions, three configurations are considered:

- CFRP laminate expansions;
- CFRP + Cu foil + RT/Duroid 5880 expansions;
- CFRP + Cu foil + RT/Duroid 5880 + Cu patches expansions.

Table 6.26: CUF model mesh characteristics

Total # of nodes	**Total # of elements**
3173	768

The layers thickness are reported in Table 6.1, while materials' properties are reported in Table 6.2, Table 6.3 and Table 6.4.

6.3.2 Macroscopic thermo-elastic deformation

Due to the applied constraints and the distribution of the patches, the displacement field is asymmetric. Therefore, the percentage difference with respect to the ABAQUS model is evaluated for the out-of-plane displacement at both vertices of the triangular base.

Table 6.27: ABAQUS model characteristics and thermo-elastic analysis results

DOF	**|Displacement w| at (-100, -100) [mm]**	**|Displacement w| at (100, -100) [mm]**
126996	8.81	8.25

Both CUF Equivalent Single Layer (ESL) and Layer-Wise (LW) models were developed. As shown in Table 6.28 and Table 6.29, the model based on first-order Taylor expansions is not able to accurately capture the displacement field, exhibiting a difference of approximately 22% compared to the ABAQUS model. In contrast, the TE3 and TE5 models provide accurate predictions with a reduced number of degrees of freedom.

Table 6.28: CUF model characteristics and thermo-elastic analysis results with TE

Exp. Order	**DOF**	**|Disp. w| at (-100,-100)**	**|% Diff.| wrt ABQ**	**|Disp. w| at (100,-100)**	**|% Diff.| wrt ABQ**
TE 1	19038	1.12×10^{1}	2.68×10^{1}	1.03×10^{1}	2.53×10^{1}
TE 3	38076	8.77×10^{0}	4.62×10^{-1}	8.20×10^{0}	5.90×10^{-1}
TE 5	57114	8.79×10^{0}	$1.71 \times 10-1$	8.32×10^{0}	8.66×10^{-1}

A similar trend is observed for the Layer-Wise models, for which a reduced percentage difference is already achieved using first-order Lagrange expansions. As discussed previously, the most accurate model is expected to be LE3, which shows only a marginal improvement compared to LE2. Since both models exhibit a percentage difference of less than 1% with respect to the ABAQUS solution, the LE2 model is identified as the optimal choice due to its lower computational cost.

Table 6.29: CUF model characteristics and thermo-elastic analysis results with LE

Exp. Order	**DOF**	**|Disp. w| at (-100,-100)**	**|% Diff.| wrt ABQ**	**|Disp. w| at (100,-100)**	**|% Diff.| wrt ABQ**
LE 1	26964	8.28×10^{0}	6.00×10^{0}	7.81×10^{0}	5.25×10^{0}
LE 2	44409	8.77×10^{0}	4.19×10^{-1}	8.31×10^{0}	7.28×10^{-1}
LE 3	61854	8.78×10^{0}	3.03×10^{-1}	8.32×10^{0}	9.06×10^{-1}

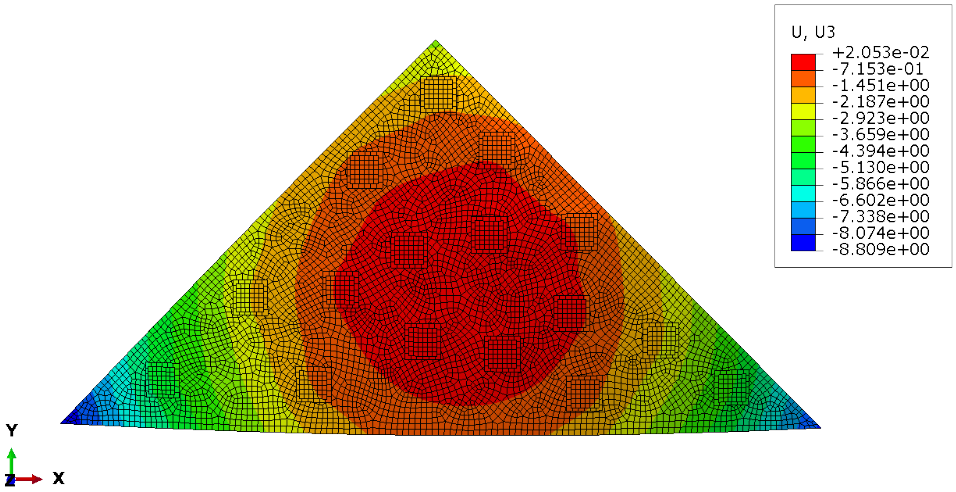

Figure 6.17: ABAQUS out-of-plane displacement under a thermal load of 100 K

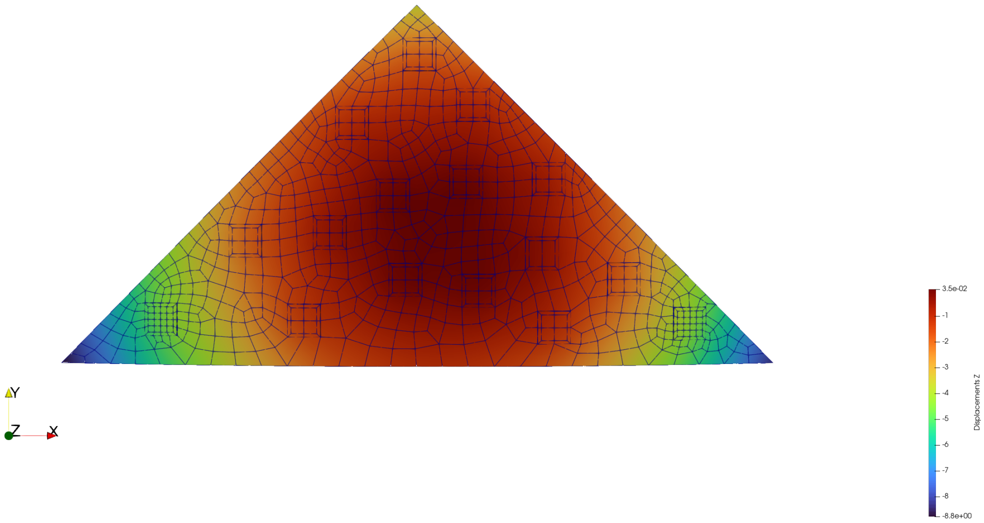

Figure 6.18: CUF out-of-plane displacement under a thermal load of 100 K using Lagrange Expansion of the second order

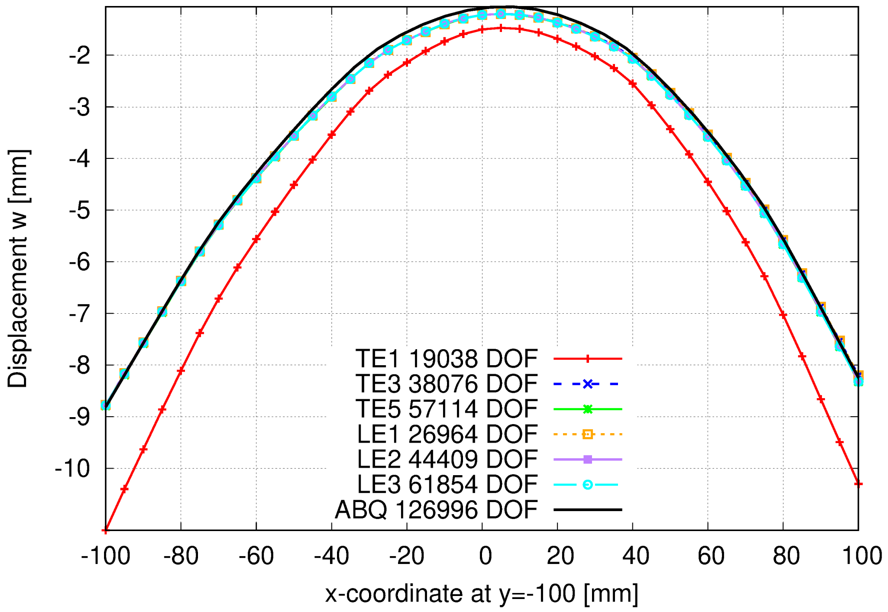

Figure 6.19: Out-of-plane displacement under a thermal load of 100 K: comparison between TE expansions, LE expansions and ABAQUS model results with respective DOF

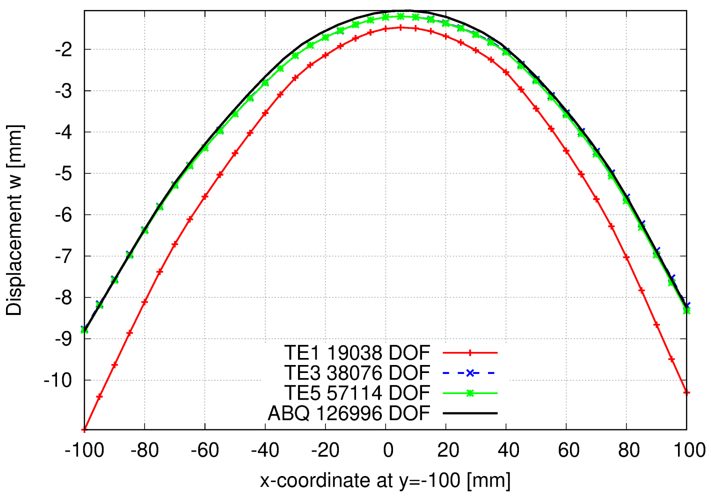

Figure 6.20: Out-of-plane displacement under a thermal load of 100 K: comparison between TE expansions and ABAQUS model results with respective DOF

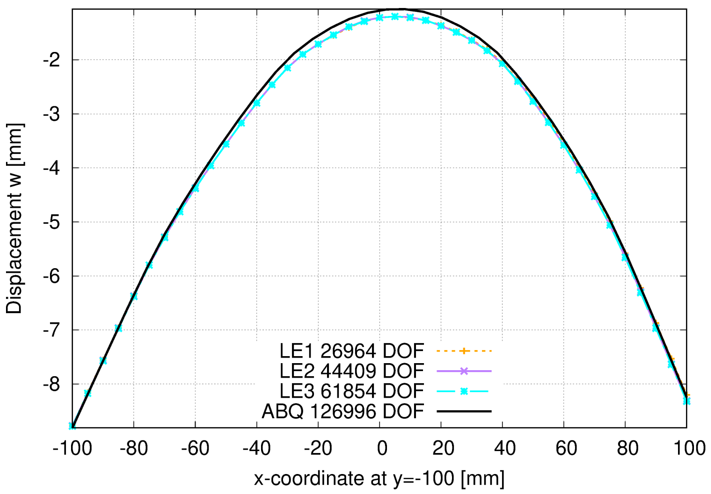

Figure 6.21: Out-of-plane displacement under a thermal load of 100 K: comparison between TE expansions, LE expansions and ABAQUS model results with respective DOF

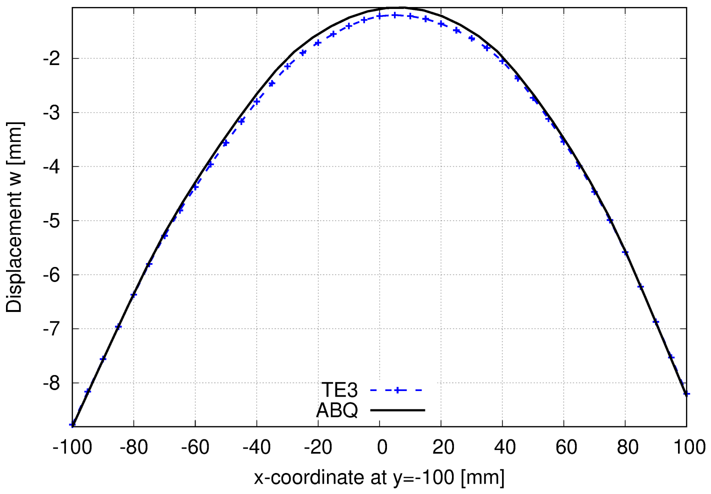

Figure 6.22: Out-of-plane displacement under a thermal load of 100 K: comparison between third order TE expansion and ABAQUS model results.

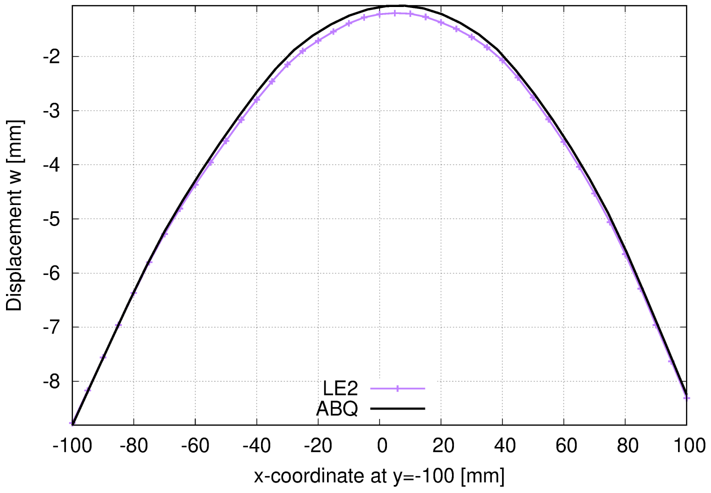

Figure 6.23: Out-of-plane displacement under a thermal load of 100 K: comparison between second order LE expansion and ABAQUS model results.

6.4 Development of the final model without microstrips lines

This chapter presents the development of the final finite element model of the triangular plate with dielectric patches without microstrips. The structural configuration consists of the four physical layers previously introduced: a CFRP fabric laminate, a copper foil layer, a dielectric substrate made of RT/Duroid 5880 and radiating copper patches bonded to the dielectric layer three different in-plane geometries.

6.4.1 ABAQUS Shell Model

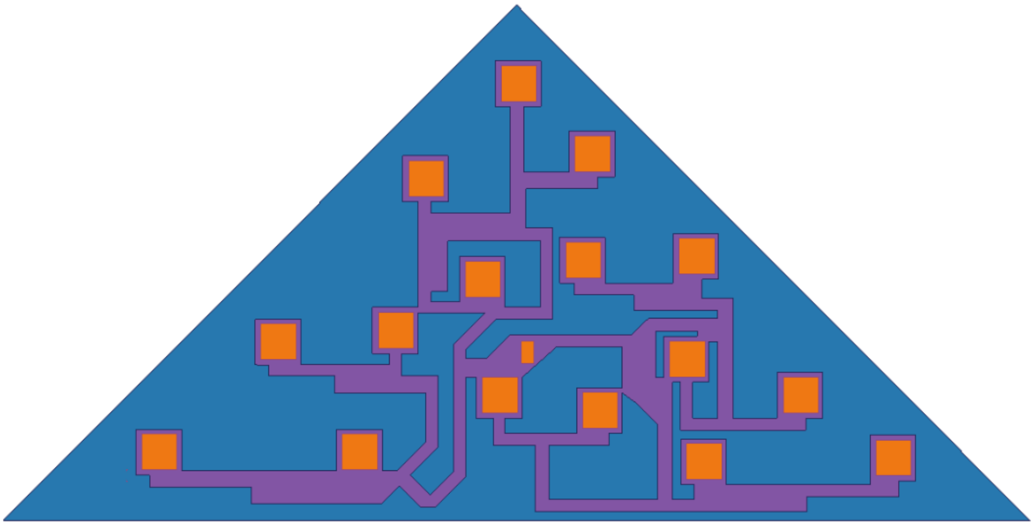

Figure 6.24: ABAQUS model

The ABAQUS model was developed using three distinct 3D planar shell sections:

- a shell section representing the CFRP laminate;
- a shell section representing the combined copper foil and dielectric substrate, modeled with a composite layup and serving as support for the radiating patches;
- a shell section corresponding to the radiating copper patches.

Table 6.30: ABAQUS model mesh characteristics

Total # of nodes	Total # of elements
52641	16730

Each layer was discretized using quadratic quadrilateral reduced-integration shell elements (S8R). A refined in-plane mesh, with element side lenghts ranging from 1 mm to 2 mm, was adopted for all layers to ensure adequate resolution of the displacement field. The use of quadratic elements is motivated by the need to accurately capture the mechanical response of a geometrically thin multilayered structure, where bending-membrane coupling effects may be non-negligible.

Table 6.31: Abaqus model: nodal and elemental distribution per material.

	CFRP fabric	**Copper foil 1 + RT/Duroid 5880**	**Patches**
Number of nodes	37236	12538	2867
Number of elements	12251	3683	796

6.4.2 CUF model

A Carrera Unified Formulation (CUF) model is subsequently developed for comparison purposes. Three through-the-thickness expansions configurations are considered:

- CFRP laminate expansion;
- CFRP+Cu foil+RT/Duroid 5880 expansion;
- CFRP+CU foilRT/Duroid 5880 + Cu patches expansion.

The CUF framework allows an enriched kinematic description along the thickness direction through hierarchical expansions of the displacement field. Owing to this refined through-thickness representation, a coarser in-plane mesh based on Q9 elements. with sizes ranging from 1 mm to 5 mm, can be employed without compromising accuracy.

Table 6.32: CUF model mesh characteristics

Total # of nodes	**Total # of elements**
6111	1495

Nevertheless, local in-plane mesh refinement was introduced in correspondence with the two lateral patches. This refinement was implemented to enable detailed evaluation of the through-the-thickness stress components in those regions, while avoiding the need for separate submodel. Both Layer Wise and Equivalent Single Layer formulations were implemented using the same in-plane discretization to ensure consistency in the comparative assessment. The layers thickness are reported in Table 6.1, while materials' properties are reported in Table 6.2, Table 6.3 and Table 6.4.

6.4.3 Macroscopic thermo-elastic deformation

In this section, the results of the uncoupled thermo-elastic analysis of the triangular sub-array model, including the full substrate composed of copper foil and a dielectric layer, are presented. At this stage of modeling, certain features increase the difficulty of achieving convergence between the ABAQUS model and the CUF model. This also reflected in the results, which show that the ABAQUS model requires a higher number of elements, nodes and, consequently, degrees of freedom compared to the CUF model. From a computational standpoint, the CUF model allows for more efficient and straightforward analyses. As in the previous cases, the displacement field along the z-axis under thermal loading is taken as the reference quantity to asses the consistency between the ABAQUS and CUF models. In particular, the displacement of the nodes located at the base of the triangular plate was considered.

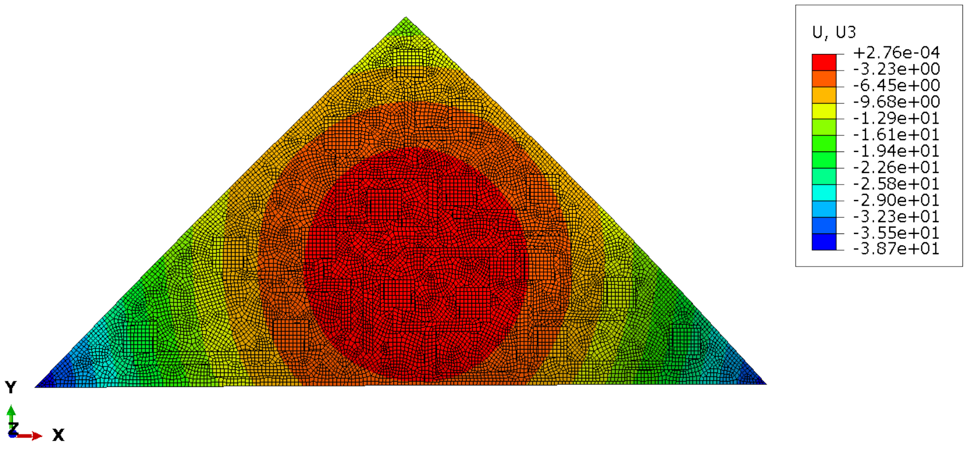

Figure 6.25: ABAQUS model results

Table 6.33: ABAQUS model characteristics and thermo-elastic analysis results

DOF	|Displacement w| at (-100, -100) [mm]	|Displacement w| at (100, -100) [mm]
315846	38.49	37.23

Table 6.34: CUF characteristics and thermo-elastic analysis results: TE models.

Exp. Order	DOF	|Disp. w| at (-100,-100)	|% Diff.| wrt ABQ	|Disp. w| at (100,-100)	|% Diff.| wrt ABQ
TE 1	36666	5.06×10^1	3.15×10^1	4.77×10^1	2.81×10^1
TE 3	73332	3.97×10^1	3.25×10^0	3.75×10^1	8.52×10^{-1}
TE 5	109998	3.97×10^1	3.04×10^0	3.75×10^1	6.96×10^{-1}

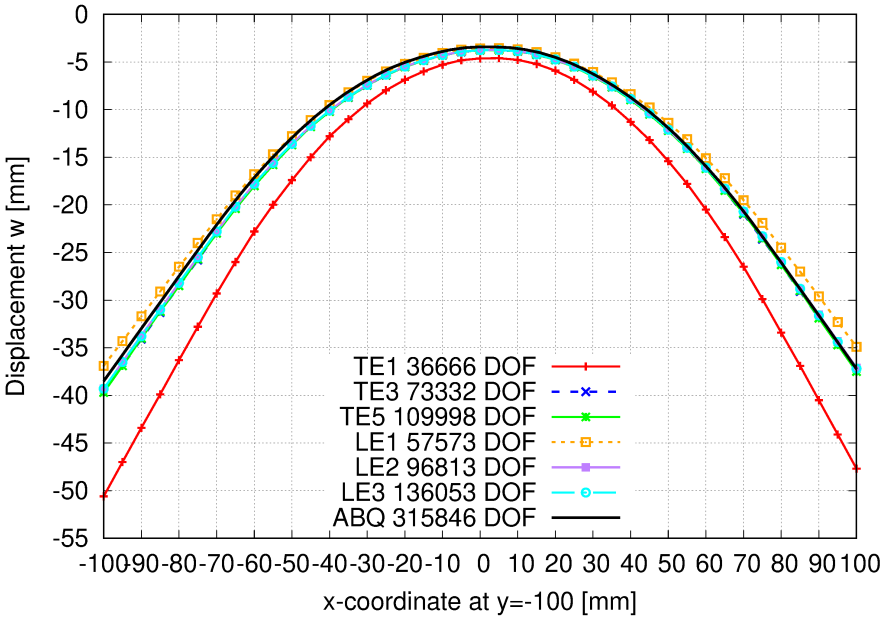

Figure 6.26: Out-of-plane displacement: comparison between TE expansions, LE expansions and ABAQUS model results with respective DOF

Table 6.35: CUF characteristics and thermo-elastic analysis results: LE models.

Exp. Order	**DOF**	**|Disp. w| at (-100,-100)**	**|% Diff.| wrt ABQ**	**|Disp. w| at (100,-100)**	**|% Diff.| wrt ABQ**
LE 1	57573	3.69×10^1	4.03×10^0	3.49×10^1	6.31×10^0
LE 2	96813	3.93×10^1	2.08×10^0	3.71×10^1	2.68×10^{-1}
LE 3	136053	3.93×10^1	2.17×10^0	3.72×10^1	1.94×10^{-1}

In particular, two models are highlighted: a LW model and an ESL model. Both, identified as optimal configurations, exhibit relative differences with respect to the ABAQUS model at the two non-coincident ends, with slightly different magnitudes. This discrepancy is mainly due to the imperfect correspondence between the boundary conditions adopted in the ABAQUS and CUF models. When the use of an ESL model is reuquired, it emerges that, in terms of both computational efficiency and accuracy, a model based on third-order Taylor expansions is recommended. In the case of a LW approach, a model based on second-order Lagrange expansions is considered optimal. As shown in Table 6.35, the LE 2 and LE 3 models are approximately equivalent, and therefore the LE 2 model is selected as the optimal Layer-Wise (LW) model.

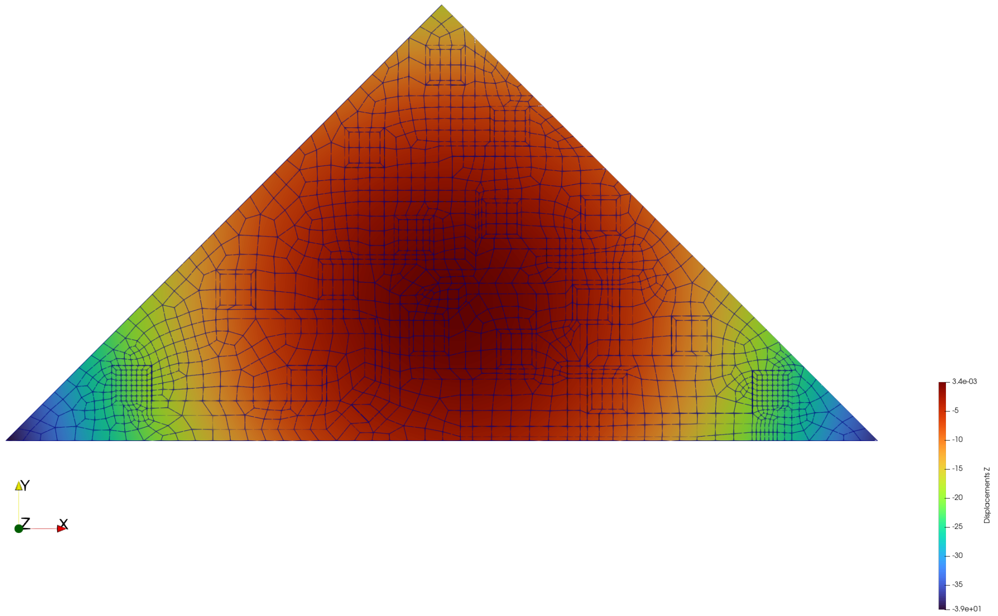

Figure 6.27: CUF out-of-plane displacement under a thermal load of 100 K using Lagrange Expansion of the second order

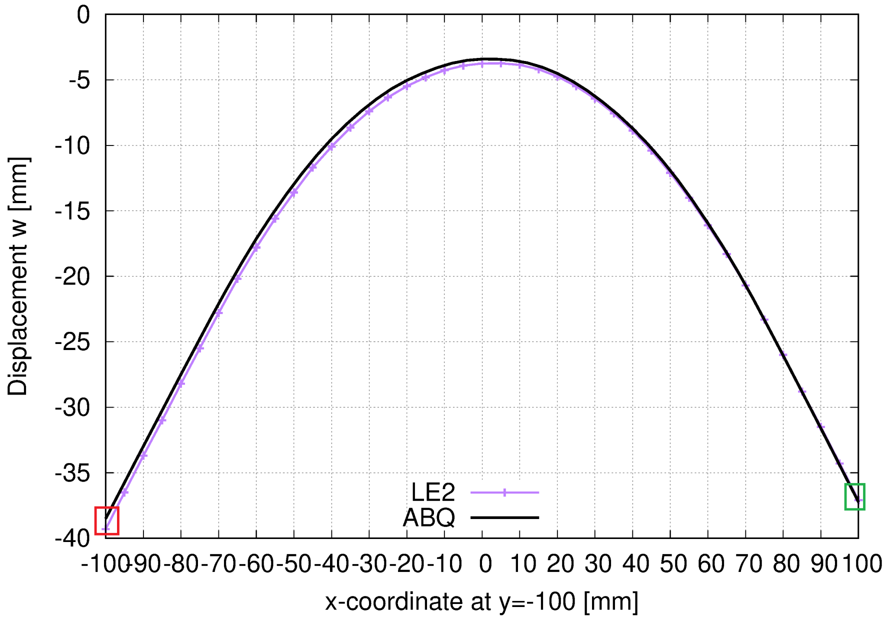

Figure 6.28: Out-of-plane displacement: comparison between TE expansions, LE expansions and ABAQUS model results with respective DOF

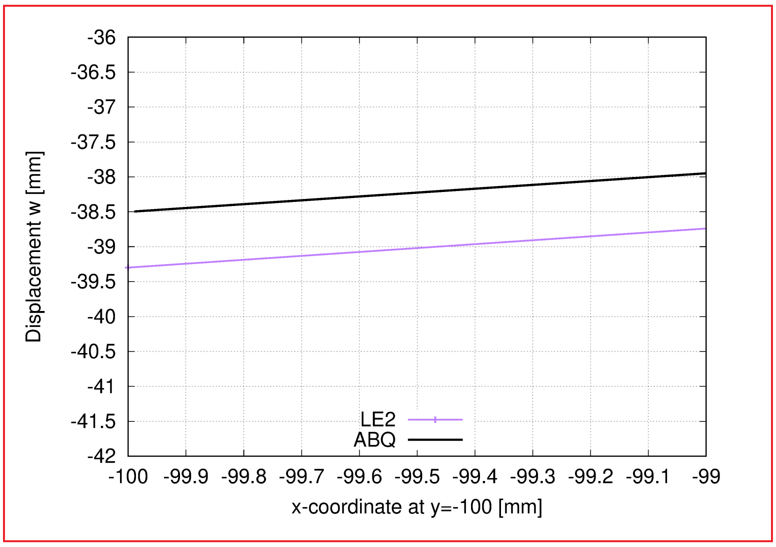

(a)

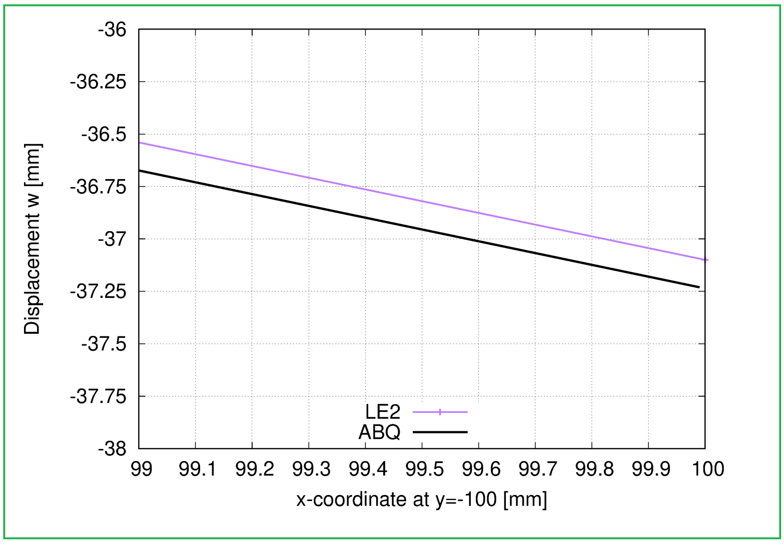

(b)

Figure 6.29: (a) Displacement detail at (-100,-100), (b) Displacement detail at (100,-100)

Table 6.36: Selected best LE expansion model results.

Exp. Order	**DOF**	**|Disp. w| (-100,-100)**	**% Diff. vs ABQ**	**|Disp. w| (100,-100)**	**% Diff. vs ABQ**
LE 2	96813	3.93×10^1	2.08×10^0	3.71×10^1	2.68×10^{-1}

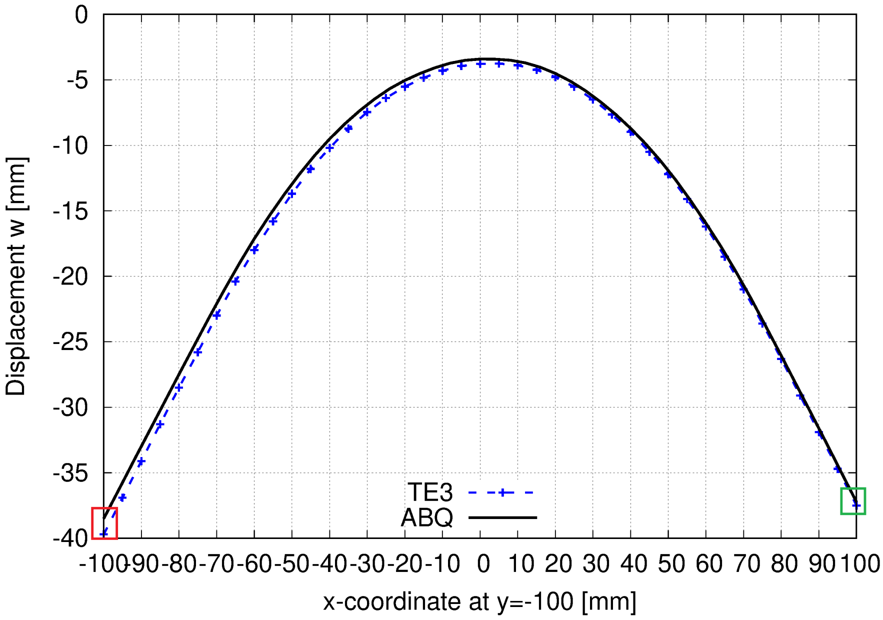

Figure 6.30: Out-of-plane displacement: comparison between third-order TE expansion model and ABAQUS model results

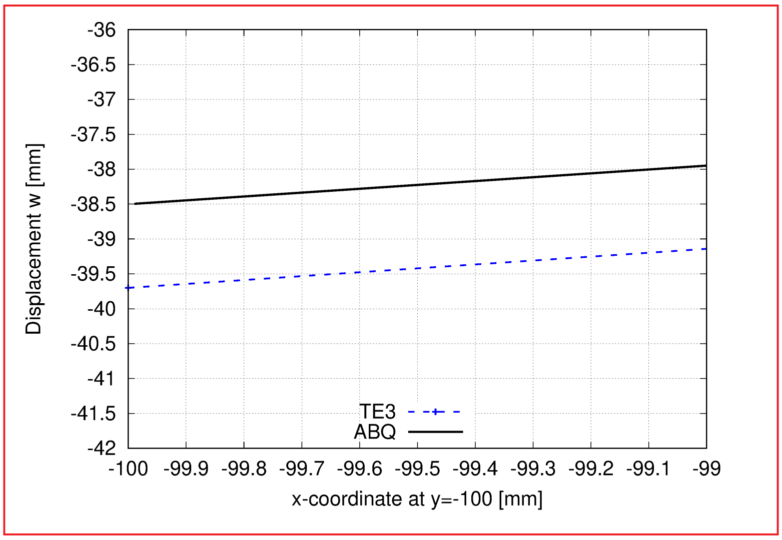

(a)

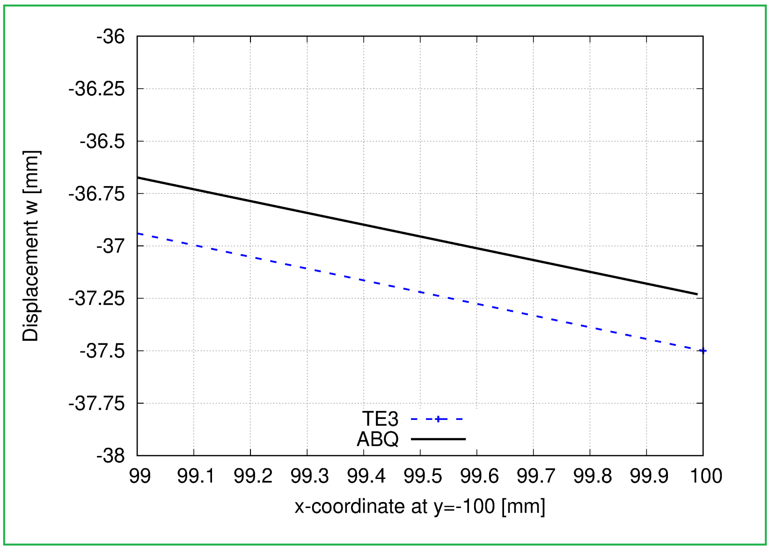

(b)

Figure 6.31: Out-of-plane displacement detail for TE 3 model: (a) at (-100,-100); (b) at (100,-100)

Table 6.37: Selected best TE expansion model results.

Exp. Order	**DOF**	**|Disp. w| (-100,-100)**	**% Diff. vs ABQ**	**|Disp. w| (100,-100)**	**% Diff. vs ABQ**
TE 3	73332	3.97×10^1	3.25×10^0	3.75×10^1	8.52×10^{-1}

6.4.4 Through-the-thickness stress distributions

In this section, the results related to the analysis of through-the-thickness stress distributions near the free edge of two patches are presented. The selected patches, along with their corresponding nodes, are those experiencing the highest deformation and stress levels. For the investigation of the phenomena, it is necessary to refine the mesh along the thickness direction. As a reference parameter to assess whether the mesh is sufficiently refined, the σ_{zz} stress component is considered. in correspondence of the lower surface of the plate (z=0 mm) and at the upper surface of the patches (z=0.658 mm), the $\sigma_z z$ stress component is expected to be approximately zero.

From this point onward, the two reference patches for the through-thickness stress analysis are identified as "Patch 1" and "Patch2". The patch located at the left end is denoted as "Patch 1" and the node along whose thickness the stress distribution is evaluated has coordinates (x,y)=(-73.95, -90.23) mm. The patch at the right end is referred to as "Patch 2" and the corresponding node is located at (x,y)=(78.62, -91.67) mm. The following Figure 6.32 and

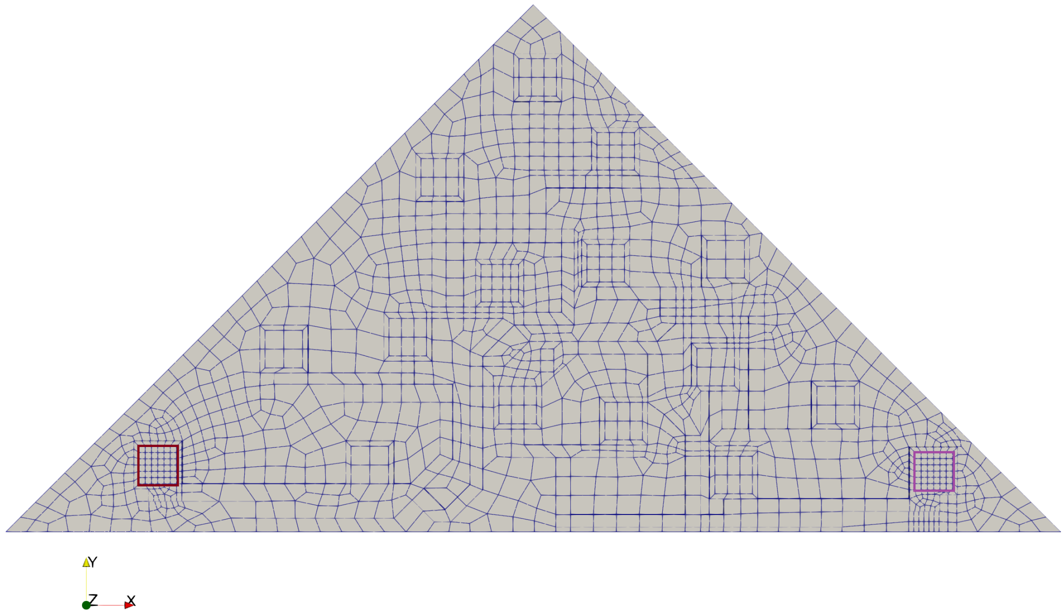

Figure 6.32: CUF model showing the analysed patches: "Patch 1" is highlighted in red, "Patch 2" is highlighted in purple

Figure 7.15 show the selected patches and the corresponding nodes considered in the analysis.

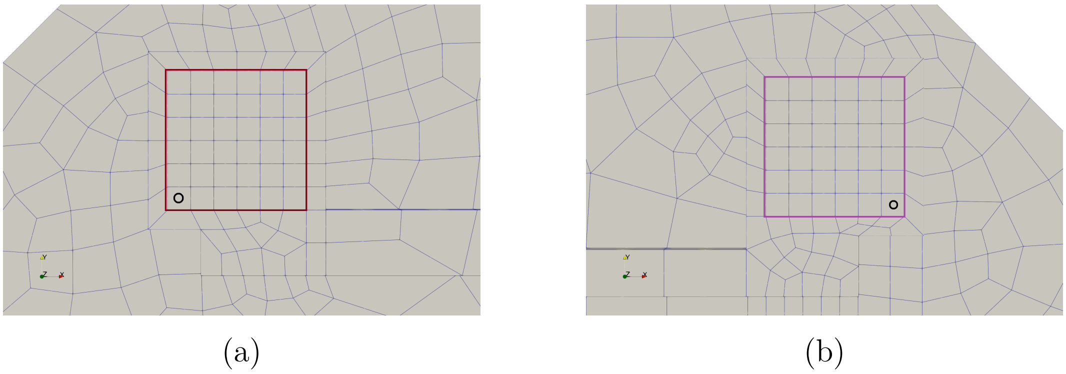
(a) (b)

Figure 6.33: (a) "Patch 1" and evaluated node (x,y)=(-73.95, -90.23) mm; (b) "Patch 2" and evaluated node (x,y)=(78.62, -91.67) mm

In this case, the ABAQUS model is not used as a direct reference for two main reasons. First, ABAQUS shell models are based on ESL formulations, where the thickness is defined as a section property. Each layer is used to study the global structural response and stresses are derived from the integration points through the thickness. Unlike CUF models, there are no separate degrees of freedom for each layer and, as a result, interlaminar stresses are reconstructed. They are often inaccurate, particularly for ultra-thin structures like those considered in this thesis. Second, while a 3D solid ABAQUS model could be used for this type of analysis, representing the structure with its actual volume and effectively producing a true Layer-Wise model, this approach has significant drawbacks. Although stress components, including interlaminar stresses, are naturally computed and accurate, the 3D solid model requires a very high number of elements and incurs substantial computational cost. Moreover, due to the thinness of the layers, shear-locking issues are often observed.

Patch 1

As anticipated in the introduction of this section, Layer-Wise models were developed using the same in-plane mesh while progressively increasing the number of elements through the thickness, adopting Lagrange expansions from first to third order. In the stress distribution plots for σ_{xx}, σ_{yy}, σ_{zz}, and σ_{xy}, each curve is associated with the element distribution adopted for each layer, reported in sequence from the CFRP layer to the Cu foil, the Duroid, and finally the top Cu layer. The thinner layers, namely the CFRP plate and the two copper layers, are discretized with up to three elements, whereas the thicker dielectric layer is discretized with up to 18 elements, depending on the expansion order considered. The results obtained from LE1, LE2, and LE3 models show a very high level of agreement. In all cases, the curves overlap almost perfectly already at intermediate mesh levels, indicating that the solution is stable and that excessive refinement along the thickness is not required. The σ_{zz} stress component is expected to be approximately zero, as prescribed by structural theories, and is therefore used as the key parameter for selecting an appropriate through-the-thickness discretization. It can be observed that the σ_{zz} results remain consistent despite variations in the number of elements through the thickness, with values close to zero as expected. The Table 6.38, Table 6.39 and Table 6.40 report stress values at the bottom and top surfaces of the sub-array, as well as at the interfaces between adjacent layers. The σ_{xy} component exhibits abrupt sign changes in correspondence with variations in the slope of the normal stress distributions, indicating localized transitions in the stress state. A singular behavior or change of regime is observed, with stresses rapidly transitioning from negative values to high positive peaks, up to approximately 30 MPa for σ_{yy},. Due to its reduced cross-section, the patch exhibits a behavior similar to that of a flange.

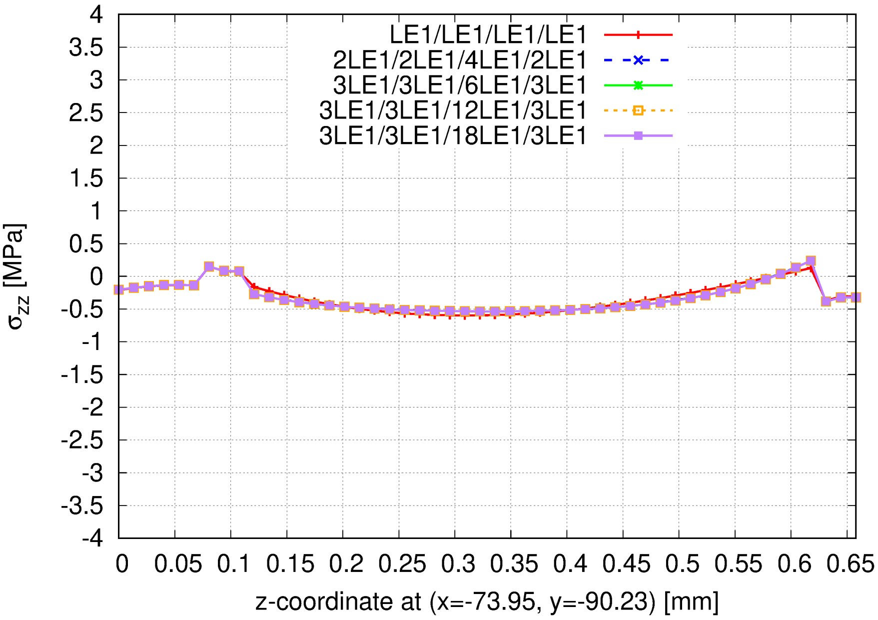

Figure 6.34: Effect of through-the-thickness mesh refinement on the σ_{zz} stress profile. The comparison between the baseline mesh ($LE1/LE1/LE1/LE1$) and the refined configurations (up to $3LE1/3LE1/18LE1/3LE1$) shows that the stress gradients are consistently captured, indicating a converged numerical solution

Table 6.38: Interlayer stress convergence results along the plate thickness at $(x, y) = (-73.95, -90.23)$ mm: First-Order Lagrange expansion

z-coordinate [mm]	σ_{zz}	σ_{xx}	σ_{yy}	σ_{xy}
0.000	-0.2	0	0	-5.2
0.080	0.1	-25.0	-25.0	0.4
0.115	-0.3	-4.0	-5.0	0.1
0.623	0.1	22.0	27.0	5.5
0.658	-0.3	24.0	30.0	6.0

From the analysis of the σ_{xx} and σ_{yy} components, a compressive stress state is observed at the interface between the CFRP layer and the copper foil at z=0.08mm, with a magnitude of about 25 MPa. At the upper surface of the patch (z=0.658 mm), the structure is subjected to a maximum tensile stress of approximately 29 MPa. The stress variation near this surface reflects the reduced area available for stress distribution, explaining the pronounced positive peaks.

Along the thickness of the dielectric material (0.115<z<0.623 mm), a region characterized by low and nearly constant normal stresses is observed, indicating

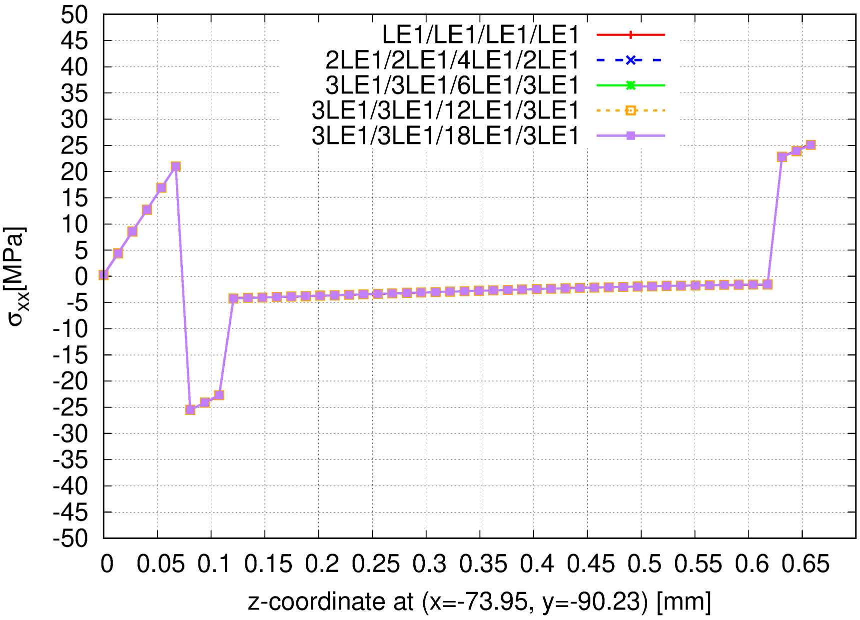

Figure 6.35: Effect of through-the-thickness mesh refinement on the σ_{xx} stress profile.

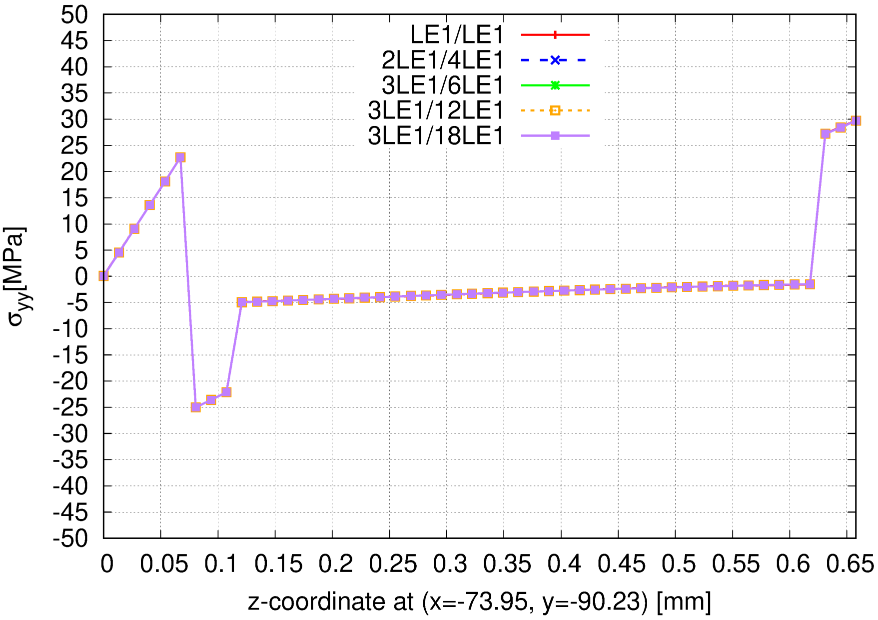

Figure 6.36: Effect of through-the-thickness mesh refinement on the σ_{yy} stress profile.

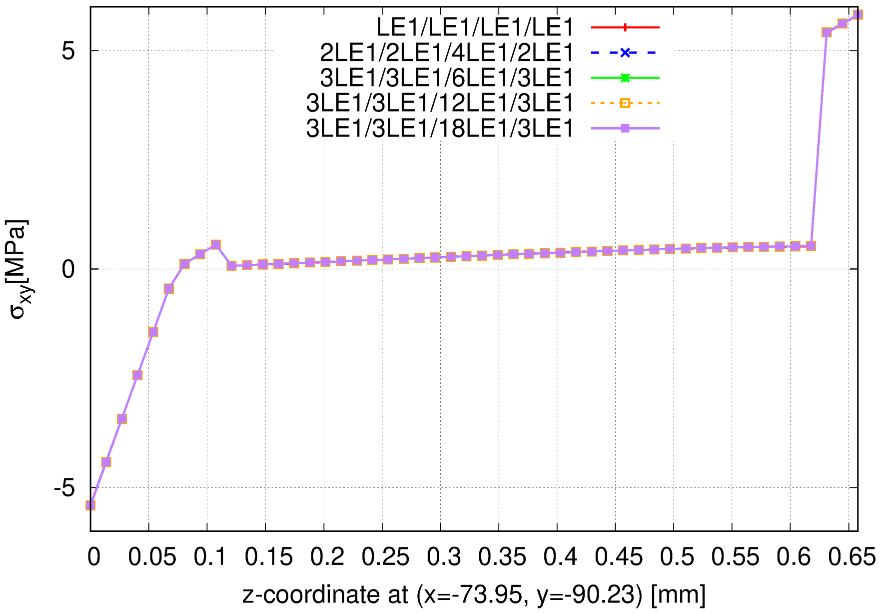

Figure 6.37: Effect of through-the-thickness mesh refinement on the σ_{xy} stress profile.

that this zone is relatively unloaded compared to the surrounding layers. The shear component σ_{xy} reaches its maximum values at the outer surfaces (z=0 and z=0.658mm) and becomes nearly zero in the central region, where the system appears to be in a state of near-pure in-plane stress equilibrium.

Table 6.39: Interlayer stress convergence results along the plate thickness at $(x, y) = (-73.95, -90.23)$ mm: Second-Order Lagrange expansion

z-coordinate [mm]	σ_{xx}	σ_{yy}	σ_{zz}	σ_{xy}
0.000	-0.25	0	0	-5.2
0.080	0	-25.0	-25.0	0.4
0.115	-0.35	-4.0	-5.0	0.2
0.623	0	22.0	27.0	5.5
0.658	-0.4	25.0	30.0	6.0

The model developed using LE 2 elements for each layer exhibits a symmetric trend in the σ_{xx} distribution within the Duroid layer compared to the other models. This behavior can be attributed to the presence of only quadratic terms in the mathematical formulation of the expansion. Aside from this discrepancy, the same considerations apply to the models based on second- and third-order Lagrange expansions. Since the results are essentially overlapping, it can be concluded that a single LE 1 element per layer is sufficient to capture the

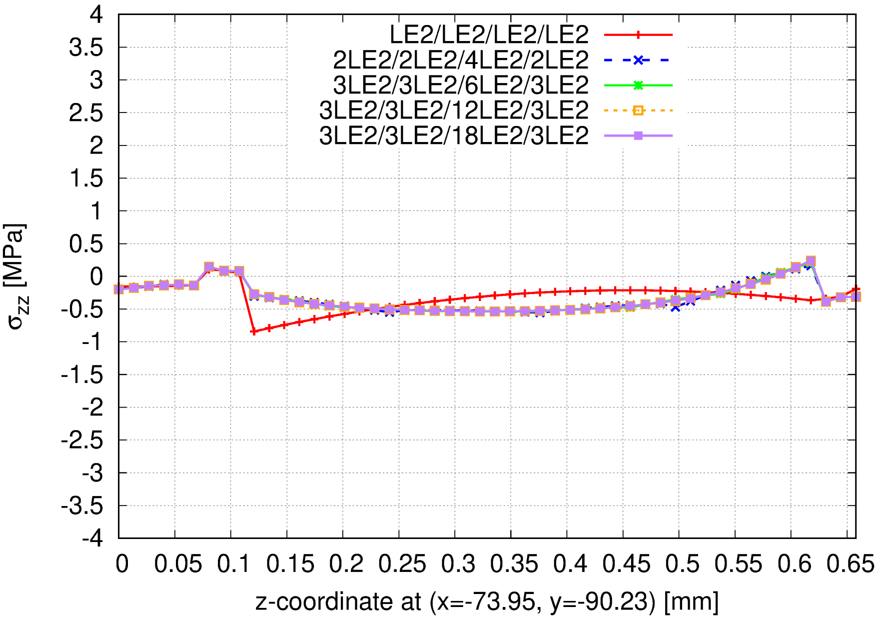

Figure 6.38: Effect of through-the-thickness mesh refinement on the σ_{zz} stress profile. It is shown the comparison between the solution obtained with baseline mesh ($LE2/LE2/LE2/LE2$) and the refined configurations (up to $3LE2/3LE2/18LE2/3LE2$)

through-the-thickness stress distribution.

Table 6.40: Interlayer stress convergence results along the plate thickness at $(x, y) = (-73.95, -90.23)$ mm: Third-Order Lagrange expansion

z-coordinate [mm]	σ_{xx}	σ_{yy}	σ_{zz}	σ_{xy}
0.000	-0.3	0	0	-5.2
0.080	0	-25.0	-25.0	0.4
0.115	-0.35	-4.0	-5.0	0.2
0.623	0.15	22.0	27.0	5.5
0.658	-0.4	24.0	30.0	6.0

Patch 2

For this patch, the same analysis was carried out by considering a node approximately symmetric to that of the left patch. Due to the boundary conditions not being applied exactly at the center of the plate, and the asymmetric distribution of the patches, this comparison was performed to verify whether similarly located patches in the most deformed regions exhibit comparable stress distributions. This section reports a subset of the results obtained for

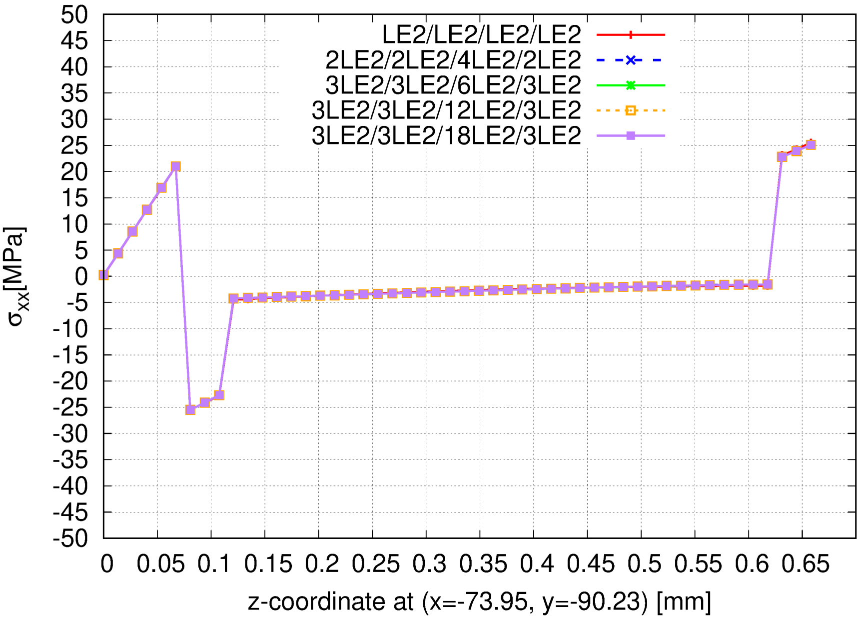

Figure 6.39: Effect of through-the-thickness mesh refinement on the σ_{xx} stress profile.

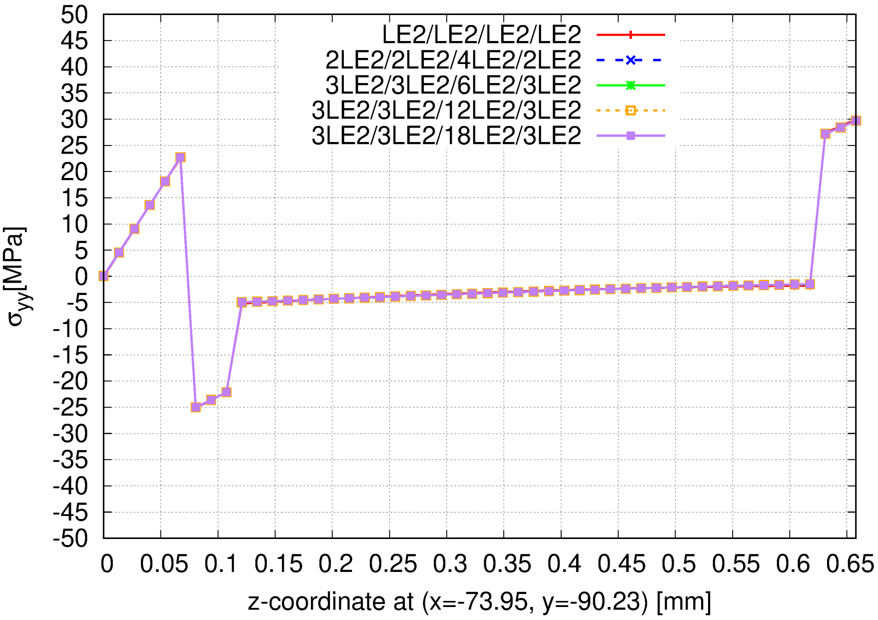

Figure 6.40: Effect of through-the-thickness mesh refinement on the σ_{yy} stress profile.

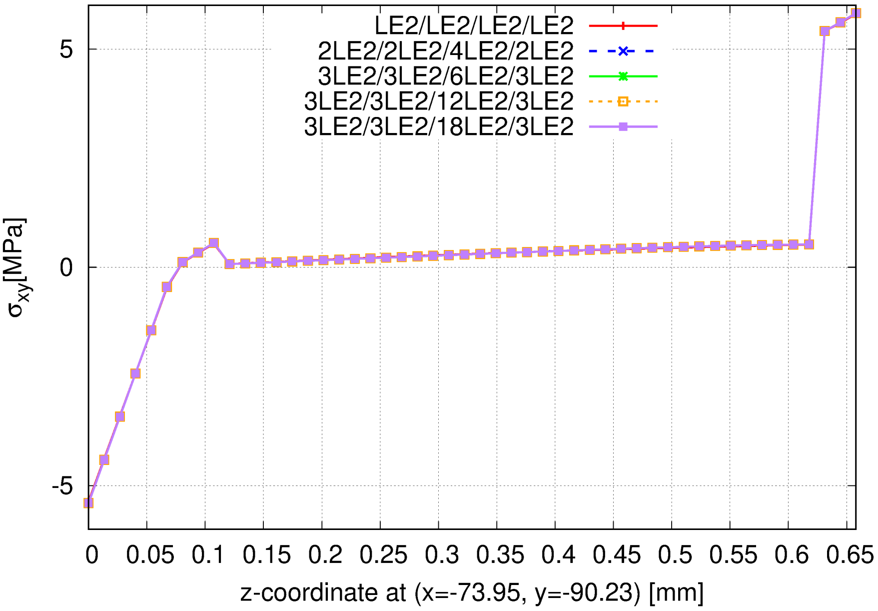

Figure 6.41: Effect of through-the-thickness mesh refinement on the σ_{xy} stress profile.

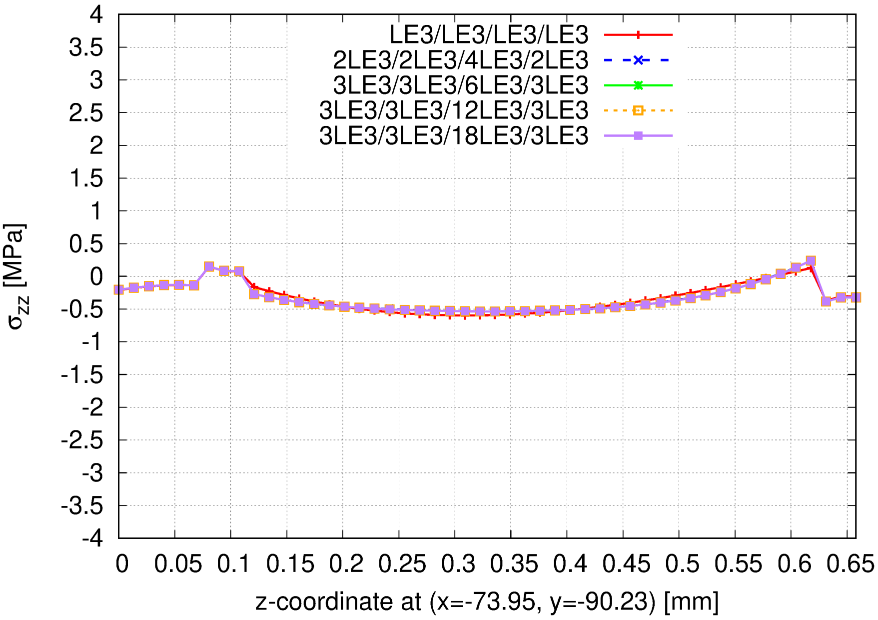

Figure 6.42: Effect of through-the-thickness mesh refinement on the σ_{zz} stress profile. It is shown the comparison between the solution obtained with baseline mesh ($LE3/LE3/LE3/LE3$) and the refined configurations (up to $3LE3/3LE3/18LE3/3LE3$).

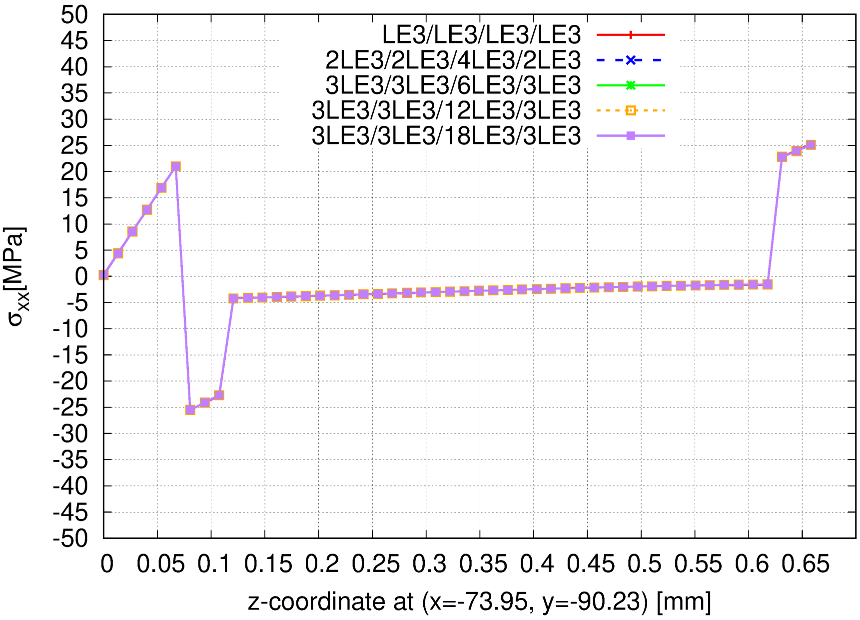

Figure 6.43: Effect of through-the-thickness mesh refinement on the σ_{xx} stress profile.

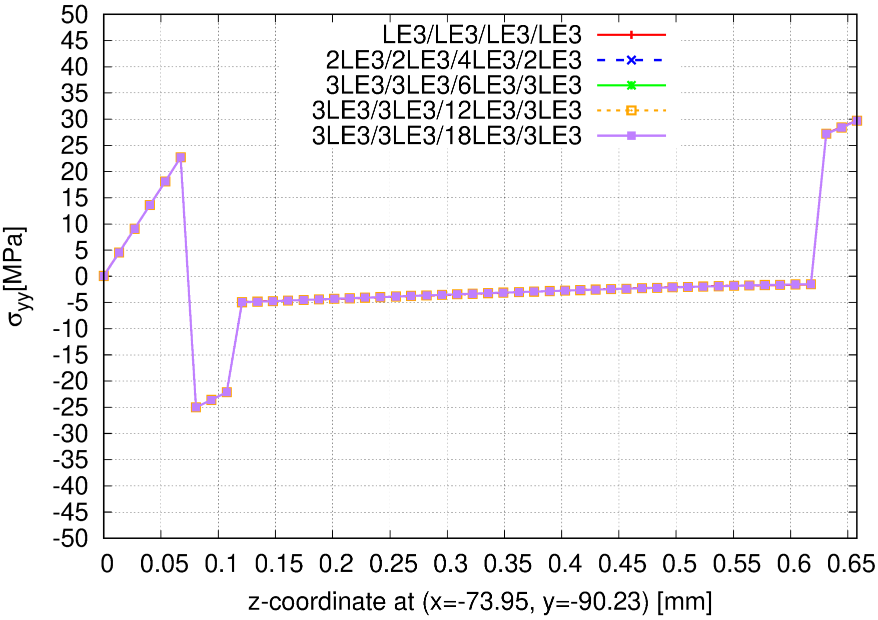

Figure 6.44: Effect of through-the-thickness mesh refinement on the σ_{yy} stress profile.

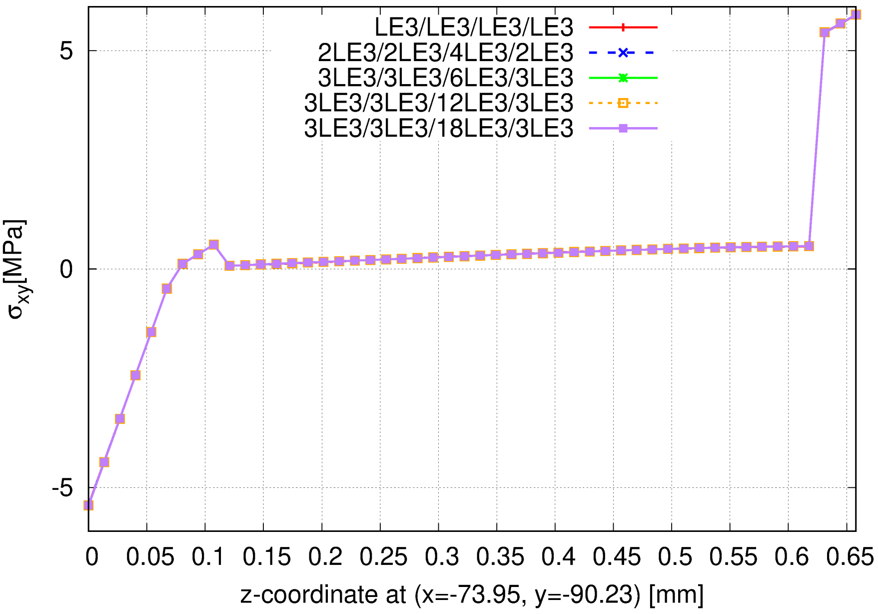

Figure 6.45: Effect of through-the-thickness mesh refinement on the σ_{xy} stress profile.

Patch 2, specifically those related to models based on first-order Lagrange expansions. The complete set of results is provided in the Appendix A. The accuracy of the results, using σ_{zz} as the reference parameter, is confirmed even for models with a low number of elements and low-order expansions.

Table 6.41: Interlayer stress convergence results along the plate thickness at $(x, y) = (78.62, -91.67)$ mm: First-Order Lagrange expansion

z-coordinate [mm]	σ_{zz}	σ_{xx}	σ_{yy}	σ_{xy}
0.000	-0.3	0	0	4.5
0.080	0	-25.0	-25.0	-0.2
0.115	-0.3	-4.0	-5.0	-0.4
0.623	0.2	-22.0	26.0	-4.5
0.658	-0.4	24.0	29.0	-4.8

Particular attention is given to the σ_{xy} component. As observed for Patch 1, it exhibits pronounced peaks at the upper and lower surfaces. Since the out-of-plane displacement w of the two patches is nearly symmetric with respect to the yz plane passing through the center of the plate, the σ_{xy} distribution is expected to be antisymmetric, as it depends on the mixed derivatives of the

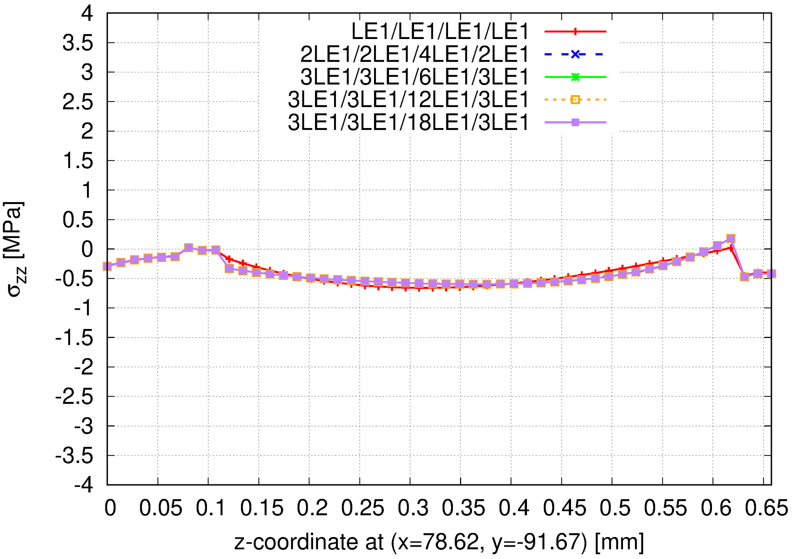

Figure 6.46: Effect of through-the-thickness mesh refinement on the σ_{zz} stress profile. It is shown the comparison between the solution obtained with baseline mesh ($LE1/LE1/LE1/LE1$) and the refined configurations (up to $3LE1/3LE1/18LE1/3LE1$)

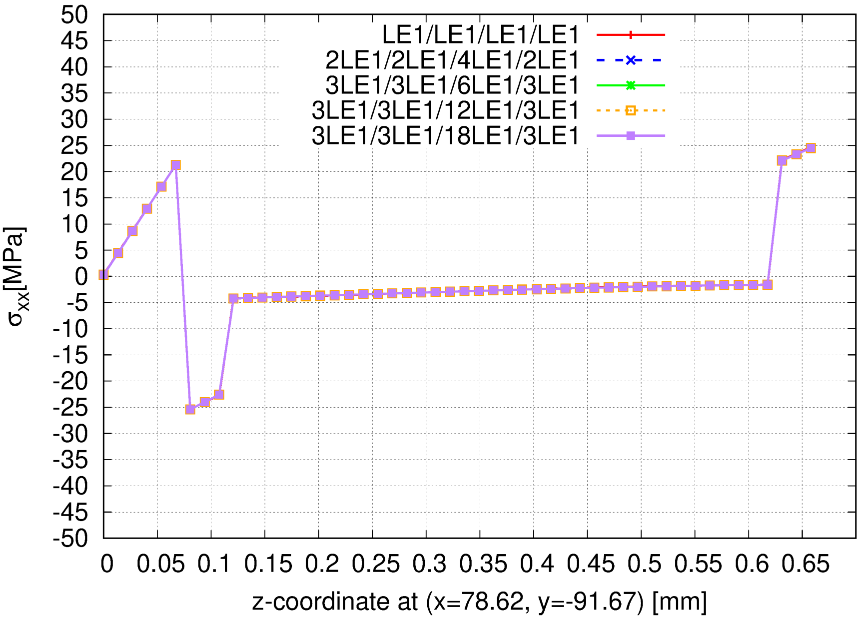

Figure 6.47: Effect of through-the-thickness mesh refinement on the σ_{xx} stress profile.

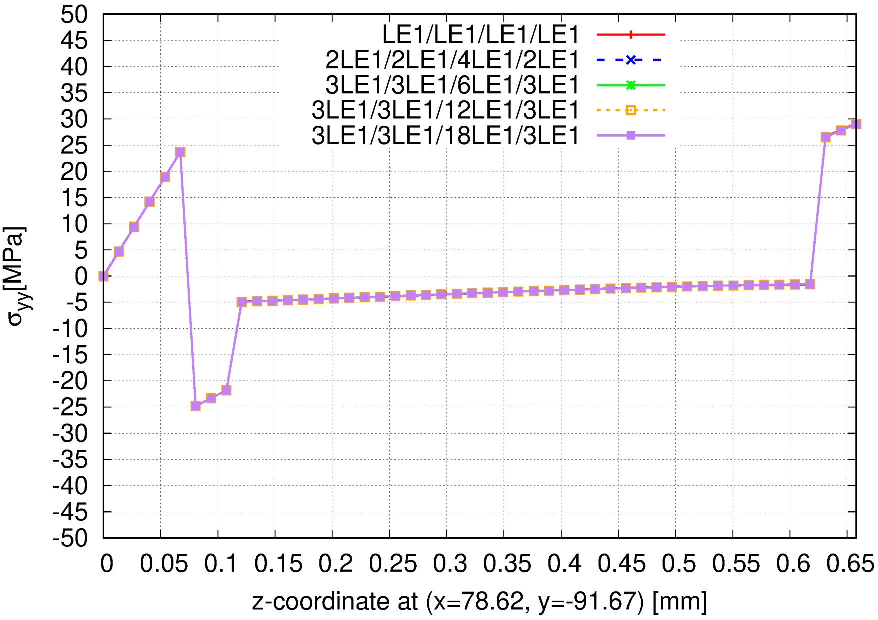

Figure 6.48: Effect of through-the-thickness mesh refinement on the σ_{yy} stress profile.

displacement field.

$$\sigma_{xy} \propto \frac{\partial^2 w}{\partial x \partial y} \tag{6.2}$$

Within the dielectric layer, σ_{xy} remains very low. The abrupt variations observed near the outer regions ($z < 0.1$ mm and$z > 0.6$ mm) are associated with layer transitions and proximity to the free edge.

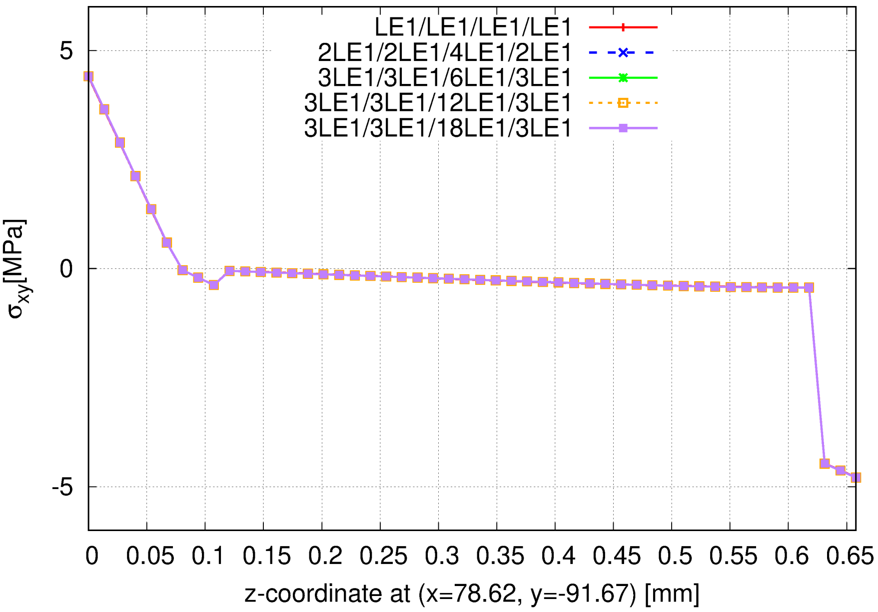

Figure 6.49: Effect of through-the-thickness mesh refinement on the σ_{xy} stress profile.

Chapter 7

Macroscale sub-array model

This chapter presents the development and results obtained from the most complex sub-array model, whose features closely approximate those of the original configuaration.

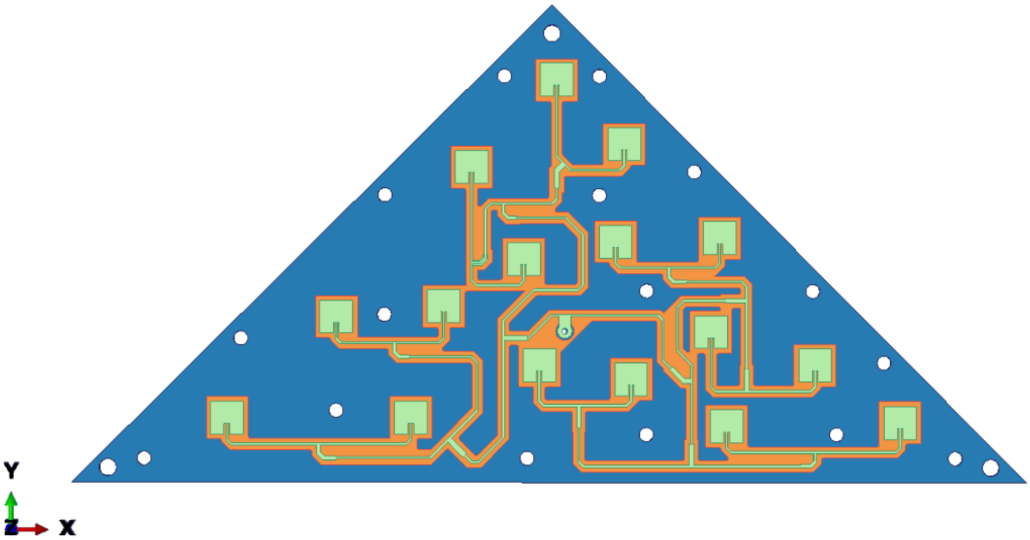

Figure 7.1: Original sub-array ABAQUS model illustrating the layered configuration of CFRP (blue), copper foil layer (not visible in orange), RT/Duroid 5880 layer (green) and copper patches with microstrip lines (orange)

The original sub-array model features a highly complex geometry. The triangular plate includes several holes for assembly. The CFRP layer is followed by the substrate, consisting of a thin copper foil and an RT/Duroid dielectric layer, characterized in this case by multiple fillets. Finally, the top layer includes patches and microstrip lines, where a significant reduction in volume and cross-sectional area is observed. Some detailed features included in the original sub-array model, such as holes, fillets and the connections between lines and patche, are simplified and therefore neglected in the final model.

The relevance of this model lies in the presence of microstrip lines and the significant cross-sectional variations between the layers, which influence the structural response under thermal loading. The effect of the microstrips alone on the out-of plane displacements is also briefly highlighted.

7.1 Development of the final model

7.1.1 Abaqus 3D shell model

Table 7.1: ABAQUS model mesh characteristics

Total # of nodes	Total # of elements
68785	21151

The ABAQUS model was developed using three distinct 3D planar shell sections:

- a shell section representing the CFRP laminate;
- a shell section representing the combined copper foil
- a RT/Duroid 5880 dielectric substrate, modeled with a composite layup and serving as support for both radiating patches and the microstrips;
- a shell section corresponding to the radiating copper patches.

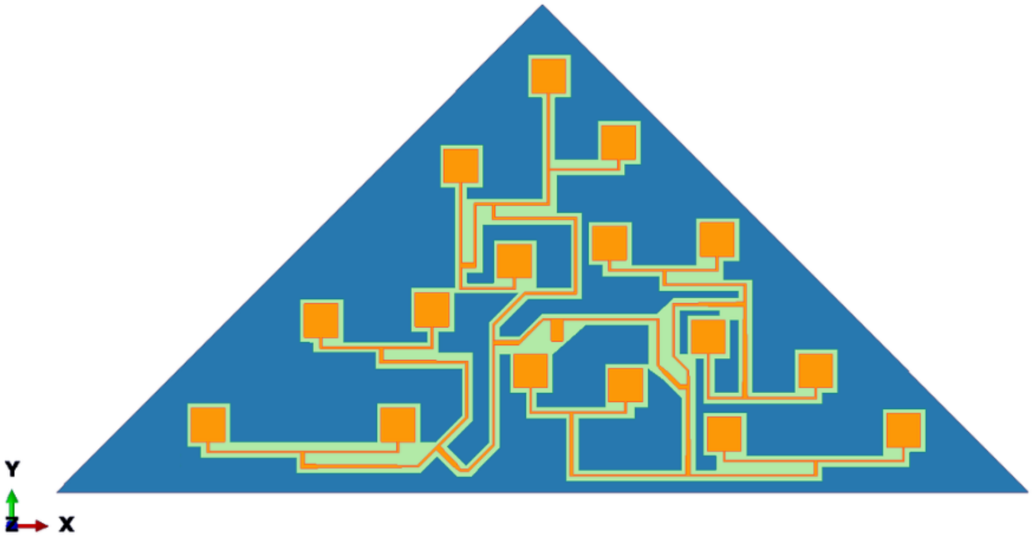

Figure 7.2: Final sub-array ABAQUS model illustrating the layered configuration of CFRP (blue), copper foil layer (not visible in orange), RT/Duroid 5880 layer (green) and copper patches with microstrip lines (orange)

Each layer was discretized using quadratic quadrilateral reduced-integration shell elements (S8R). A refined in-plane mesh was adopted for all layers to ensure adequate resolution of the displacement field. It was necessary to employ elements with sizes ranging from 0.8 mm to 1 mm in order to obtain a sufficiently refined mesh and prevent shear locking effects during the analysis. The use of quadratic elements is motivated by the need to accurately capture the mechanical response of a geometrically thin multilayered structure, where bending-membrane coupling effects may be non-negligible.

Table 7.2: Detailed nodal and elemental distribution across different shell layers.

	CFRP fabric	**Copper foil**	**RT/Duroid 5880**	**Patches and microstrip line**
Number of nodes	36582	12451	12451	7301
Number of elements	12033	3654	3654	1810

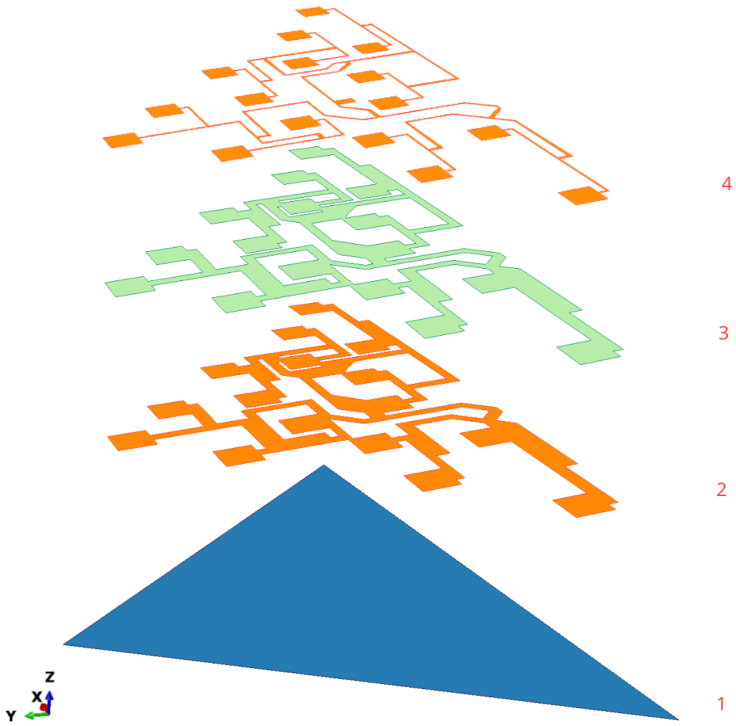

Figure 7.3: Exploded view of the subarray assembly. The components include the CFRP plate (blue), the copper (Cu) foil (orange), and the RT/Duroid 5880 substrate (green)

7.1.2 CUF model

A Carrera Unified Formulation (CUF) model is subsequently developed for comparison purposes. Three through-the-thickness expansions configurations are considered:

- CFRP laminate expansion;
- CFRP+Cu foil+RT/Duroid 5880 expansion;
- CFRP+CU foilRT/Duroid 5880 + Cu patches expansion.

The CUF framework allows an enriched kinematic description along the thickness direction through hierarchical expansions of the displacement field. Owing to this refined through-thickness representation, a coarser in-plane mesh can be employed without compromising accuracy. The geometric complexity of the model led to the use of Q9 elements with varying sizes, significantly refined in correspondence with the microstrip lines and at their junctions with the patches. Wherever possible, the mesh was kept as regular as possible to ensure improved accuracy of the results.

Table 7.3: CUF model in-plane mesh characteristics

Total number of nodes	**Total number of elements**
10741	2652

Nevertheless, local in-plane mesh refinement was introduced in correspondence with the two lateral patches. This refinement was implemented to enable detailed evaluation of the through-the-thickness stress components in those regions, while avoiding the need for separate submodel. Both Layer Wise and Equivalent Single Layer formulations were implemented using the same in-plane discretization to ensure consistency in the comparative assessment. For the definition of appropriate boundary conditions, shown in Figure 7.4, a MATLAB code was used to identify the nodes of the CUF in-plane mesh closest to those selected in the ABAQUS model. Both displacements and rotations along the three reference axes were constrained through the thickness at the two nodes identified by the MATLAB code. Finally, a thermal load of $\Delta\theta = 100$ K is applied. The layers thickness are reported in Table 6.1, while materials' properties are reported in Table 6.2, Table 6.3 and Table 6.4.

7.2 Thermo-elastic analysis results

In this section, the results obtained from an uncoupled thermo-elastic analysis, corresponding to Procedure 199, are presented.

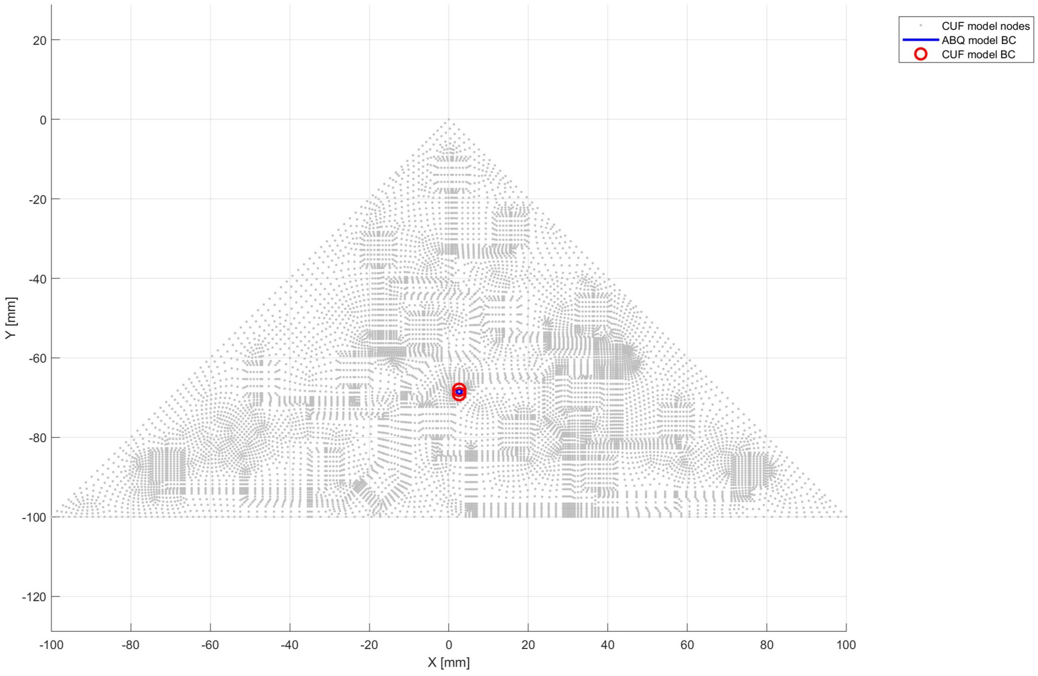

Figure 7.4: Boundary conditions of CUF model

7.2.1 Macroscopic thermo-elastic deformation

As observed in the previous cases, a slight asymmetry in the out-of-plane displacement field wwith respect to the yzplane is consistently detected. This is due to the slightly off-centered boundary condition and the non-uniform distribution of the patches on the plate surface. Another common aspect, compared to the sub-array model without lines presented in the previous chapter, is that the presence of microstrip lines reduces the maximum deformation of the plate by a few millimeters. The following Table 7.4 reports the percentage difference at the point of maximum displacement, located at (x,y)=(100,-100). A similar trend is observed in the corresponding CUF models.

Table 7.4: Comparison of Abaqus displacement results with and without lines.

|Max displ. w| at (-100, -100) [mm] ABQ no lines	**|Max displ. w| at (-100, -100) [mm] ABQ with lines**	**|% Difference| w.r.t. ABQ no lines**
38.49	34.37	10.70

Starting from an in-plane mesh of 2652 Q9 elements, both Layer-Wise (LW) and Equivalent Single Layer (ESL) CUF models were generated. Compared to the simplified models, a larger percentage difference between CUF and ABAQUS

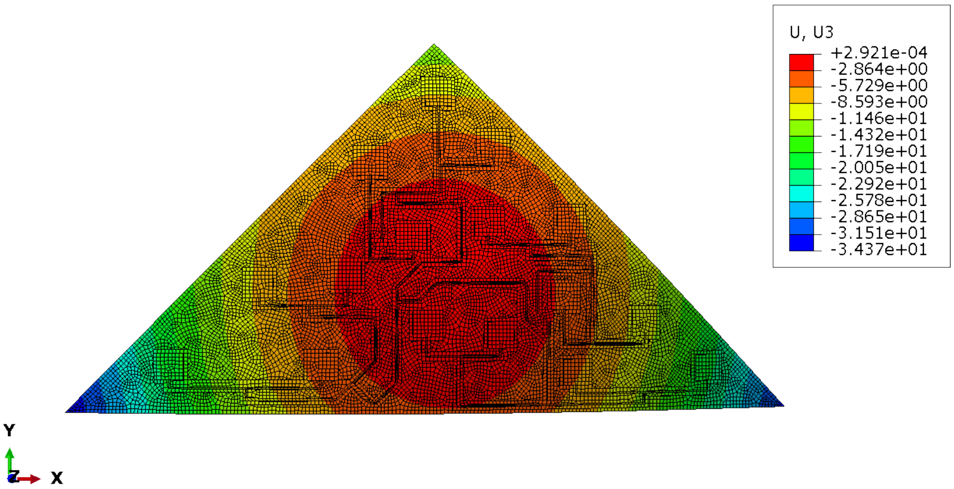

Figure 7.5: ABAQUS model results

results is observed. This is mainly due to the presence of microstrip lines, which, owing to their small volume and shell-like geometry, introduce mesh distortion and a more complex coupling between layers, particularly in the ABAQUS model. As the ABAQUS mesh is further refined, the results progressively approach those of the CUF model, which can therefore be considered both more accurate and computationally efficient.

Table 7.5: Abaqus reference values for out-of-plane displacement w at (x,y)=(-100,-100) and (x,y)=(100,-100).

|Displacement w| at (-100, -100) [mm]	|Displacement w| at (100, -100) [mm]
34.37	32.61

Table 7.6: Convergence analysis of out-of-plane displacement w for Taylor Expansion (TE) models.

Expansion Order	DOF	|Displacement w| at (-100, -100) [mm]	|%Difference| w.r.t. ABQ	|Displacement w| at (100, -100) [mm]	|%Difference| w.r.t. ABQ
TE 1	64446	4.20E+01	22.2	3.92E+01	20.3
TE 2	96669	3.31E+01	3.58	3.10E+01	4.85
TE 3	128892	3.37E+01	1.88	3.16E+01	3.12
TE 5	193338	3.37E+01	1.88	3.16E+01	3.12

For the ESL models, a full agreement is observed between the TE 3 (128892 DOF) and TE 5 (193338 DOF) solutions, indicating that convergence has been achieved. In comparison with ABAQUS results, the differences remain limited; however, despite all being ESL formulations, the CUF models require significantly fewer degrees of freedom—approximately one-third or less than half of those of the ABAQUS model (412710 DOF).

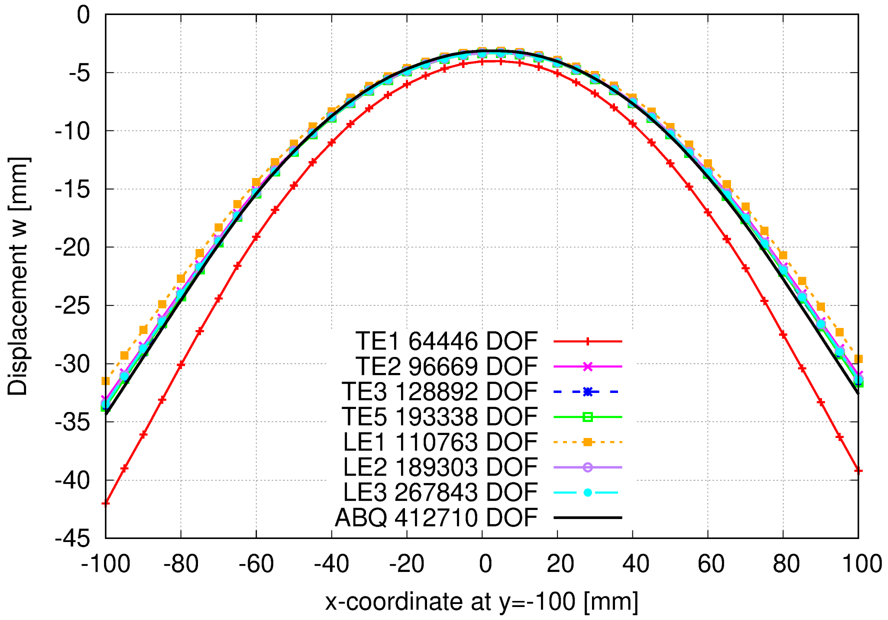

Figure 7.6: Out-of-plane displacement: comparison between TE expansions, LE expansions and ABAQUS model results with respective DOF

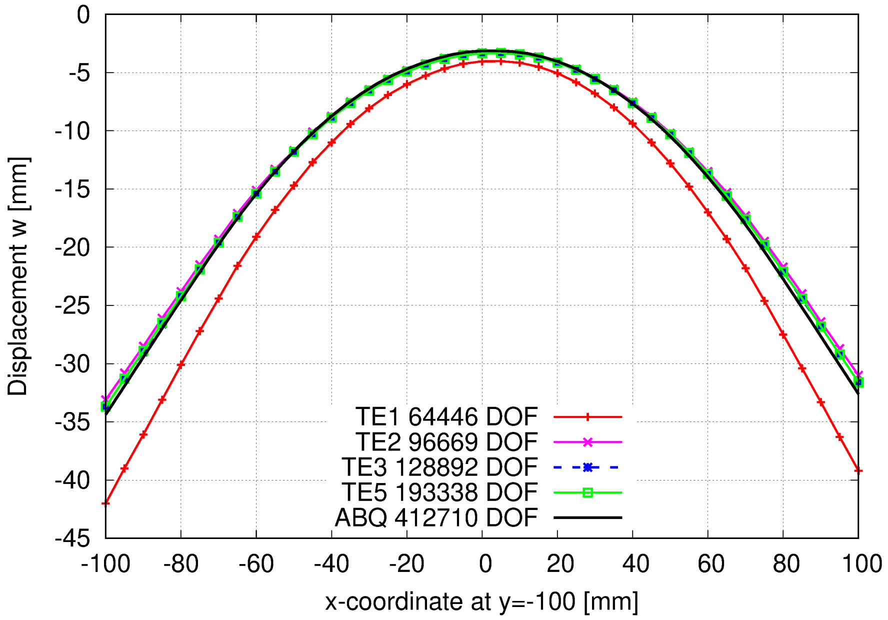

Figure 7.7: Out-of-plane displacement: comparison between TE expansions models and ABAQUS model results with respective DOF

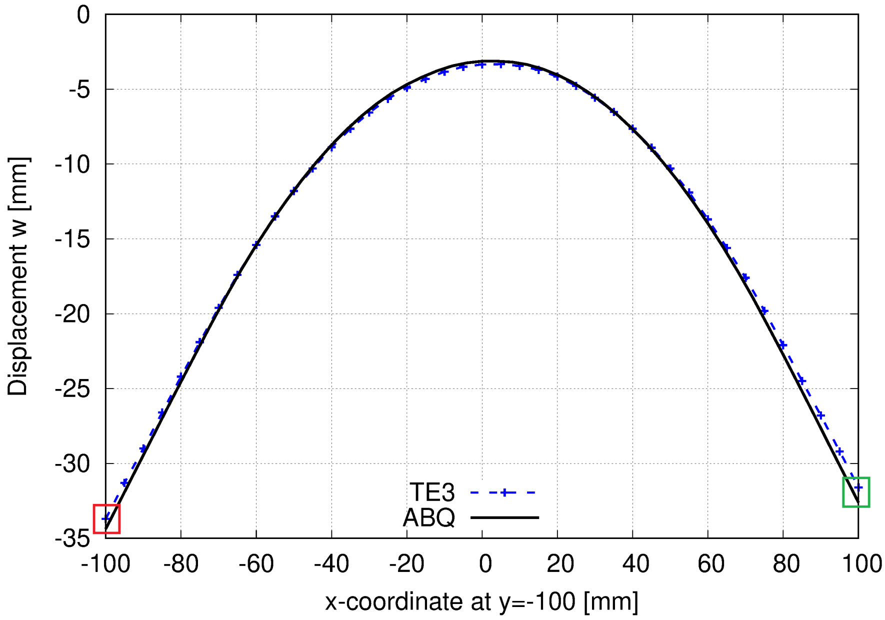

Figure 7.8: Out-of-plane displacement: comparison between Third-Order Taylor expansions model and ABAQUS model results

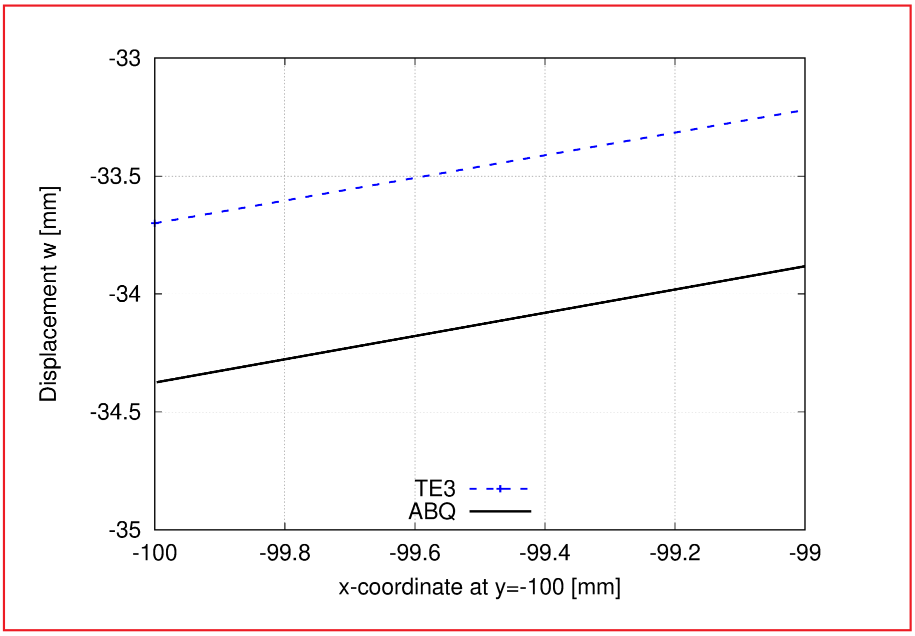

(a)

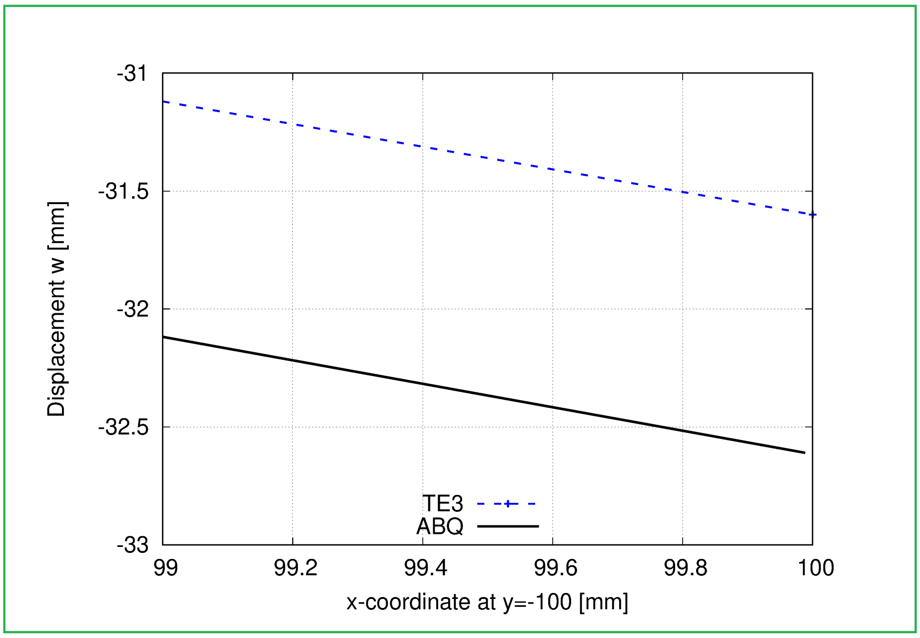

(b)

Figure 7.9: Displacement detail for the Third-Order Taylor expansions model: (a) at (-100,-100); (b) at (100,-100)

Regarding the LW models, overlapping results are obtained for the second-order (189303 DOF) and third-order (267843 DOF) Lagrange expansions, again highlighting a substantial reduction in computational cost. In particular, both CUF LE 2 and LE 3 models are fully Layer-Wise and allow direct evaluation of through-the-thickness stresses. In contrast, in ABAQUS, such stress resolution would require a 3D solid model, leading to higher computational cost and potential shear-locking issues due to the small thicknesses and geometric complexity of the layers.

Table 7.7: Convergence analysis of out-of-plane displacement w for Lagrange Expansion (LE) models.

Expansion Order	**DOF**	**|Displacement w| at (-100, -100) [mm]**	**|%Difference| w.r.t. ABQ**	**|Displacement w| at (100, -100) [mm]**	**|%Difference| w.r.t. ABQ**
LE 1	110763	3.15E+01	8.27	2.96E+01	9.34
LE 2	189303	3.34E+01	2.80	3.13E+01	4.01
LE 3	267843	3.35E+01	2.61	3.14E+01	3.84

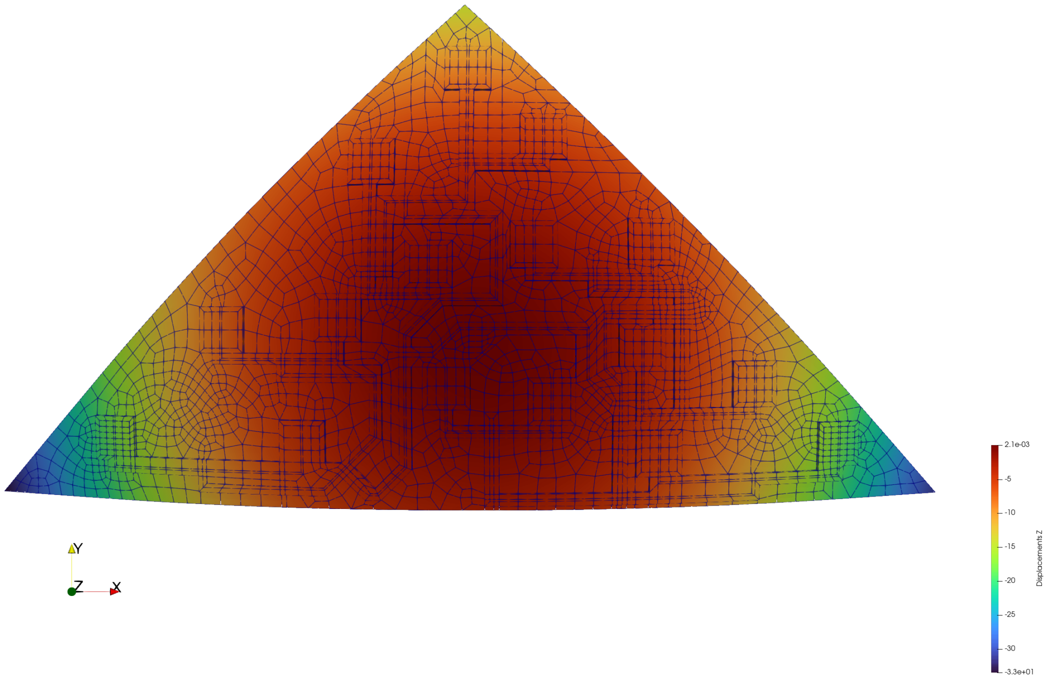

Figure 7.10: CUF out-of-plane displacement under thermal load of 100 K using Lagrange Expansions of the third order

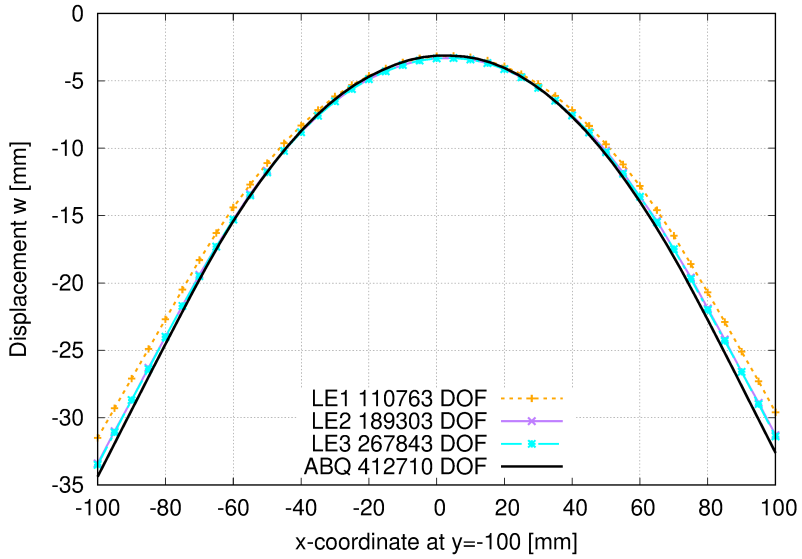

Figure 7.11: Out-of-plane displacement: comparison between LE expansions models and ABAQUS model results with respective DOF

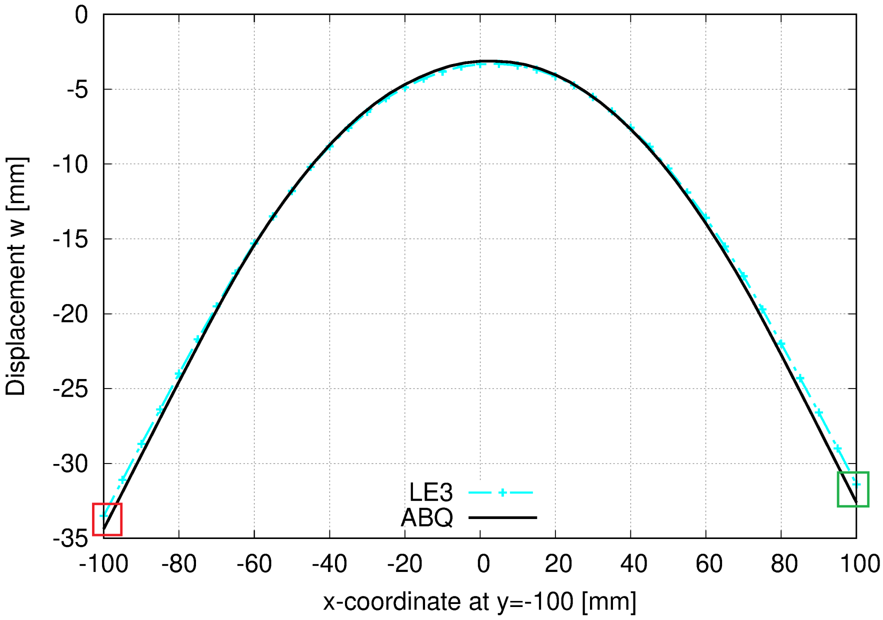

Figure 7.12: Out-of-plane displacement: comparison between Third-Order Lagrange expansions model and ABAQUS model results

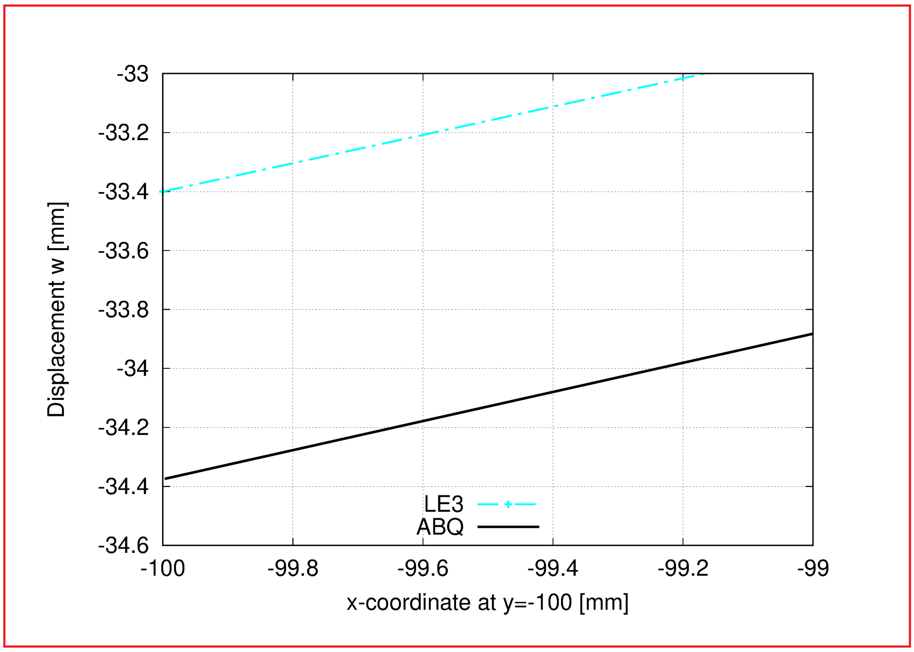

(a)

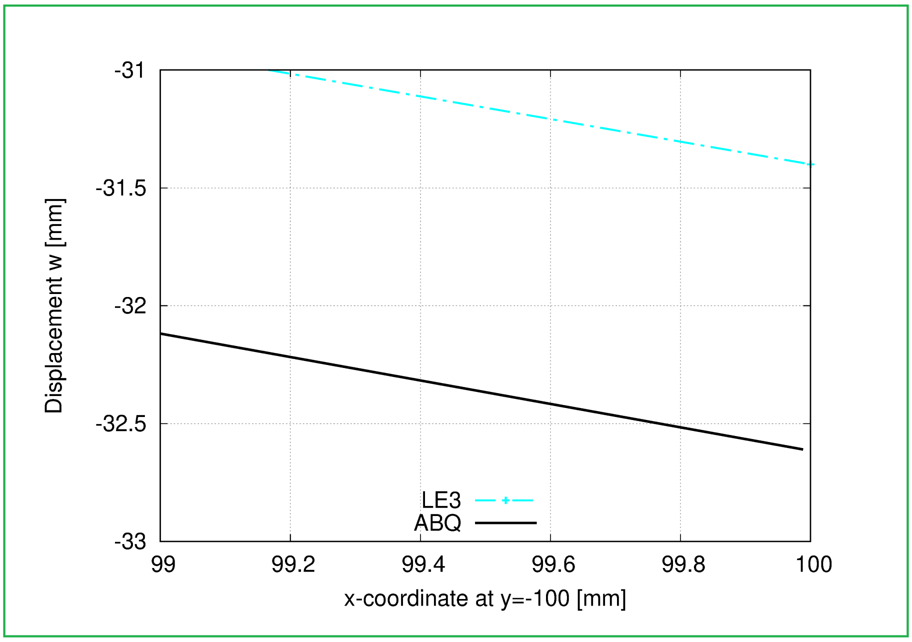

(b)

Figure 7.13: Displacement detail for LE 3 model: (a) at (-100,-100); (b) at (100,-100)

7.2.2 Through-the-thickness stress distributions

In this section, the results of the through-the-thickness stress analysis near the free edge of two selected patches are reported. The patches, together with their corresponding nodes, are identified in the regions undergoing the highest deformation and stress levels.To accurately capture free-edge effects, a refined discretization along the thickness direction is necessary. Theσ_{zz} stress component is taken as a reference parameter to evaluate the suitability of the mesh, since it is expected to be approximately zero.

The following Figure 7.14 and Figure 7.15 show the selected patches and the corresponding nodes considered in the analysis.

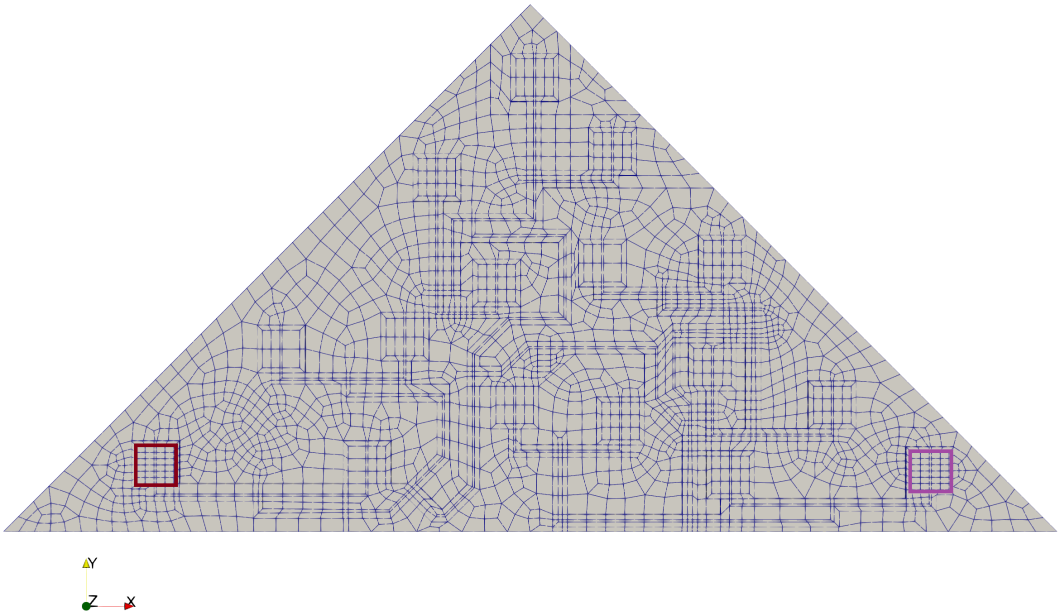

Figure 7.14: CUF model showing the analysed patches: "Patch 1" is highlighted in red, "Patch 2" is highlighted in purple

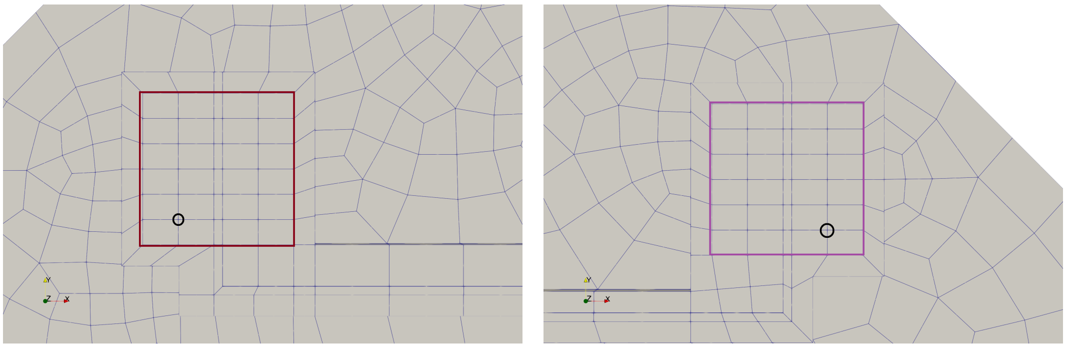

(a) (b)

Figure 7.15: (a) "Patch 1" and evaluated node (x,y)=(-73.71, -90.22) mm; (b) "Patch 2" and evaluated node (x,y)=(78.37, -91.36) mm

Patch 1

As in the case without microstrip lines, Layer-Wise models based on first-, second-, and third-order Lagrange expansions (LE1, LE2, LE3) were developed, progressively increasing the number of elements through the thickness depending on the layer thickness. The σ_{zz} component was continuously monitored to assess the reliability of the results. Models based on first-order Lagrange expansions exhibit some instability in capturing σ_{zz}, as evidenced by the peaks observed within the CFRP layer ($0 < z < 0.08$ mm). Increasing the number of elements reduces the amplitude of these peaks. More consistent results are obtained

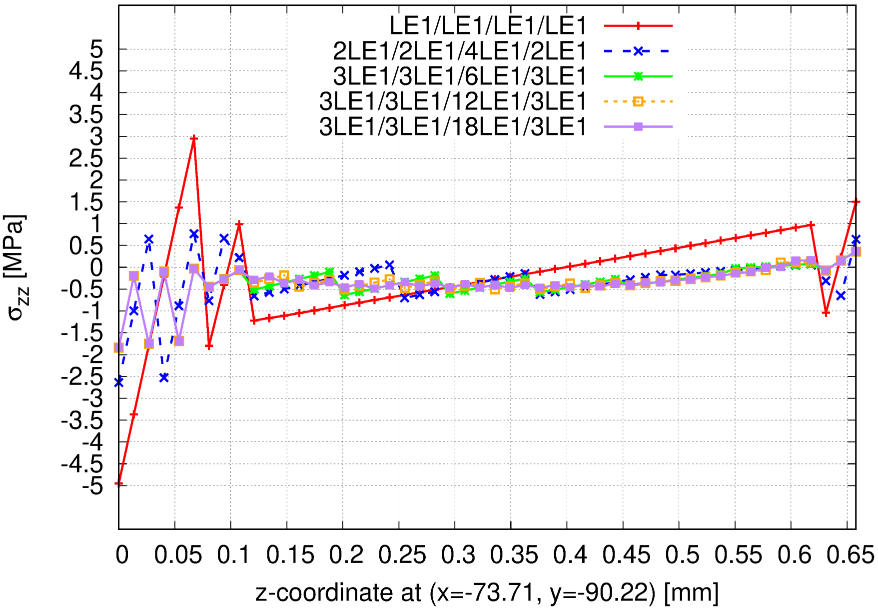

Figure 7.16: Effect of through-the-thickness mesh refinement on the σ_{zz} stress profile. The comparison between the baseline mesh ($LE1/LE1/LE1/LE1$) and the refined configurations (up to $3LE1/3LE1/18LE1/3LE1$) shows that the stress gradients are consistently captured, indicating a converged numerical solution

using second- and third-order expansions. In particular, for a uniform element distribution (LE2/LE2/LE2/LE2), a symmetric trend in σ_{zz} is observed with respect to the other results, due to the quadratic nature of the expansion, which may limit the accuracy in stress reconstruction.

Table 7.8: Interlayer stress convergence results along the plate thickness at $(x, y) = (-73.71, 90.22)$ mm: First-Order Lagrange expansion

z-coordinate [mm]	σ_{zz} [MPa]	σ_{xx} [MPa]	σ_{yy} [MPa]	σ_{xy} [MPa]
0	-0.2	0	0	-5.3
0.08	0.1	-25.5	-25.1	0.4
0.115	-0.3	-4.2	-5	0.1
0.623	0.1	22.8	27.2	5.5
0.658	-0.3	25.2	30	6.1

The stress peaks observed in σ_{xx}, σ_{yy}, and σ_{xy} follow trends similar to those identified in the model without microstrip lines, although with slightly different

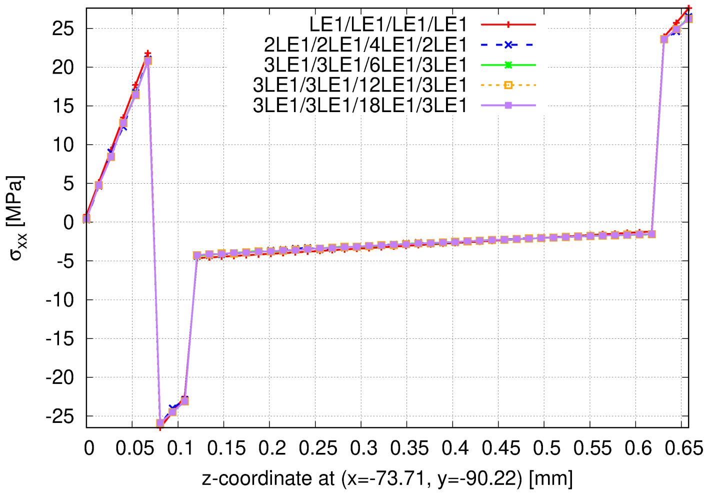

Figure 7.17: Effect of through-the-thickness mesh refinement on the σ_{xx} stress profile.

magnitudes, highlighting the influence of the interconnecting circuits. In this model, the in-plane mesh of the patches is slightly less refined than in the previous case; however, this does not appear to significantly affect the accuracy of the results.

Table 7.9: Interlayer stress convergence results along the plate thickness at (x, y) = (-73.71,90.22) mm: Second-Order Lagrange expansion.

z-coordinate [mm]	σ_{zz} [MPa]	σ_{xx} [MPa]	σ_{yy} [MPa]	σ_{xy} [MPa]
0	-0.25	0	0	-5.3
0.08	0	-25.5	-25.1	0.4
0.115	-0.35	-4.2	-5	0.2
0.623	0	22.8	27.2	5.5
0.658	-0.4	25.2	30	6.1

Patch 2

As expected, similar through-the-thickness stress distributions are obtained for Patch 2, with the main discrepancy again observed in the σ_{zz} component. The σ_{xy} distributions for the two patches exhibit a specular (antisymmetric) behavior. This is consistent with the fact that the out-of-plane displacement was nearly symmetric with respect to the yzplane passing through the center of the plate, while σ_{xy}depends on the mixed second derivative of the displacement

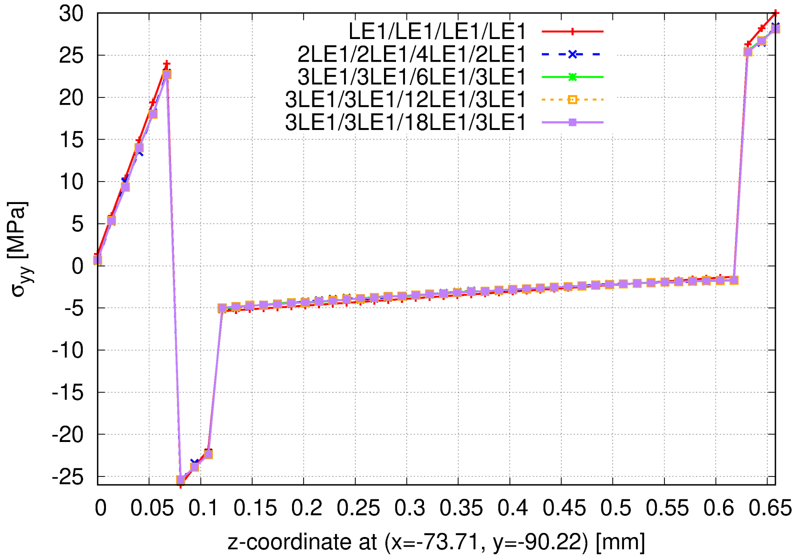

Figure 7.18: Effect of through-the-thickness mesh refinement on the σ_{yy} stress profile.

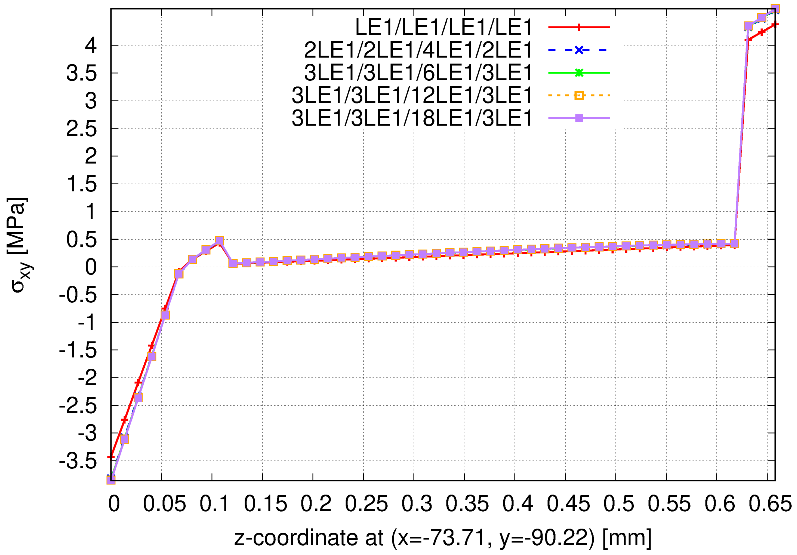

Figure 7.19: Effect of through-the-thickness mesh refinement on the σ_{xy} stress profile.

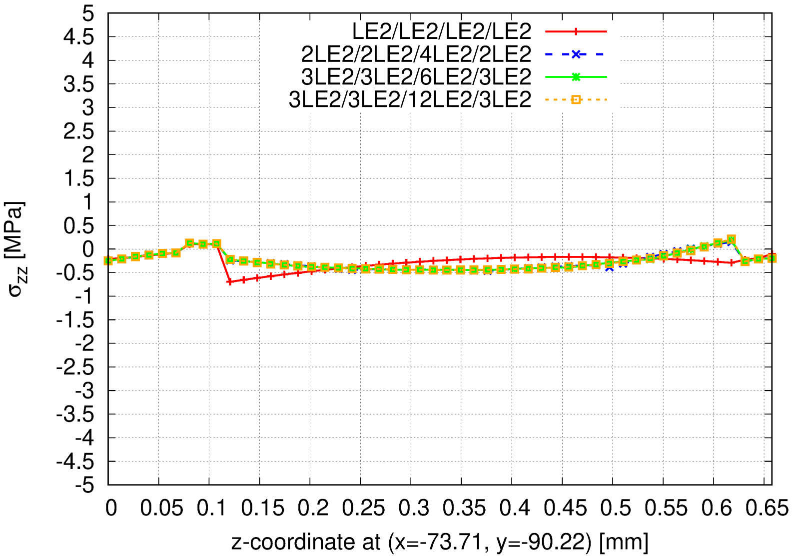

Figure 7.20: Effect of through-the-thickness mesh refinement on the σ_{zz} stress profile. The comparison between the baseline mesh ($LE2/LE2/LE2/LE2$) and the refined configurations (up to $3LE2/3LE2/12LE2/3LE2$) shows that the stress gradients are consistently captured, indicating a converged numerical solution

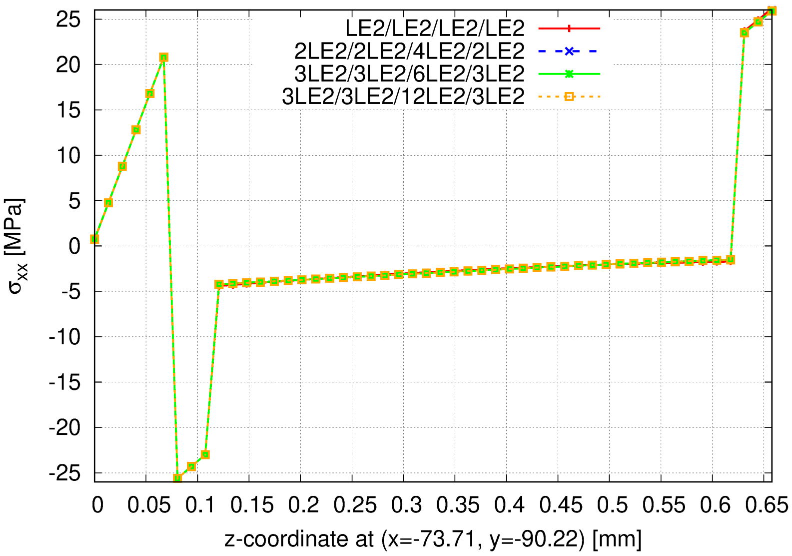

Figure 7.21: Effect of through-the-thickness mesh refinement on the σ_{xx} stress profile.

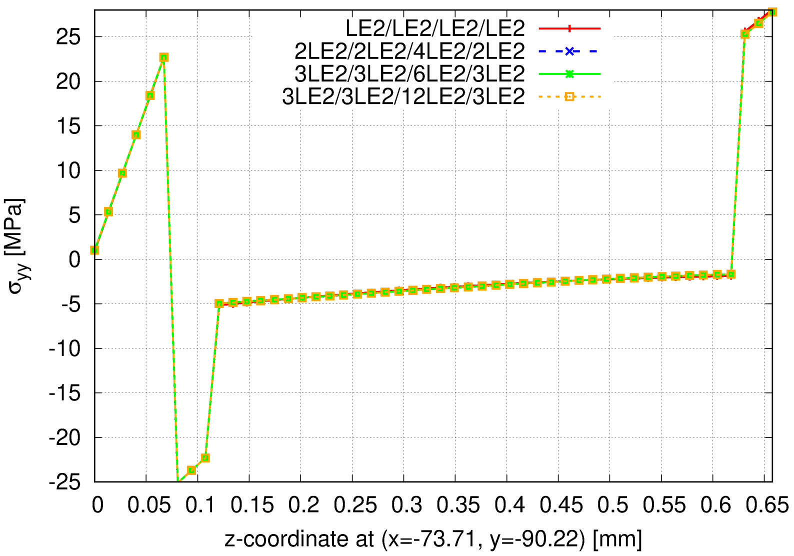

Figure 7.22: Effect of through-the-thickness mesh refinement on the σ_{yy} stress profile.

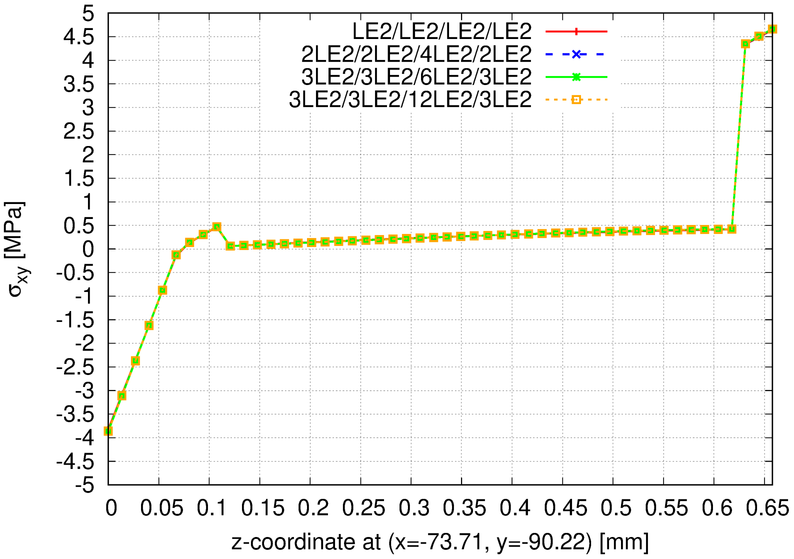

Figure 7.23: Effect of through-the-thickness mesh refinement on the σ_{xy} stress profile.

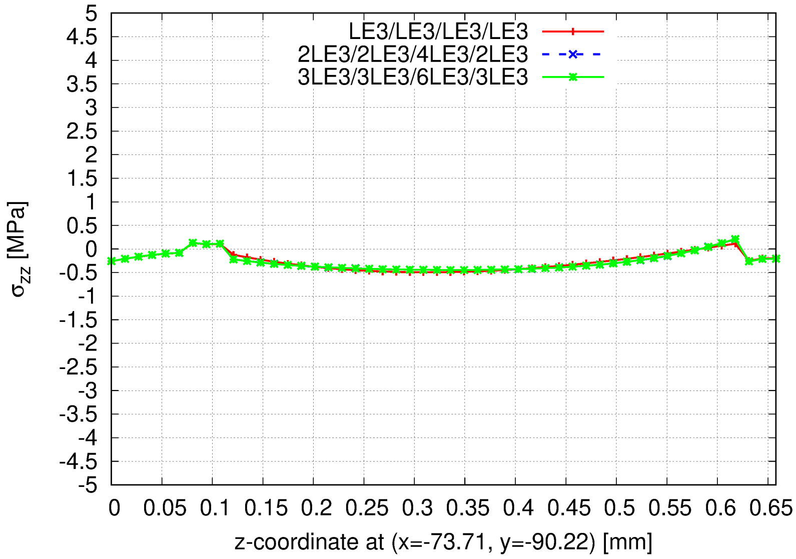

Figure 7.24: Effect of through-the-thickness mesh refinement on the σ_{zz} stress profile. The comparison between the baseline mesh ($LE3/LE3/LE3/LE3$) and the refined configurations (up to $3LE3/3LE3/6LE3/3LE3$) shows that the stress gradients are consistently captured, indicating a converged numerical solution

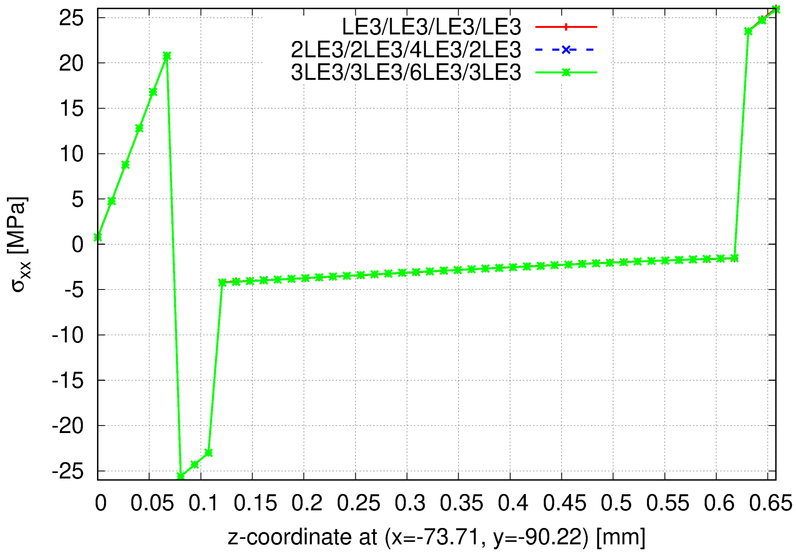

Figure 7.25: Effect of through-the-thickness mesh refinement on the σ_{xx} stress profile.

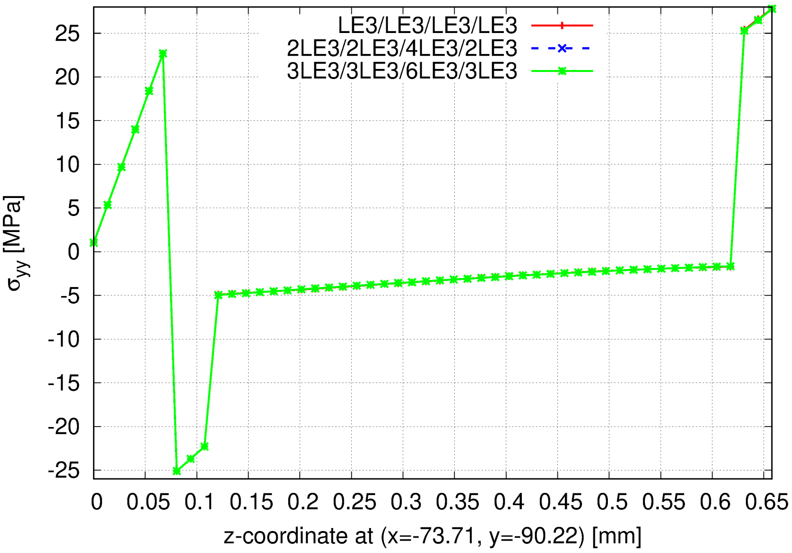

Figure 7.26: Effect of through-the-thickness mesh refinement on the σ_{yy} stress profile.

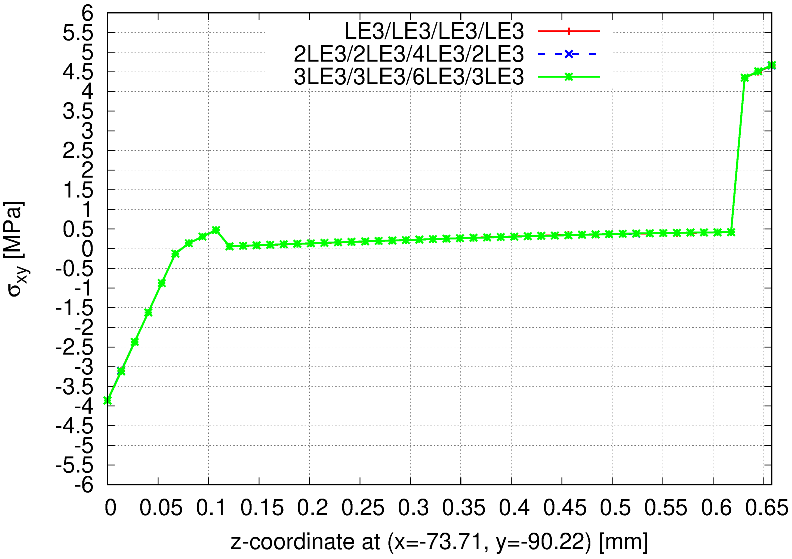

Figure 7.27: Effect of through-the-thickness mesh refinement on the σ_{xy} stress profile.

Table 7.10: Interlayer stress convergence results along the plate thickness at (x, y) = (-73.71,90.22) mm: Third-Order Lagrange expansion

z-coordinate [mm]	σ_{zz} [MPa]	σ_{xx} [MPa]	σ_{yy} [MPa]	σ_{xy} [MPa]
0	-0.3	0	0	-4.5
0.08	0	-25.2	-24.8	-0.2
0.115	-0.3	-4.1	-4.9	-0.4
0.623	0.2	22.5	26.5	-4.5
0.658	-0.4	24.5	29.2	-4.8

Table 7.11: INterlayer stress convergence results along the plate thickness ate (x,y)=(78.37,-91.36) mm: First-Order Lagrange expansion

z-coordinate	σ_{zz} **[MPa]**	σ_{xx} **[MPa]**	σ_{yy} **[MPa]**	σ_{xy} **[MPa]**
0	-0.25	0	0	4.5
0.08	0	-25.2	-24.8	-0.2
0.115	-0.35	-4.1	-4.9	-0.4
0.623	0.1	22.5	26.5	-4.5
0.658	-0.4	24.5	29.2	-4.8

field. Within the dielectric layer, σ_{xy} remains very low, while the abrupt variations observed near the outer regions ($z < 0.1$ mm and $z > 0.6$ mm) are associated with layer transitions and proximity to the free edge.

This section reports a subset of the results obtained for Patch 2, specifically those related to models based on first-order Lagrange expansions. The complete set of results is provided in Appendix B.

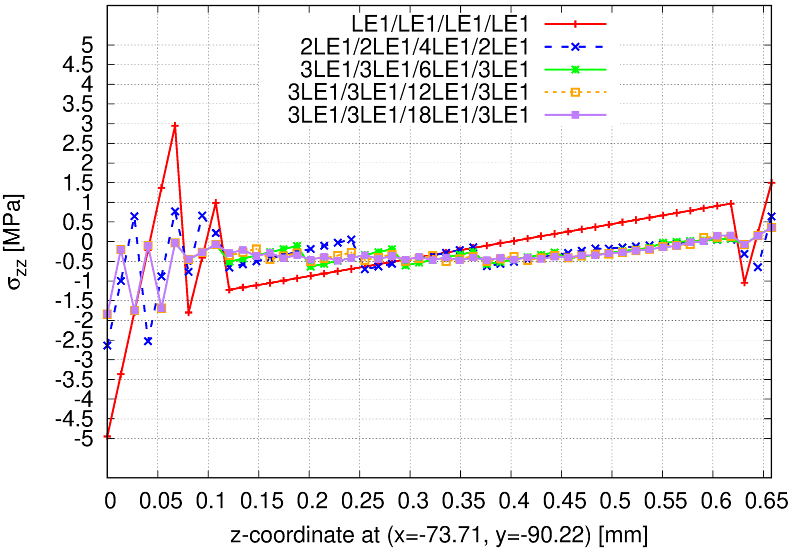

Figure 7.28: Effect of through-the-thickness mesh refinement on the σ_{zz} stress profile. The comparison between the baseline mesh ($LE1/LE1/LE1/LE1$) and the refined configurations (up to $3LE1/3LE1/18LE1/3LE1$) shows that the stress gradients are consistently captured, indicating a converged numerical solution

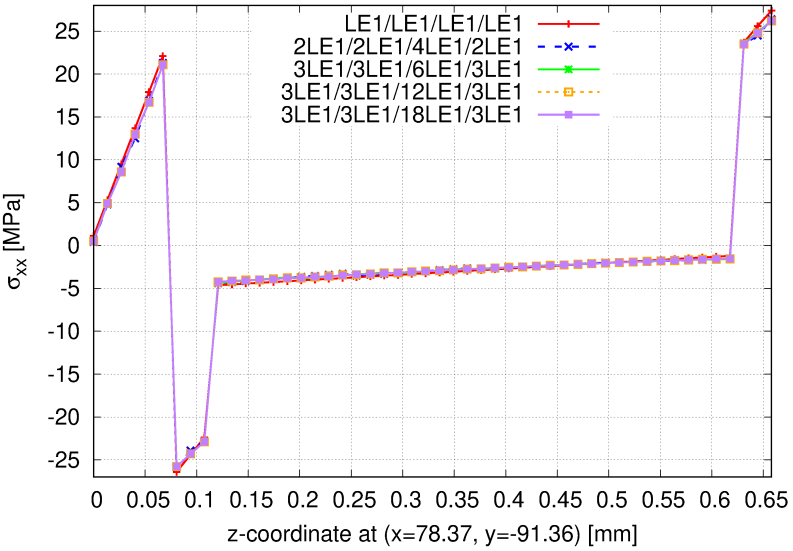

Figure 7.29: Effect of through-the-thickness mesh refinement on the σ_{xx} stress profile.

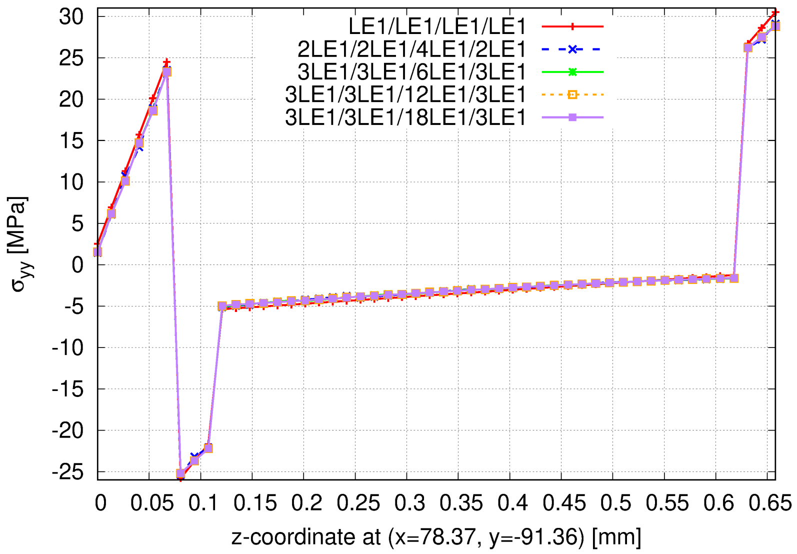

Figure 7.30: Effect of through-the-thickness mesh refinement on the σ_{yy} stress profile.

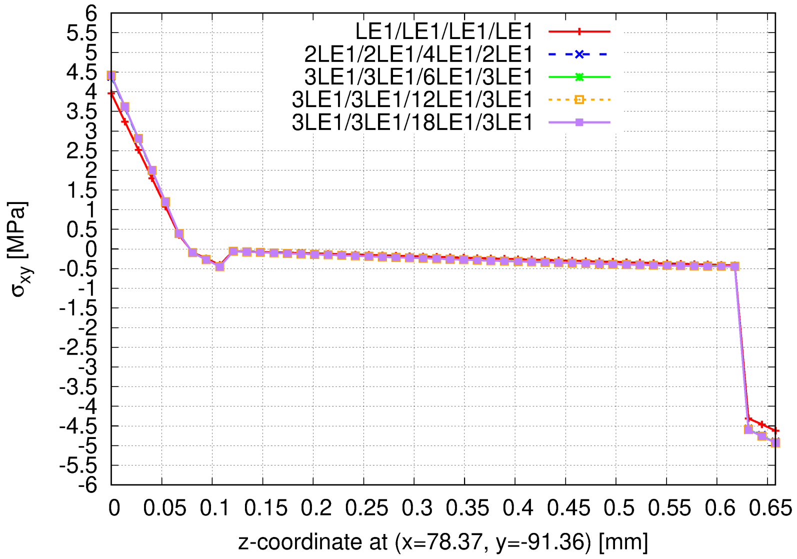

Figure 7.31: Effect of through-the-thickness mesh refinement on the σ_{xy} stress profile.

Chapter 8

Conclusions

This thesis research focused on the study of ultra-thin structures with embedded electronic components. The main objective was to develop structural models based on the Carrera Unified Formulation (CUF). The study was carried out with particular emphasis on Layer-Wise approaches capable of providing accurate numerical results from uncoupled thermo-elastic analyses, while ensuring compatibility with commercial software, specifically ABAQUS CAE, and achieving clear computational advantages. In this context, the work also addressed the increasing structural complexity of sub-array configurations, including variations in geometry, multilayered compositions, and the presence of microstrip lines, highlighting their influence on both displacement and stress fields. Through the preliminary models presented in chapter 6, it was possible to verify step by step the effectiveness of FEM modeling using CUF. Particular attention was devoted to the most advanced preliminary model, namely the sub-array composed of four layers and three different in-plane geometries. In this case, the CUF model demonstrated a high level of accuracy in capturing the displacement field with a significantly reduced number of degree of freedom. In particular, the Layer-Wise model based on second-order Lagrange expansions required 96813 DOF, compared to 315846 DOF for the ABAQUS model. Similarly, for the final model, the Layer-Wise formulation based on third-order Lagrange expansions involved 267843 DOF, compared to 412710 DOF for the ABAQUS model. After validating the displacement field, the analysis focused on the evaluation of stresses along the thickness in correspondence with the most highly loaded patches. In particular, the stress components σ_{xx},σ_{yy} and σ_{xy} were investigated at the interfaces between the different layers. Given the anisotropic nature of the plate and the presence of varying cross-sections, this analysis is essential to understand the structural response under thermal loading and to assess the limits of the material under such conditions. It can therefore be stated that the validity of Layer-Wise CUF models for the development of macroscopic representations of ultra-thin structures with embedded electronics has been verified. The possibility of obtaining detailed, pointwise stress information is particularly relevant for the exchange of data with models developed at the micromechanical level. The results obtained are thus well-suited for integration within a multiscale analysis framework.

8.1 Future works

Future work will focus on several key developments aimed at extending and improving the present modeling framework. First, the extension of the proposed approach to the nonlinear regime will be addressed. In particular, both geometric nonlinearities, associated with large displacements and rotations, and material nonlinearities, such as temperature-dependent behavior and possible inelastic effects, will be considered in order to provide a more realistic representation of ultra-thin structures under operational conditions. A second objective will be the investigation of thermal fatigue phenomena in ultra-thin anisotropic multilayered structures. Special attention will be devoted to the effects of repeated thermal loading and to the progressive evolution of stress states, with particular emphasis on interlaminar stresses, which play a crucial role in damage initiation and propagation. Another important development will concern the analysis of the influence of in-plane tensile loads applied to the structure to meet flatness requirements. These loads may significantly alter the stress distribution, including interlaminar stress components, and their interaction with thermal loading will be systematically investigated to capture possible coupled effects. Finally, further efforts will be dedicated to improving the coupling between macro-scale CUF models and micro-scale descriptions. The objective will be to enhance the accuracy of stress predictions, particularly at the interfaces and to enable more robust and efficient multiscale modeling strategies for ultra-thin structures with embedded electronics.

Appendix A

Through-the-thickness stress distributions for Patch 2 of the preliminary triangular sub-array model without microstrip lines

Table A.1: Interlayer stress convergence results along the plate thickness at $(x, y) = (78.62, -91.67)$ mm: Second-Order Lagrange expansion

z-coordinate [mm]	σ_{zz}	σ_{xx}	σ_{yy}	σ_{xy}
0.000	-0.25	0	0	4.5
0.080	0	-25.0	-25.0	-0.2
0.115	-0.35	-4.0	-5.0	-0.4
0.623	0.1	-22.0	26.0	-4.5
0.658	-0.4	24.0	29.0	-4.8

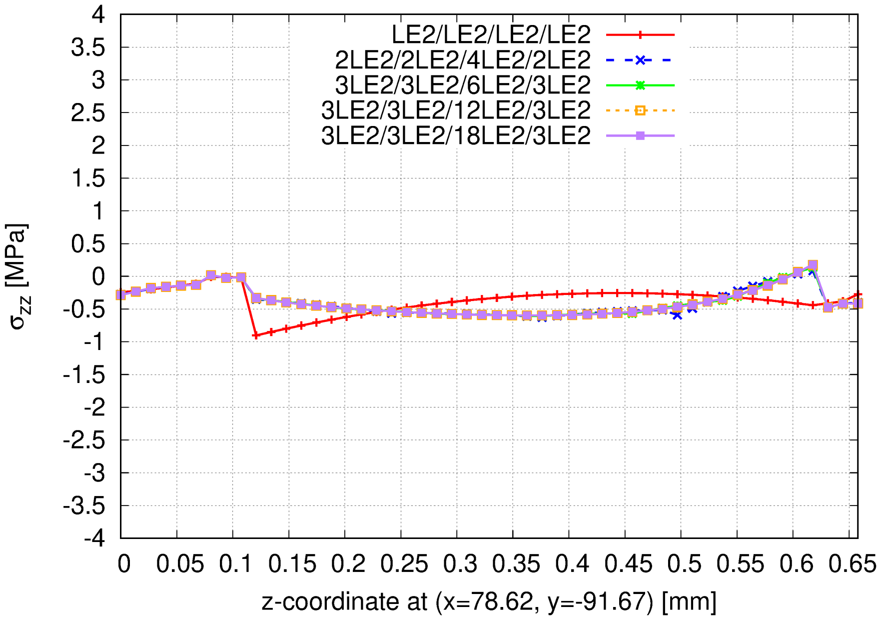

Figure A.1: Effect of through-the-thickness mesh refinement on the σ_{zz} stress profile. It is shown the comparison between the solution obtained with baseline mesh ($LE2/LE2/LE2/LE2$) and the refined configurations (up to $3LE2/3LE2/18LE2/3LE2$).

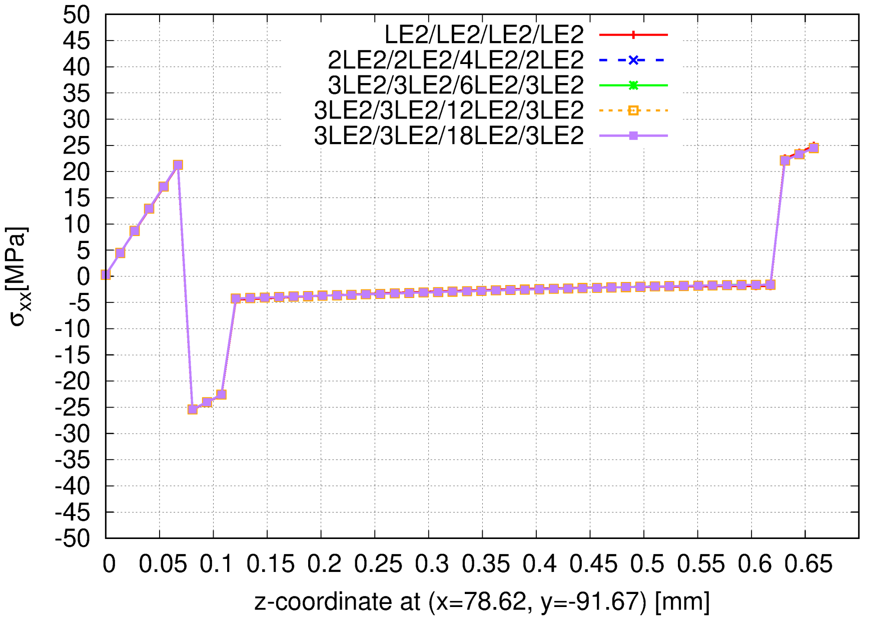

Figure A.2: Effect of through-the-thickness mesh refinement on the σ_{xx} stress profile.

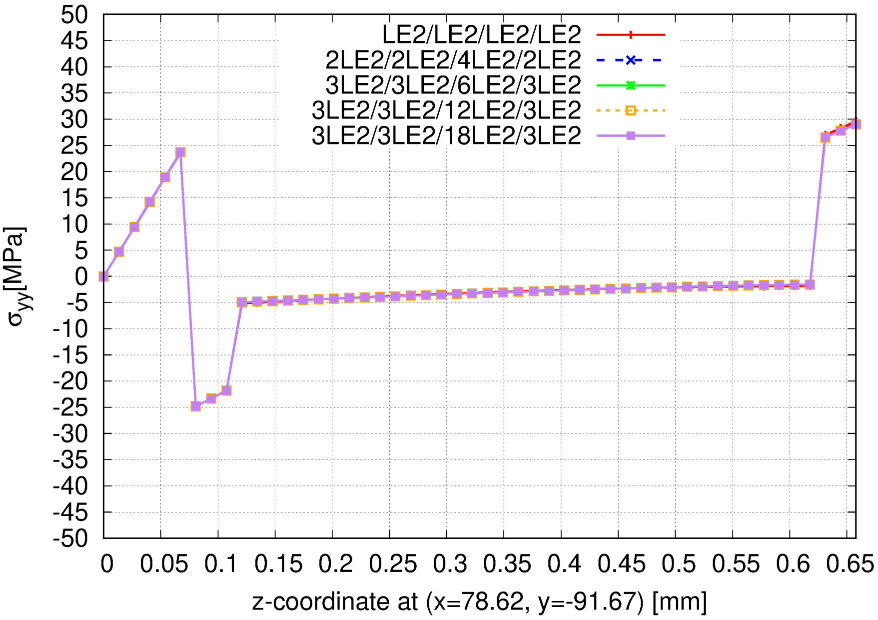

Figure A.3: Effect of through-the-thickness mesh refinement on the σ_{yy} stress profile.

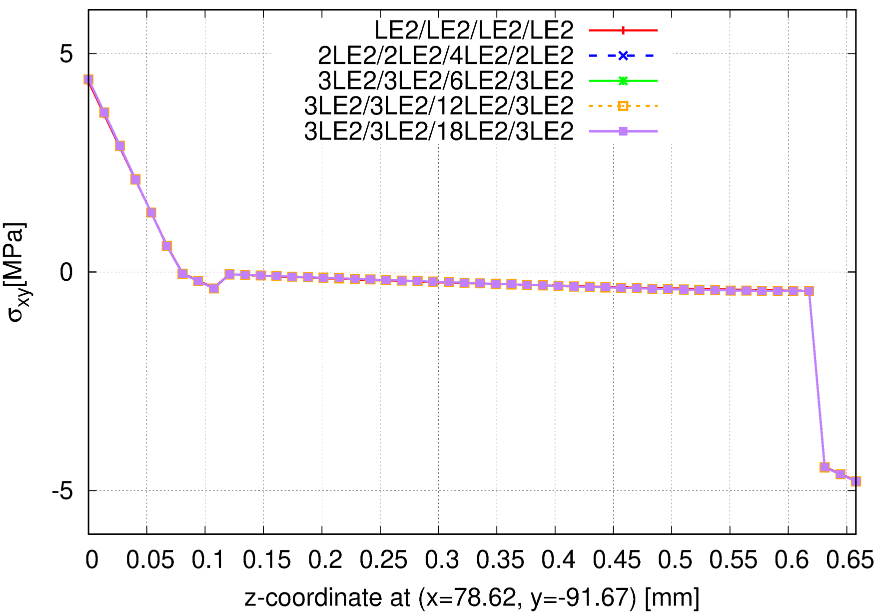

Figure A.4: Effect of through-the-thickness mesh refinement on the σ_{xy} stress profile.

Table A.2: Interlayer stress convergence results along the plate thickness at $(x, y) = (78.62, -91.67)$ mm: Third-Order Lagrange expansion

z-coordinate [mm]	σ_{zz}	σ_{xx}	σ_{yy}	σ_{xy}
0.000	-0.3	0	0	4.5
0.080	0	-25.0	-25.0	-0.2
0.115	-0.35	-4.0	-5.0	-0.4
0.623	0.15	-22.0	26.0	-4.5
0.658	-0.4	24.0	29.0	-4.8

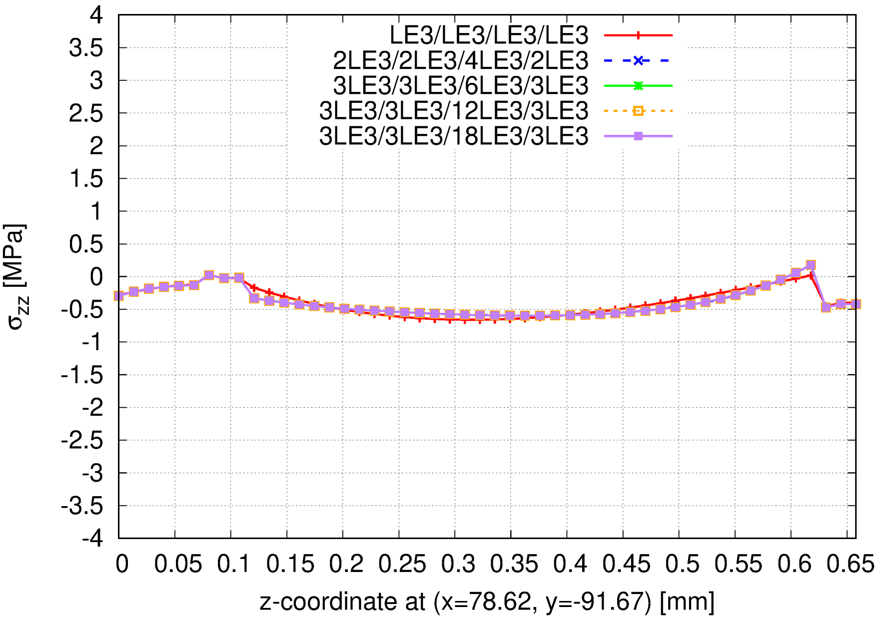

Figure A.5: Effect of through-the-thickness mesh refinement on the σ_{zz} stress profile.It is shown the comparison between the solution obtained with baseline mesh ($LE3/LE3/LE3/LE3$) and the refined configurations (up to $3LE3/3LE3/18LE3/3LE3$).

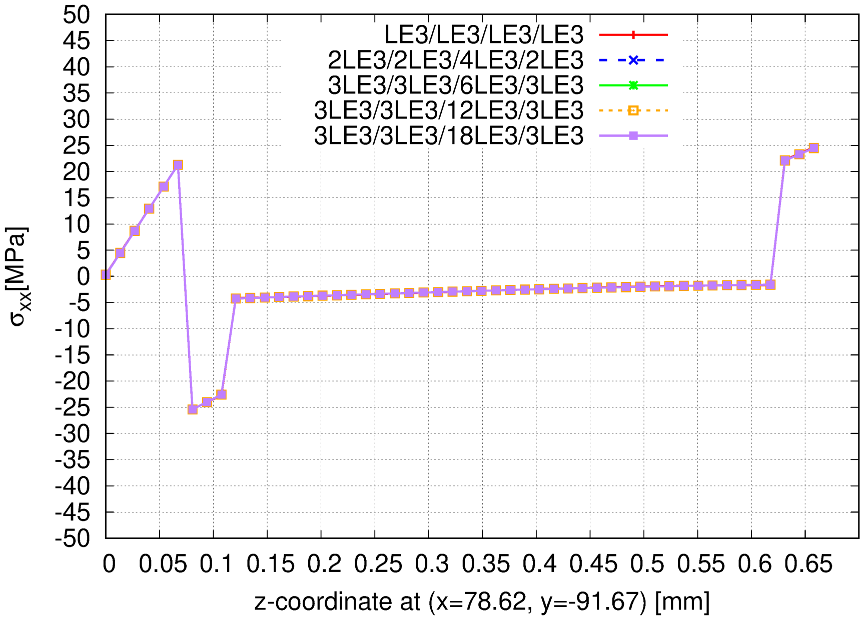

Figure A.6: Effect of through-the-thickness mesh refinement on the σ_{xx} stress profile.

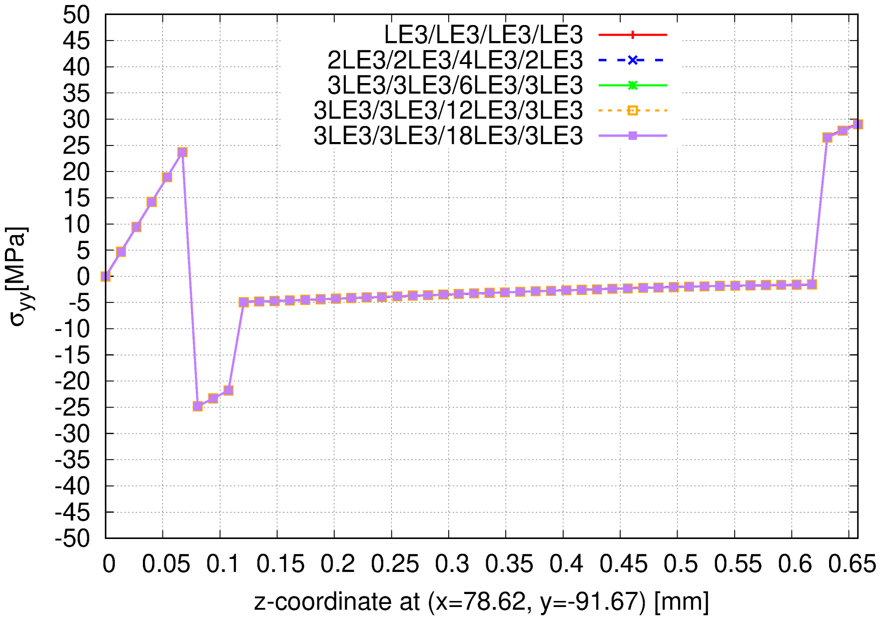

Figure A.7: Effect of through-the-thickness mesh refinement on the σ_{yy} stress profile.

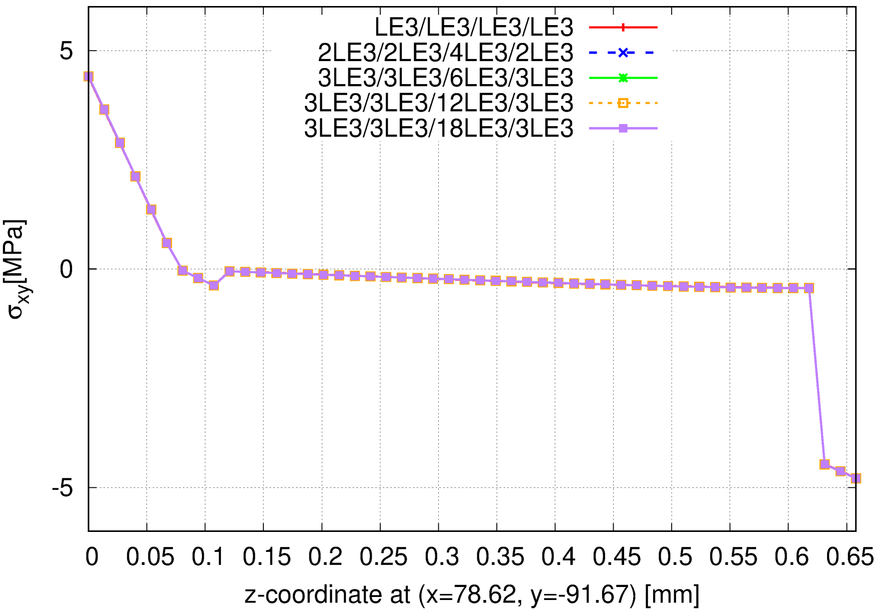

Figure A.8: Effect of through-the-thickness mesh refinement on the σ_{xy} stress profile.

Appendix B

Through-the-thickness stress distributions for Patch 2 of final triangular sub-array model

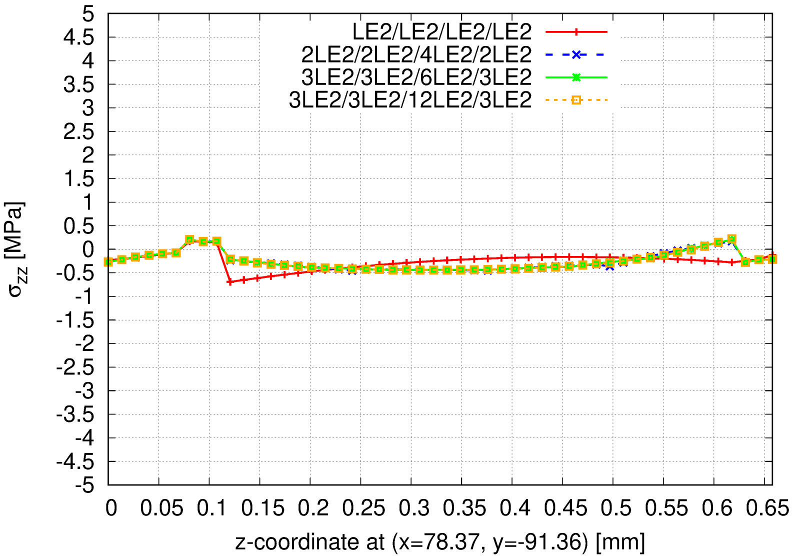

Figure B.1: Effect of through-the-thickness mesh refinement on the σ_{zz} stress profile. The comparison between the baseline mesh ($LE2/LE2/LE2/LE2$) and the refined configurations (up to $3LE2/3LE2/12LE2/3LE2$) shows that the stress gradients are consistently captured, indicating a converged numerical solution

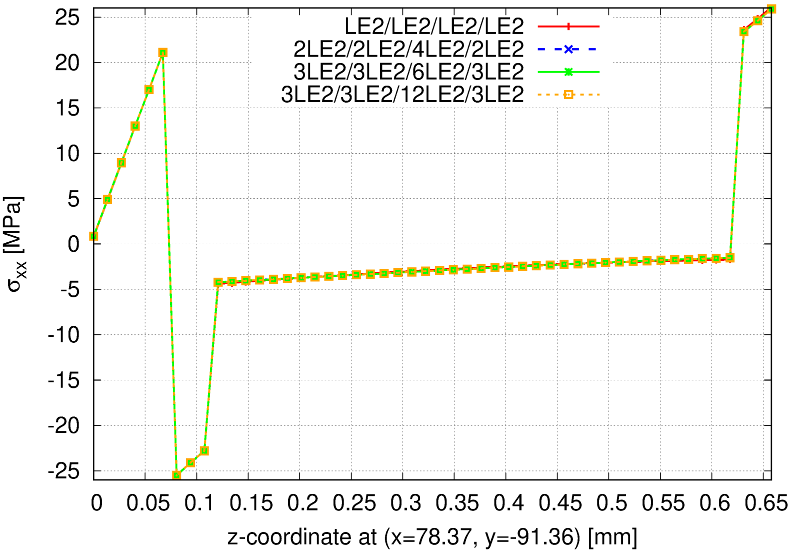

Figure B.2: Effect of through-the-thickness mesh refinement on the σ_{xx} stress profile.

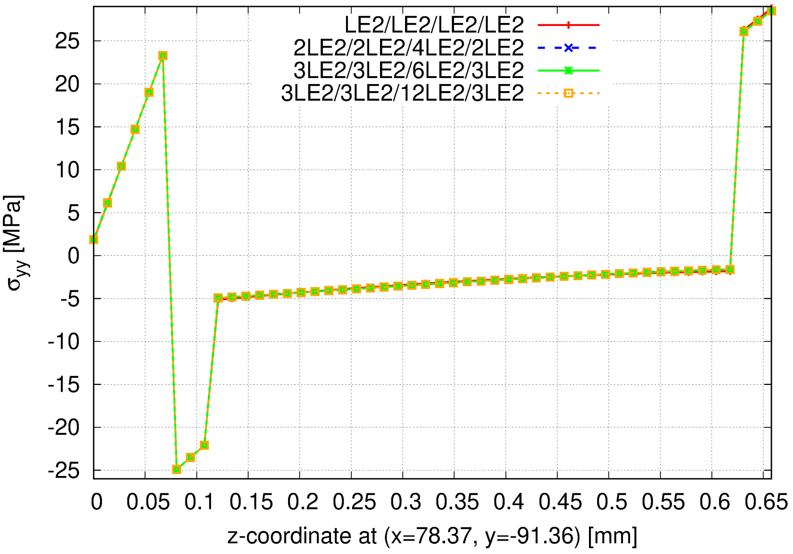

Figure B.3: Effect of through-the-thickness mesh refinement on the σ_{yy} stress profile.

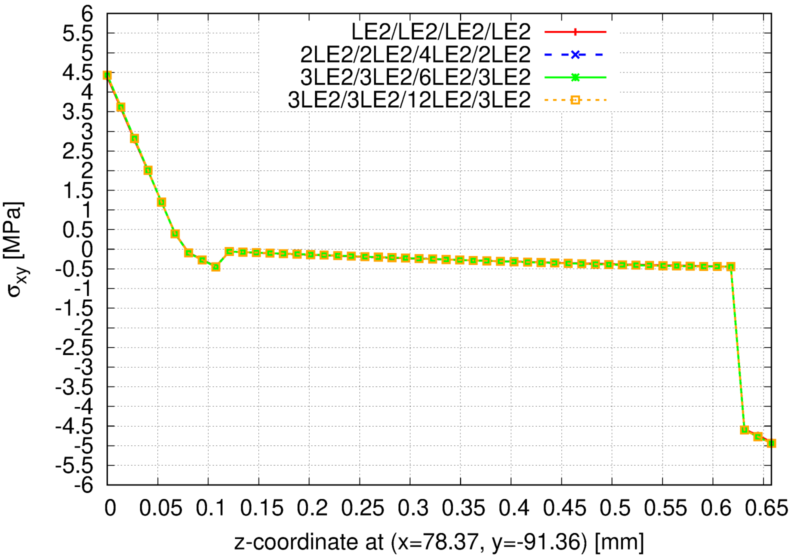

Figure B.4: Effect of through-the-thickness mesh refinement on the σ_{xy} stress profile.

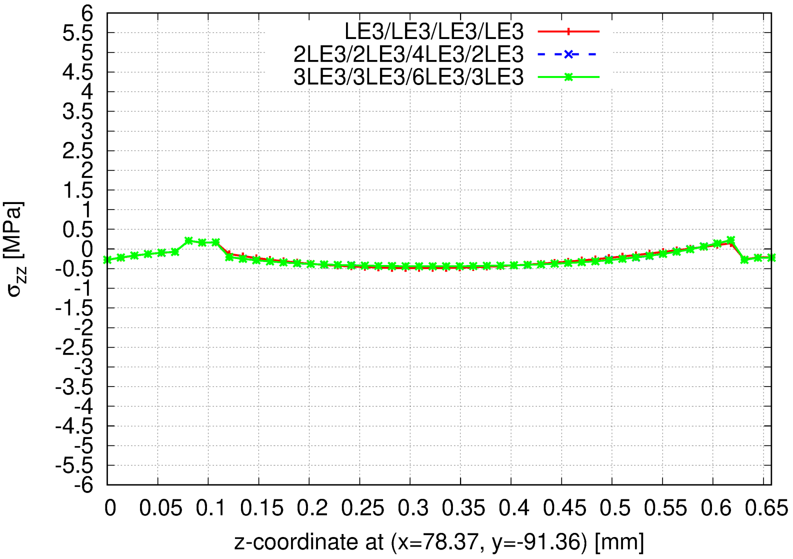

Figure B.5: Effect of through-the-thickness mesh refinement on the σ_{zz} stress profile. the baseline mesh ($LE3/LE3/LE3/LE3$) and the refined configurations (up to $3LE3/3LE3/6LE3/3LE3$) shows that the stress gradients are consistently captured, indicating a converged numerical solution

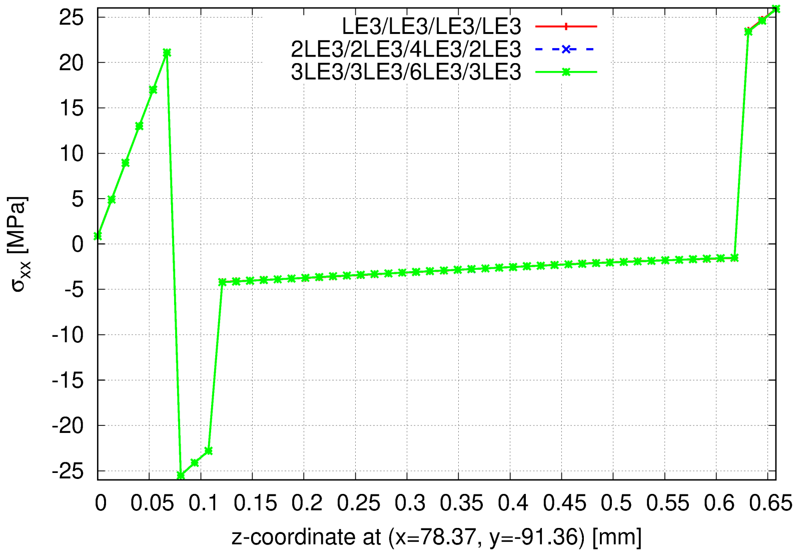

Figure B.6: Effect of through-the-thickness mesh refinement on the σ_{xx} stress profile.

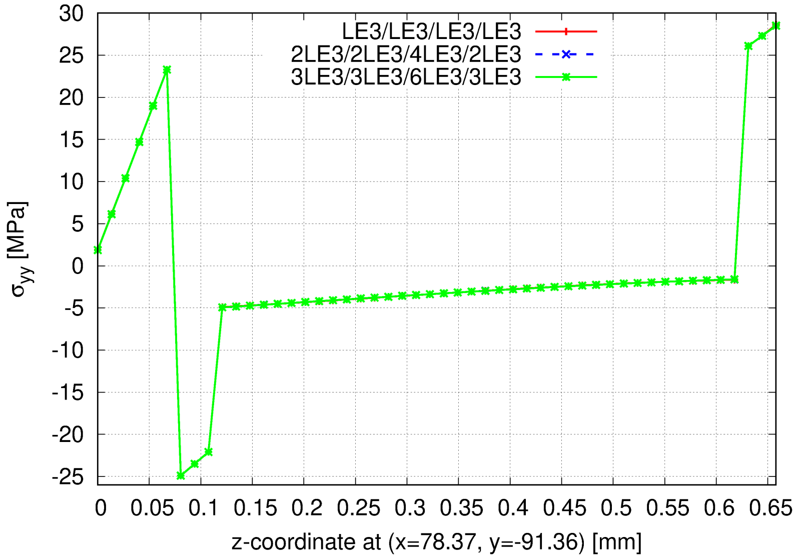

Figure B.7: Effect of through-the-thickness mesh refinement on the σ_{yy} stress profile.

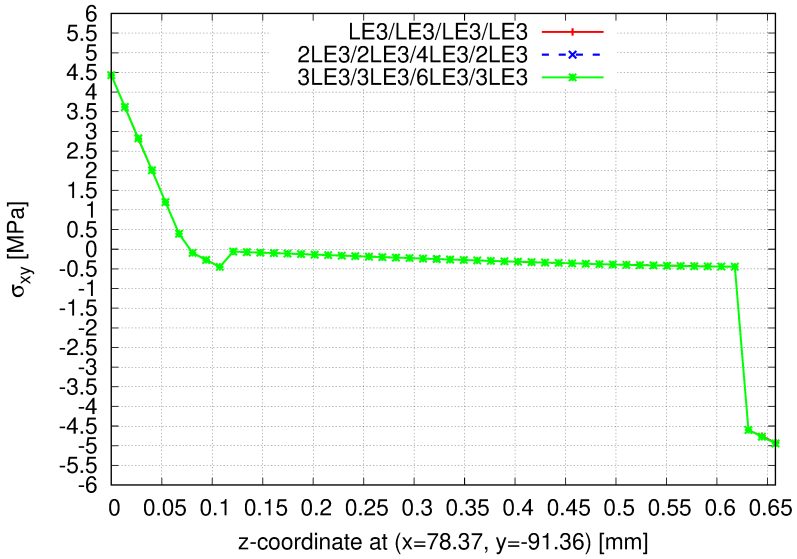

Figure B.8: Effect of through-the-thickness mesh refinement on the σ_{xy} stress profile.

Bibliography

[1] Ibuki Hayashi, Ryo Higuchi, Tomohiro Yokozeki, and Takahira Aoki. “Analytical study on the thermal deformation of ultralight phased array antenna”. In: *Acta Astronautica* 188 (Aug. 2021), pp. 531–544 (cit. on p. 1).

[2] European Space Agency. *Types of orbits*. Accesso: 24 Maggio 2024. ESA. 2020. URL: `https://www.esa.int/Enabling_Support/Space_Transportation/Types_of_orbits#GEO` (cit. on p. 2).

[3] Thermal Engineer. *Standard Environments - Atmospheric Properties*. Accesso: 24 Maggio 2024. Thermal Engineer. 2024. URL: `https://www.thermalengineer.com/library/environments.htm` (cit. on p. 3).

[4] Chen Yang, Xuepan Zhang, Xiaoqi Huang, ZhengAi Cheng, Xinghua Zhang, and Xinbin Hou. “Optimal sensor placement for deployable antenna module health monitoring in SSPS using genetic algorithm”. In: *Acta Astronautica* 140 (Nov. 2017), pp. 213–224 (cit. on p. 6).

[5] L. Datashvili, S. Endler, B. Wei, H. Baier, H. Langer, M. Friemel, N. Tsignadze, and J. Santiago-Prowald. “Study of mechanical architectures of large deployable space antenna apertures: from design to tests”. In: *CEAS Space Journal* 5.3–4 (Dec. 2013), pp. 169–184 (cit. on p. 6).

[6] Fei Zheng, Mei Chen, and Jie He. “Analyses of a New Simplified Large Deployable Reflector Structure”. In: *2008 IEEE Aerospace Conference*. Mar. 2008, pp. 1–7 (cit. on p. 7).

[7] W. Seboldt, M. Klimke, M. Leipold, and N. Hanowski. “European Sail Tower SPS Concept”. In: *Acta Astronautica* 48.5–12 (May 2001), pp. 785–792 (cit. on p. 8).

[8] Susumu Sasaki, Koji Tanaka, Ken Higuchi, Nobukatsu Okuizumi, Shigeo Kawasaki, Naoki Shinohara, Kei Senda, and Kousei Ishimura. “A new concept of solar power satellite: Tethered-SPS”. In: *Acta Astronautica* 60.2 (Jan. 2007), pp. 153–165 (cit. on p. 9).

[9] Yang Yang, Yiqun Zhang, Baoyan Duan, Dongxu Wang, and Xun Li. "A novel design project for space solar power station (SSPS-OMEGA)". In: *Acta Astronautica* 121 (Apr. 2016), pp. 51–58 (cit. on p. 10).

[10] Hiroaki Tanaka et al. "Experimental demonstration of deformable reflector antenna system with high accuracy deformation measurement". In: *Acta Astronautica* 194 (May 2022), pp. 93–105 (cit. on p. 11).

[11] John R. Glaese and Emmett J. McDonald. *Space Solar Power Multi-Body Dynamics and Controls, Concepts for the Integrated Symmetrical Concentrator Configuration.* Final Report Contract NAS8-00151. NASA Marshall Space Flight Center, Dec. 2000 (cit. on p. 11).

[12] R. S. Vaidya and C. T. Sun. "Prediction of composite properties from a representative volume element". In: *Journal of Applied Mechanics* 56 (1996), pp. 171–179 (cit. on p. 14).

[13] Z. Huang and Y. Wang. "Analytical micromechanics models for elastoplastic behavior of long fibrous composites: A critical review and comparative study". In: *Materials (Basel)* 11.10 (2018), pp. 143–256 (cit. on p. 14).

[14] W. Voigt. "Theoretische Studien über die Elasticitätsverhältnisse der Krystalle". In: *Abhandlungen der Königlichen Gesellschaft der Wissenschaften in Göttingen* 34 (1887), pp. 3–51 (cit. on p. 15).

[15] András Reuss. "Berechnung der Fließgrenze von Mischkristallen auf Grund der Plastizitätsbedingung für Einkristalle". In: *ZAMM - Journal of Applied Mathematics and Mechanics / Zeitschrift für Angewandte Mathematik und Mechanik* 9.1 (1929), pp. 49–58 (cit. on p. 15).

[16] Z. Hashin and S. Shtrikman. "A variational approach to the theory of the elastic behaviour of polycrystals". In: *Journal of the Mechanics and Physics of Solids* 10.4 (1962), pp. 343–352 (cit. on p. 15).

[17] T. Mori and K. Tanaka. "Average stress in matrix and average elastic energy of materials with misfitting inclusions". In: *Acta Metallurgica* 21.5 (1973), pp. 571–574 (cit. on p. 15).

[18] J. Aboudi. "A continuum theory for fiber-reinforced elastic-viscoplastic composites". In: *International Journal of Engineering Science* 20.5 (1982), pp. 605–621 (cit. on p. 15).

[19] M. Paley and J. Aboudi. "Micromechanical analysis of composites by the generalized cells model". In: *Mechanics of Materials* 14.2 (1992), pp. 127–139 (cit. on p. 15).

[20] J. Aboudi, M. J. Pineda, and S. M. Arnold. "Linear thermoelastic higher-order theory for periodic multiphase materials". In: *Journal of Applied Mechanics* 68.5 (2001), pp. 697–707 (cit. on p. 16).

[21] W. Yu. “A unified theory for constitutive modeling of composites”. In: *Journal of Mechanics of Materials and Structures* 11.4 (2016), pp. 379–411 (cit. on p. 16).

[22] A. R. Sánchez-Majano, R. Masia, A. Pagani, and E. Carrera. “Microscale thermo-elastic analysis of composite materials by high-order geometrically accurate finite elements”. In: *Composite Structures* 300 (2022), p. 116105. DOI: `10.1016/j.compstruct.2022.116105` (cit. on p. 16).

[23] A. G. de Miguel, A. Pagani, W. Yu, and E. Carrera. “Micromechanics of periodically heterogeneous materials using higher-order beam theories and the mechanics of structure genome”. In: *Composite Structures* 180 (2017), pp. 484–496. DOI: `10.1016/j.compstruct.2017.08.025` (cit. on p. 19).

[24] E. Carrera, A. G. de Miguel, and A. Pagani. “Hierarchical theories of structures based on Legendre polynomial expansions with finite element applications”. In: *International Journal of Mechanical Sciences* 120 (2017), pp. 286–300. DOI: `10.1016/j.ijmecsci.2016.11.021` (cit. on p. 20).

[25] Alberto Racionero Sánchez-Majano. “Multiscale finite element models for the analysis, design and optimisation of variable stiffness composites”. Doctoral Dissertation. Politecnico di Torino, 2024 (cit. on p. 20).

[26] Rebecca Masia. “Modelli multiscala per analisi igro-termo-elastica di strutture e materiali compositi eterogenei”. Tesi di Laurea Magistrale. Politecnico di Torino, 2022 (cit. on pp. 20, 25).

[27] Erasmo Carrera, Maria Cinefra, Marco Petrolo, and Enrico Zappino. *Finite Element Analysis of Structures through Unified Formulation.* Chichester, UK: John Wiley & Sons, 2014. ISBN: 978-1-119-94121-7 (cit. on pp. 25, 36).

[28] Francesca Bracaglia. “Thermo-elastic analysis of variable stiffness composites”. Tesi di Laurea Magistrale. Politecnico di Torino, 2023 (cit. on pp. 25, 49).

[29] Erasmo Carrera, Fiorenzo A. Fazzolari, and Maria Cinefra. *Thermal Stress Analysis of Beams, Plates and Shells: Computational Modelling and Applications.* Amsterdam, Netherlands: Elsevier, 2017. ISBN: 978-0-12-420093-7 (cit. on p. 44).

[30] Alfonso Pagani, Piero Chiaia, and Alberto Racionero Sánchez-Majano. *Analisi termoelastiche di strutture aerospaziali.* Dispense del corso di Strutture per Veicoli Spaziali (Cod. 01SRMMT, 04LNUMT). A.A. 2023/2024. Politecnico di Torino, 2023 (cit. on p. 49).

[31] Alfonso Pagani, Enrico Zappino, Francesca Bracaglia, Rebecca Masia, and Erasmo Carrera. “Thermal stress analysis of variable angle tow composite plates through high-order structural models”. In: *Composite Structures* 327 (2024), p. 117668. DOI: `10.1016/j.compstruct.2023.117668` (cit. on p. 49).

[32] Fei Tao, Xiuqi Lyu, Xin Liu, and Wenbin Yu. “Multiscale analysis of multilayer printed circuit board using mechanics of structure genome”. In: *Mechanics of Advanced Materials and Structures* 28.8 (2021), pp. 774–783. DOI: `10.1080/15376494.2019.1596335`.

[33] Shoji Kitamura, Hiroshi Aoki, Yasushi Okawa, and Hirofumi Taniguchi. “Study of space transportation for space solar power systems”. In: *Acta Astronautica* 60.1 (Jan. 2007), pp. 1–6.

[34] Domenico Andrea Iannotta. “Analisi "global/local" di strutture spaziali dispiegabili in materiale composito”. Tesi di Laurea Magistrale. Politecnico di Torino, 2021.

[35] Elisa Tortorelli. “Modelli 2D avanzati per lo studio di strutture in materiale iperelastico”. Tesi di Laurea Magistrale. Politecnico di Torino, 2022.

[36] A. Canabal, R. P. Jedlicka, and A. G. Pino. “Multifunctional phased array antenna design for satellite tracking”. In: *Acta Astronautica* 57.11 (Dec. 2005), pp. 887–900.

[37] James Taylor, Atsushi Okazaki, Takumi Honda, Shunji Kotsuki, Moeka Yamaji, Takuji Kubota, Riko Oki, Toshio Iguchi, and Takemasa Miyoshi. “Oversampling reflectivity observations from a geostationary precipitation radar satellite: Impact on typhoon forecasts within a perfect model OSSE framework”. In: *Journal of Advances in Modeling Earth Systems (JAMES)* 13.6 (2021), e2020MS002332. DOI: `10.1029/2020MS002332`.

[38] Atsushi Okazaki, Takumi Honda, Shunji Kotsuki, Moeka Yamaji, Takuji Kubota, Riko Oki, Toshio Iguchi, and Takemasa Miyoshi. “Simulating precipitation radar observations from a geostationary satellite”. In: *Atmospheric Measurement Techniques* 12.7 (2019), pp. 3985–3996. DOI: `10.5194/amt-12-3985-2019`.